INFORMATION TO USERS

This manuscript has been reproduced from the microfilm master. UMI films the text directly from the original or copy submitted. Thus, some thesis and dissertation copies are in typewriter face, while others may be from any type of computer printer.

The quality of this reproduction is dependent upon the quality of the copy submitted. Broken or indistinct print, colored or poor quality illustrations and photographs, print bleedthrough, substandard margins, and improper alignment can adversely affect reproduction.

In the unlikely event that the author did not send UMI a complete manuscript and there are missing pages, these will be noted. Also, if unauthorized copyright material had to be removed, a note will indicate the deletion.

Oversize materials (e.g., maps, drawings, charts) are reproduced by sectioning the original, beginning at the upper left-hand corner and continuing from left to right in equal sections with small overlaps.

ProQuest Information and Learning
300 North Zeeb Road, Ann Arbor, MI 48106-1346 USA
800-521-0600

ELECTRON SPIN RESONANCE STUDIES OF $^{53}Cr^{3+}$ AND VO^{2+} IONS IN $AlCl_3.6H_2O$

by

Kenneth Pack

Submitted in partial fulfillment of the
requirements for the degree of
Master of Science.

Department of Physics
School of Graduate Studies
University of Ottawa
Ottawa, Canada

1975

ABSTRACT

Electron spin resonance (ESR) studies are reported for Cr^{3+} and VO^{2+} in $AlCl_3.6H_2O$. Electron-nuclear double resonance (ENDOR) studies are reported for the isotope $^{53}Cr^{3+}$ in $AlCl_3.6H_2O$. All the microwave measurements were done at X-band microwave frequencies ($\sim$ 9.4 GHz). The VO^{2+} study was done at room temperature and it shows that these are two different orientations of the $Al^{3+}.6H_2O$ complexes per unit cell. The $VO^{2+}.5H_2O$ complexes associated with the two types of $Al^{3+}.6H_2O$ complexes are rotated with respect to each other by an angle $33^{o} \pm 3^{o}$ in the plane perpendicular to the crystal c axis. The Cr^{3+} ESR measurements were done at four temperatures between room and liquid helium temperature, while the ENDOR of $^{53}Cr^{3+}$ was done at liquid helium temperature. The Cr^{3+} studies show that the sign of the spin Hamiltonian zero-field splitting parameter D is negative, indicating that the $Cr^{3+}.6H_2O$ magnetic complexes are trigonally compressed in $AlCl_3.6H_2O$. A comparison is made between the spin Hamiltonian parameter for $^{53}Cr^{3+}$ impurities in several hydrated crystals and it is found that a purely static crystal field model does not satisfactorily explain the experimental results. When the VO^{2+} spin Hamiltonian parameters are also included in the comparison it is possible to make conclusions regarding the relative susceptibility of the various $Al^{3+}.6H_2O$ complexes to distortion upon impurity doping. In particular it is concluded that the complexes in CsAl alum are more susceptible to distortion than are those in $AlCl_3.6H_2O$.

ACKNOWLEDGMENTS

I am very much indebted to the assistance and encouragement provided throughout the course of research by my supervisor, Dr. Manoogian, thank you. The special insight of Mr. Bei Wah Chan concerning the operation of the spectrometers is gladly acknowledged. I have also benefited from discussions with Mr. Andre Leclerc. Financial assistance from Dr. Manoogian's National Research Council grant is gratefully acknwoledged. Thanks are also due to Mrs. Loretta Leroux for her speedy and accurate typing of the thesis.

TABLE OF CONTENTS

LIST OF FIGURES

LIST OF TABLES

CHAPTER I INTRODUCTION

Electron spin resonance (ESR) measurements were made on $AlCl_3.6H_2O$ doped with Cr^{3+} at room temperature (297^oK), carbon dioxide sublimation temperature (195^oK), liquid nitrogen temperature (77^oK), and liquid helium temperature (4.2^oK). This aspect of the work was done because the results obtained by others[1,2,3] in this crystal are not consistent with each other at all temperatures in respect to the magnitude of the spin Hamiltonian zero-field splitting parameter D. While the nature of the D vs. T curve was not analysed in this work, a true description of its behaviour is of importance when considering the crystal vibrational and static crystal distortion contributions to D. This problem is considered by others in this laboratory. The sign of D, which has not been previously reported, is found to be negative by comparing relative intensities of the ESR lines at 297^oK and 4.2^oK. The negative sign indicates that the octahedron of waters surrounding the chromium impurity is trigonally compressed.

The principal chromium study with which this thesis is involved is the electron-nuclear double resonance (ENDOR) of $^{53}Cr^{3+}$ impurities in $AlCl_3.6H_2O$ at 4.2^oK. The $^{53}Cr^{3+}$ isotope is enriched to $\sim$ 96% in the crystal. ESR measurements were also made on the vanadyl ion, VO^{2+}, doped in the crystal. This study was done at room temperature. No previous study has been reported for the ENDOR of $^{53}Cr^{3+}$ or

the ESR of VO^{2+} in $AlCl_3.6H_2O$. The purpose of the ENDOR study is to obtain accurate values of the spin Hamiltonian hyperfine parameters A, B, and Q'. The ENDOR study also confirms the negative sign of D. The relations between A-B and D, and between Q' and D for $^{53}Cr^{3+}$ in hydrated crystals are examined. It is found that a pure static model for the trigonal distortion at the chromium site does not satisfactorily explain the experimental results. In particular, the quadrupole interaction parameter Q' is nearly the same magnitude in $AlCl_3.6H_2O$ as in the cesium alums, even though the D value at $4.2^{o}K$ is considerably smaller in $AlCl_3.6H_2O$. The purely static model predicts that Q' is proportional to $D_{4.2^{o}K}$.

Neutron diffraction and X-ray measurements in $AlCl_3.6H_2O$ show that there are two different orientations of the $Al^{3+}.6H_2O$ complex per unit cell[4,6]. The vanadyl pentrahydrate complexes, $VO^{2+}.5H_2O$, associated with the two types of aluminium complexes are rotated to each other by an angle of $33^{o} \pm 3^{o}$ in a plane perpendicular to the crystal c axis. Except for this difference in orientation, the two types of $VO^{2+}.5H_2O$ complexes are equivalent. The $Al^{3+}.6H_2O$ complexes in $AlCl_3.6H_2O$ and CsAl alum are identical in size and shape[4,5]. A comparison of the spin Hamiltonian parameters for $^{53}Cr^{3+}$ and VO^{2+} in these crystals allows deductions to be made regarding the effect of impurity doping in similar $Al^{3+}.6H_2O$ complexes for different crystals.

CHAPTER II CRYSTALLOGRAPHY

(1) Crystal Structure

The structure of aluminium chloride hexahydrate, $AlCl_3.6H_2O$, and chromium chloride hexahydrate, $CrCl_3.6H_2O$, were originally investigated by Andress and Carpenter[6]. They found, via X-ray diffraction, the crystal symmetry of these two salts to be $R\bar{3}c$. Later experiments on $AlCl_3.6H_2O$ by Buchanan and Harris[4] confirmed the space group designation of $AlCl_3.6H_2O$. In terms of a hexagonal unit cell they found $a = 11.827 \pm 0.006$ Å and $c = 11.895 \pm 0.003$Å

Both crystals are composed of chains of the form $-M(H_2O)_6^{3+} - 3Cl^- - M(H_2O)_6^{3+} - 3Cl^- -$ running parallel to the c axis of the hexagonal unit cell, where M is the metal ion in the centre of the octahedron of waters. Along each chain alternate octahedra are rotated with respect to each other about their [111] direction. The angle which the octahedra make with respect to each other is, according to Andress and Carpenter, about 24^{o} [6]. Buchanan and Harris found it to be about 28^{o} [4]. Within the experimental error of X-ray and neutron diffraction measurements the hydrated complex $Al(H_2O)_6^{3+}$ in $AlCl_3.6H_2O$ was found to be a regular octahedron[4]. Each octahedron has a trigonal axis parallel to the crystal c axis. If the octahedra are perfect then their tetragonal axes make an angle of $54^{o}44'$ with the c axis.

Table 2-1 lists some of the crystal parameters of $AlCl_3.6H_2O$ and $CrCl_3.6H_2O$. Figures 2-1 and 2-2 show two alternate unit cells for $AlCl_3.6H_2O$.

Figure 2-1: The hexagonal unit cell for $AlCl_3.6H_2O$ (and $CrCl_3.6H_2O$)*

* The Al^{3+} (Cr^{3+}) centers of the oxygen octahedra are not shown. Not all of the hydrogen atoms are shown.

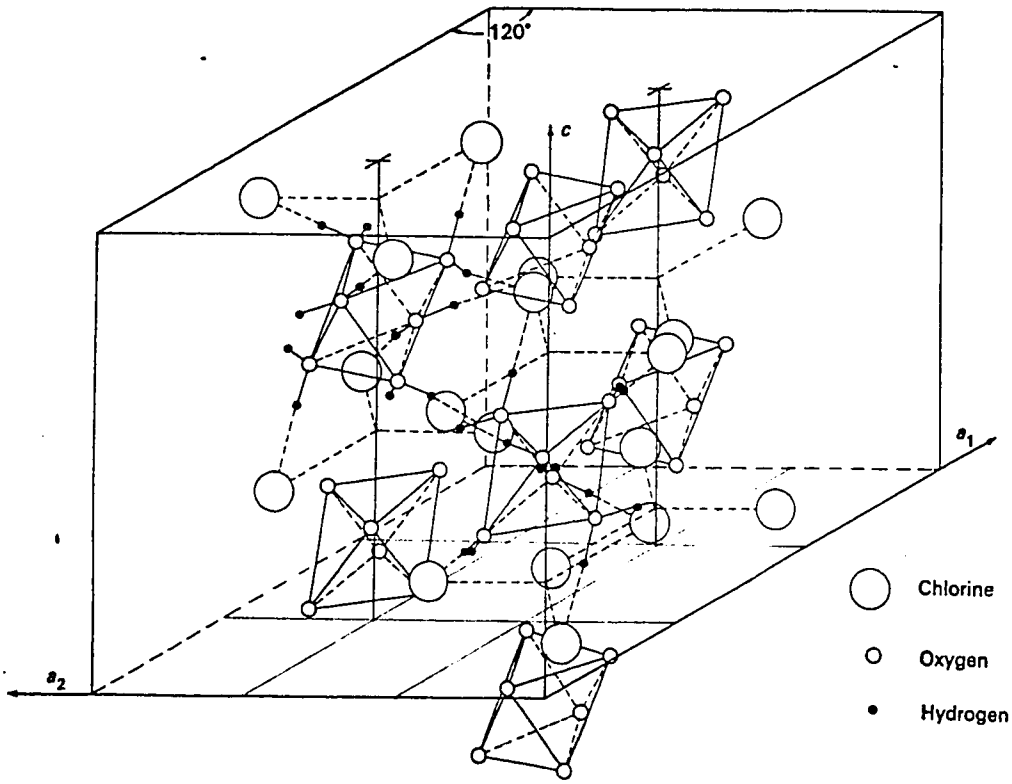
120°
c
a_1
a_2
Chlorine
Oxygen
Hydrogen

Figure 2-2: The rhombohedral unit cell for $AlCl_3.6H_2O$ (and $CrCl_3.6H_2O$).

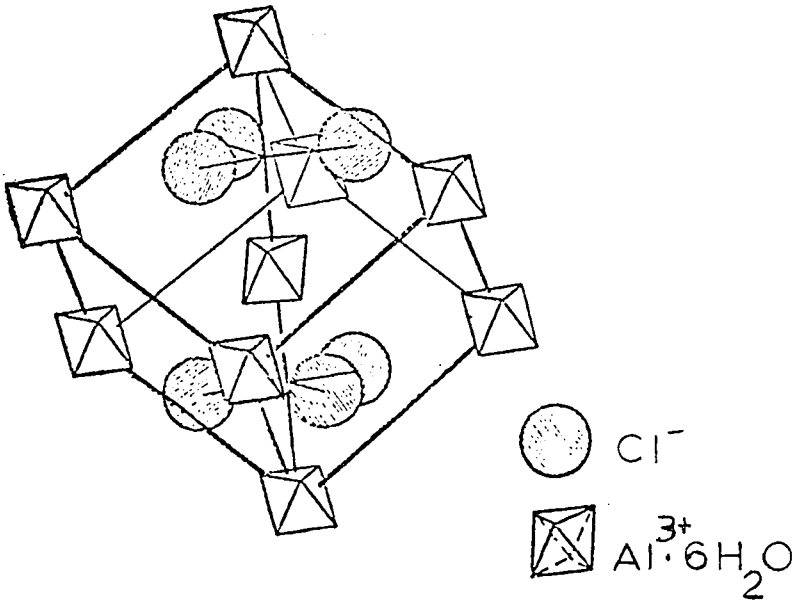
Cl^-
$Al^{3+} \cdot 6H_2O$

TABLE 2-1: Crystal parameters of $AlCl_3.6H_2O$ and $CrCl_3.6H_2O$

Rhombohedral Unit Cell Dimensions	$AlCl_3.6H_2O$	$CrCl_3.6H_2O$
a	7.85 ± 0.03	7.95 ± 0.03
α	97^o ± 20'	97^o ± 20'
Metal-Water Bond Distance (Å) [6]	1.87	1.90
Metal-Oxygen Bond Distance (Å) [4]	1.88 ± 0.02	not measured

(2) Material Preparation

Single aluminium chloride hexahydrate crystals were grown from a water solution of the dissolved salt. The crystals were found to be hygroscopic. By spraying the crystals with several coats of krylon varnish, and working during the winter when the atmosphere was dry, it was possible to keep the crystals intact for several months.

The crystals were doped with either Cr^{3+} in its natural abundance (83.76% ^{52}Cr, 9.55% ^{53}Cr), Cr^{3+} which was enriched to 96.4% ^{53}Cr, or VO^{2+} (99.76% ^{51}V). The different paramagnetic ions were obtained from aqueous solutions of chromium chloride, chromium

sulfate, and vanadyl sulfate, respectively. The ^{53}Cr dopant was obtained from Oak Ridge National Laboratory. The paramagnetic ion concentration in the $AlCl_3.6H_2O$ crystals were estimated to be less than 0.01% by weight in each case.

(3) Crystal Habit

The crystals grew as either thin elongated hexagonal prisms as shown in Figure 2-3a, or as rounded hexagonal prisms as shown in Figure 2-3b. In the case of the thin crystal the c axis is parallel to the elongated direction, and in the rounded crystal it is perpendicular to the hexagonal shaped plane.

Figure 2-3: Growth habits of $AlCl_3.6H_2O$

(a) elongated growth habit,

(b) rounded growth habit.

(a)

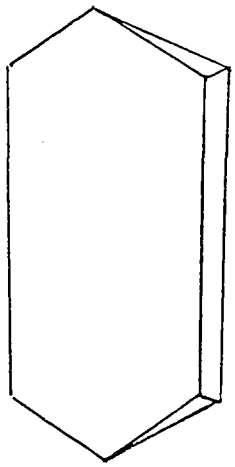

(b)

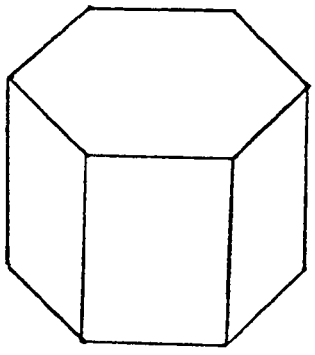

CHAPTER III THEORY

(1) General 'Theoretical' Hamiltonian

The general theoretical Hamiltonian describing an ion in a crystal is

$$\mathcal{H} = \mathcal{H}_o + \mathcal{H}_{LF} + \mathcal{H}_{LS} + \mathcal{H}_{SS} + \mathcal{H}_{Ze} + \mathcal{H}_{SI} + \mathcal{H}_{Q} + \mathcal{H}_{Zn} \qquad 3\text{-}1$$

The Hamiltonian can be considered as representing a perturbed system where the last six terms are the perturbing interactions.

$\mathcal{H}_o$ is the Hamiltonian for the free ion. Its non-relativistic form is

$$\mathcal{H}_o = \sum_k (P_k^2/2m - Ze^2/r_k) + \sum_{j<k} e^2/r_{xj}$$

$\mathcal{H}_{LF}$ is the Hamiltonian for the crystal or ligand field. Its exact form depends on the symmetry of the field.

$\mathcal{H}_{LS}$ represents the spin-orbit coupling. The origin of this interaction can be briefly outlined as follows. Classically the magnetic field at an electron due to its orbital motion is given by the Biot-Savart Law $\vec{H} = -\frac{\vec{v} \times \vec{E}}{c}$ [7].

Hence

$$\vec{H} = \frac{Ze}{cr^3}(\vec{r} \times \vec{v}) = \frac{Ze\hbar\vec{\ell}}{mcr^3} .$$

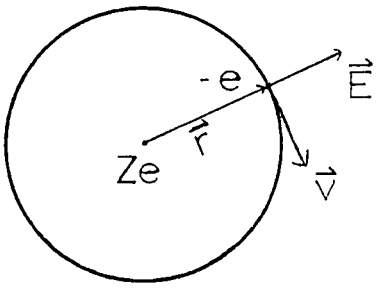

The interaction between this magnetic field and the spin magnetic moment is

$$\mathcal{H} = -\vec{\mu}_s \cdot \vec{H} = (2\beta) \frac{(Ze\hbar)}{mc\langle r^3 \rangle} \vec{s} \cdot \vec{\ell} = 4\beta^2 \frac{Ze}{\langle r^3 \rangle} \vec{s} \cdot \vec{\ell}$$

The relativistic correction due to the rotation of the electron's rest frame halves the magnitude of this interaction[8]. For a multielectron ion for which L and S are good quantum numbers the spin-orbit interaction can be written as

$$\mathcal{H}_{LS} = \lambda \vec{L} \cdot \vec{S} \qquad 3\text{-}2$$

$\mathcal{H}_{SS}$ is the spin-spin interaction between the ion's electrons. The interaction energy between two dipoles with magnetic moments $\vec{\mu}_1$ and $\vec{\mu}_2$ and separation $\vec{r}$ is

$$\mathcal{H} = \frac{\vec{\mu}_1 \cdot \vec{\mu}_2}{r^3} - \frac{3(\vec{\mu}_1 \cdot \vec{r})(\vec{\mu}_2 \cdot \vec{r})}{r^5}$$

In the present case $\vec{\mu}_i = -2\beta \vec{s}_i$ and so

$$\mathcal{H}_{SS} = \sum_{i<j} 4\beta^2 \{ \frac{\vec{s}_i \cdot \vec{s}_j}{r_{ij}^3} - \frac{3(\vec{r}_{ij} \cdot \vec{s}_i)(\vec{r}_{ij} \cdot \vec{s}_j)}{r_{ij}^5} \}$$

It can be shown that for a multielectron ion in its ground state the above expression can be written as[9]

$$\mathcal{H}_{SS} = -\rho \, (\vec{L} \cdot \vec{S})^2 + \tfrac{1}{2}(\vec{L} \cdot \vec{S}) - 1/3 \; L(L+1)S(S+1) \qquad 3\text{-}3$$

where ρ is a proportionality constant

$\mathcal{H}_{Ze}$ is the electronic Zeeman term $\beta \vec{H} \cdot (\vec{L} + 2\vec{S})$

$\mathcal{H}_{SI}$ is the interaction between the nuclear magnetic moment and the magnetic field resulting from the electronic orbital motion and the electronic spin magnetic moment. The magnetic field at the nucleus due to an electron's motion is

$$\vec{H} = \frac{\vec{v} \times \vec{E}}{c} = \frac{\vec{v}}{c} \times \frac{(-e\vec{r})}{r^3} = \frac{e}{cr^3} (\vec{r} \times \vec{v}) = \frac{e\hbar}{mcr^3} \vec{\ell} \text{ , and}$$

so the orbital contribution to $\mathcal{H}_{SI}$ is

$\mathcal{H}_a = g_n \beta_n \vec{I} \cdot 2\beta \sum_k \vec{\ell}_k / r^3$. The electronic spin-nuclear spin interaction is a dipole-dipole interaction, therefore its contribution is given by

$$\mathcal{H}_b = 2g_n \beta_n \beta \sum_k \left[\frac{-\vec{s}_k \cdot \vec{I}}{r_k^3} + \frac{3(\vec{s}_k \cdot \vec{r}_k)(\vec{I} \cdot \vec{r}_k)}{r_k^5} \right]$$

$$= 2g_n \beta_n \beta \left\langle \frac{1}{r^3} \right\rangle \left[-\vec{S} \cdot \vec{I} + 3(\vec{S} \cdot \hat{r})(\vec{I} \cdot \hat{r}) \right]$$

It can be shown that for a multielectron ion in its ground state[10]

$$\mathcal{H}_b = \frac{2g_n\beta_n\beta}{\langle r^3\rangle} \zeta[L(L+1)(\vec{I}.\vec{S}) - 3/2(\vec{L}.\vec{I})(\vec{L}.\vec{S}) - 3/2\ (\vec{L}.\vec{S})(\vec{L}.\vec{I})]$$

where ζ is a proportionality constant.

An s-electron has a finite probability of being found at the ion's nucleus. Because of the small size of the nucleus the electron density there is almost constant and hence the nucleus is essentially residing in a uniformly magnetized medium due to the electron's spin. The magnetization is $\vec{M} = (N)(\vec{m}) = (|\psi(0)|^2)(-2\beta\vec{s})$ where N is the density of the magnetic dipoles $\vec{m}$ in the medium. The interaction energy is[11]

$$\mathcal{H}_c = -\vec{\mu}_N.\vec{B} = -8\pi/3\ \vec{\mu}_N.\vec{M} = 8\pi/3\ (2g_n\beta\ \beta_n|\psi(0)|^2\vec{I}.\vec{s})$$

It has been found[12] that for a $3d^n$ electron configuration the valence electrons effect inner s electrons with spin up differently from those with spin down, resulting in a nonzero electron density at the nucleus with the interaction energy being proportional to

$$\frac{2\beta g_n\beta_n}{\langle r^3\rangle}\ \vec{I}.\vec{S}.$$ [13]

The interaction between the magnetic moment of the nucleus and the magnetic field due to the electrons can be written as

$$\mathcal{H}_{SI} = \mathcal{H}_a + \mathcal{H}_b + \mathcal{H}_c = \frac{2\beta g_n \beta_n}{\langle r^3 \rangle} \{ \vec{L}.\vec{I} + \zeta(L(L+1)(\vec{S}.\vec{I}) - 3/2\ (\vec{L}.\vec{I})(\vec{L}.\vec{S}) - 3/2\ (\vec{L}.\vec{S})(\vec{L}.\vec{I})) - K(\vec{S}.\vec{I}) \} \quad 3\text{-}4$$

K is a measure of the nonzero electron density at the nucleus.

$\mathcal{H}_Q$ represents the electrostatic interaction between the nuclear electric quadrupole moment and the ion's electrons. The electron-nucleus electrostatic interaction can be described by

$$\mathcal{H}' = \int \rho_n(r_n)\ V(r_n) d\tau_n$$

where $V(r_n)$ is the potential at a point r_n within the nucleus due to the valence electrons and $\rho_n(r_n)$ is the density of nuclear charge. A Taylor series expansion about the origin yields

$$\mathcal{H} = V(0)\int \rho_n(r_n) d\tau_n + \sum_i \frac{\partial V(0)}{\partial x_i} \int \rho_n(r_n) x_i\ d\tau_n + \frac{1}{2} \sum_{i,j} \frac{\partial^2 V(0)}{\partial x_i \partial x_j} \int \rho_n(r_n) x_i x_j d\tau_n + \ldots.$$

The third term, called the quadrupole term, can be written as[14]

$$\mathcal{H}_Q = \frac{eQ}{4I(2I-1)} \{ V_{zz} (3I_z^2 - I(I+1) + (V_{xx} - V_{yy})(I_x^2 - I_y^2) \}$$

where

$$V_{xx} = \frac{\partial^2 V}{\partial x^2}\ ,\quad V_{yy} = \frac{\partial^2 V}{\partial y^2}\ ,\quad V_{zz} = \frac{\partial^2 V}{\partial z^2}$$

and Q is the nuclear electric quadrupole moment. Q is defined by the equation

$$Q = 1/e \int \rho_n(r_n) r_n^2 (3\cos^2\theta - 1) d\tau_n$$

where

e is the proton charge

θ is the angle between r_n and the spin axes z.

In an axial symmetric field $V_{xx} = V_{yy}$ and so

$$\mathcal{H}_Q = \frac{3eQ}{4I(2I-1)} V_{zz} (I_z^2 - 1/3\ I(I+1)) \qquad 3\text{-}5$$

The nucleus also experiences an electric field due to inner atomic electrons whose orbits have been distorted by the electric field gradients of the outer electrons. This effect is expressed by multiplying Q by the Sternheimer antishielding factor $(1 - \gamma_\infty)$, which for $^{53}Cr^{3+}$ is 12.0 ± 1.0. It is convenient to define a nuclear quadrupole interaction constant Q' by the equation

$$Q' = \frac{3V_{zz}\ eQ}{4I(2I-1)} (1 - \gamma_\infty)$$

For $^{53}Cr^{3+}$ the nuclear spin is I = 3/2 and so in this case Q' is given by

$$Q' = 3V_{zz}eQ \qquad 3\text{-}6$$

$\mathcal{H}_{Zn}$ represents the nuclear Zeeman effect $-g_n\beta_n \vec{H}.\vec{I}$

(2) Spin Hamiltonian

In ESR work one is interested in a group of electron states which are within a few inverse centimeters of the ground state. This group is referred to as the ground manifold. It is separated from the higher electronic levels by several hundred inverse centimeters. Because the general theoretical Hamiltonian is very difficult to apply directly in ESR work, an effective Hamiltonian is used to describe the observed resonance transitions. This effective Hamiltonian is called the spin Hamiltonian because it consists of spin operators which operate on the effective electronic spin. The spin Hamiltonian also contains spin operators which take into account nuclear interactions that make a measureable contribution to the spectrum. For Cr^{3+} and VO^{2+} the effective spin is equal to the real spin of the Cr^{3+} and VO^{2+} ground states.

The ground manifold is the lowest energy state of the Hamiltonian $\mathcal{H}_o + \mathcal{H}_{LF}$. If the ground manifold is an orbital singlet then the orbital operators in the general theoretical Hamiltonian will relate states in the ground manifold to higher states, hence the spin Hamiltonian in the orbital singlet case should not contain any orbital momentum operators. In the case of orbital degeneracy the ground manifold is the lowest energy state of the Hamiltonian $\mathcal{H}_o + \mathcal{H}_{LF} + \mathcal{H}_{LS}$.

The remaining terms in the general theoretical Hamiltonian are expressed in the spin Hamiltonian in a modified form describing an effective spin-spin interaction $\mathcal{H}'_{SS}$, an electronic Zeeman term $\mathcal{H}'_{Ze}$, a spin-nuclear quadrupole term $\mathcal{H}'_{Q}$, and a nuclear Zeeman term $\mathcal{H}'_{Zn}$.

The spin Hamiltonian

$$= \mathcal{H}_{Ze} + \mathcal{H}_{SS} + \mathcal{H}_{SI} + \mathcal{H}_{Q} + \mathcal{H}_{Zn}$$

now has the form

$$\mathcal{H} = \beta g_{ij} H_i S_j + D_{ij} S_i S_j + A_{ij} S_i I_j + P_{ij} I_i I_j - g_{n_{ij}} \beta_n H_i I_j \qquad 3\text{-}7$$

The tensors g_{ij}, D_{ij}, A_{ij}, P_{ij}, and $g_{n_{ij}}$ reflect the symmetry of the ligand field and the effect which higher energy states have on the ground manifold. When the ligand field is axially symmetric the spin Hamiltonian is written as

$$\begin{aligned} H = {} & g_{//} \beta H_z S_z + g_{\perp} \beta (H_x S_x + H_y S_y) + 3/2\, D_{zz} (S_z^2 - 1/3\, S(S+1)) \\ & + A_{//} S_z I_z + A_{\perp} (S_x I_x + S_y I_y) + 3/2\, P_{zz} (I_z^2 - - 1/3\, I(I+1)) \\ & - g_{n_{//}} \beta_n H_z I_z - g_{n_{\perp}} \beta_n H_z I_z \end{aligned} \qquad 3\text{-}8$$

It is found in most cases that the principle axes of g_{ij}, D_{ij}, A_{ij}, P_{ij}, and $g_{n_{ij}}$ coincide. It is customary to refer to $3/2\, D_{zz}$ as D, $A_{//}$ as A, $A_{\perp}$ as B, and $3/2\, P_{zz}$ as $P_{//}$. It can be shown that $P_{//}$ and Q' are identical[15,16].

(3) A Description of the Spin Hamiltonian Parameters

A simple description of the spin Hamiltonian parameters is obtained from perturbation theory. The results of applying perturbation theory to the general theoretical Hamiltonian depend on whether the ground manifold of an atom is orbitally nondegenerate or degenerate, but only the former case is considered here. In the work of Abragam and Pryce[17a,17b,17c] the following theoretical Hamiltonian parameters are derived:

$$g_{ij} = 2.0023(\delta_{ij} - \lambda\Omega_{ij}) \qquad 3\text{-}9$$

$$D_{ij} = -\lambda^2 \Omega_{ij} - \rho\ell_{ij} \qquad 3\text{-}10$$

$$A_{ij} = -P(K\delta_{ij} + 3\zeta\ell_{ij} + 2\lambda\Omega_{ij} - 3\zeta\lambda u_{ij}) \qquad 3\text{-}11$$

$$P_{ij} = q'\ell_{ij} \qquad 3\text{-}12$$

$$g'_{n_{ij}} = g_n \qquad 3\text{-}13$$

The terms which the spin Hamiltonian parameters are related to are defined as follows:

$$\Omega_{ij} \equiv \sum_{n\neq 0} \frac{\langle 0|L_i|n\rangle\langle n|L_j|0\rangle}{E(n) - E(0)}$$

where n is the excited orbital level 1, 2, 3... and 0 refers to the ground state orbital level of the atom.

$$u_{ij} \equiv -i/2 \; \varepsilon_{ik\ell} \sum_{n\neq 0} \frac{\langle 0|L_\ell|n\rangle\langle n|\, L_jL_k + L_kL_j|0\rangle}{E(n) - E(0)}$$

with $u_{ii} = 0$

$$q' = \frac{\eta e Q}{4I(2I - 1)} V_{zz}$$

$$\ell_{ij} = \tfrac{1}{2}\langle 0 | L_i L_j + L_j L_i | 0 \rangle - 1/3\ L(L + 1)\delta_{ij}$$

with $\ell_{ii} = 0$,

$$P = \frac{2 g_n \beta \beta_n}{\langle r^3 \rangle},$$

where ρ and ζ are the proprtionality constants from equations 3-3 and 3-4.

(4) Effective Nuclear g-value g_n'

Equation 3-13 neglects the effect the electron cloud has in the nucleus when the ion is in a magnetic field. The magnetic field experienced by the nucleus is $H(1 + \sigma)$ where H is the external magnetic field and σ is the shielding parameter. Instead of writing the nuclear Zeeman effect as $g_n \beta_n H(1 + \sigma)$ the factor $(1 + \sigma)$ is included in the nuclear g_n value. The measured nuclear g value is the effective nuclear g_n' which is related to the true nuclear g_n by

$$g_n' = g_n(1 + \sigma) \qquad 3\text{-}15$$

The shielding factor can be expressed in the following form[18]

$$\sigma = -5.84\ \langle 1/r^3 \rangle_{a.u.}\ \Delta g/\lambda \qquad 3\text{-}16$$

where $\langle 1/r^3 \rangle$ is the average value of $1/r^3$ for the electron wave function expressed in atomic units, λ is the spin-orbit coupling parameter expressed in cm^{-1}, and $\Delta g = g_e - 2.0023$, where g_e is the measured electronic g-value.

(5) Crystalline Electric Field, VO^{2+}

When the VO^{2+} vanadyl ion replaces Al^{3+} at the centre of the water octahedron the hydrated complex $VO^{2+}.5H_2O$ is formed. The V-O bond, which is shorter than the V-H_2O bonds, imposes a tetragonal distortion on the octahedron. Figures 3-1a and 3-1b compare $Al^{3+}.6H_2O$ with $VO^{2+}.5H_2O$. In $VO(SO_4)5H_2O$ the V-O bond length is 1.67 $\mathring{A}$ [19]. The ground state of VO^{2+} is $^2D_{3/2}$. According to the bonding scheme of Bellhausen and Gray[19] the ground state orbital of V^{4+}, the 3d' electron, is non-bonding. Figure 3-2 summarizes how the d-orbitals split in an octahedral crystal field with a tetragonal distortion. Since over 99% of vanadium has a nuclear spin of 7/2, the hyperfine interaction splits the single ground state into eight energy levels.

(6) Crystalline Electric Field, Cr^{3+}

The electronic configuration of Cr^{3+} is $3d^3$, therefore the ground state of a free Cr^{3+} ion is $^4F_{3/2}$, indicating the orbital quantum number is L = 3, the spin is S = 3/2, and the total angular momentum

Figure 3-1 Diagrams of the $Al^{3+}.6H_2O$ complex and the $VO^{2+}.5H_2O$ complex.

(a)

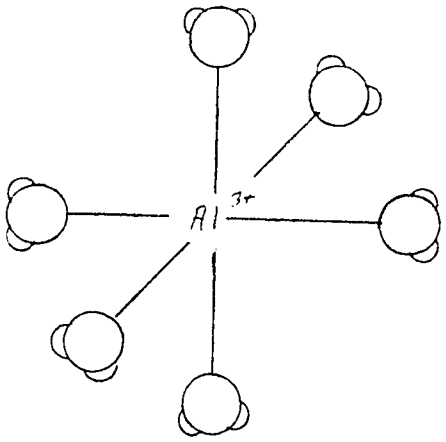

(b)

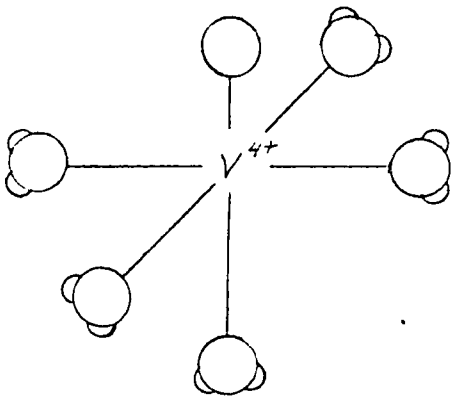

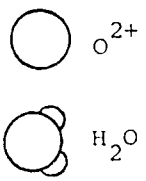

Figure 3-2: Splitting of the $^2D_{3/2}$ state of V^{4+} by the cubic and tetragonal components of the crystal field.

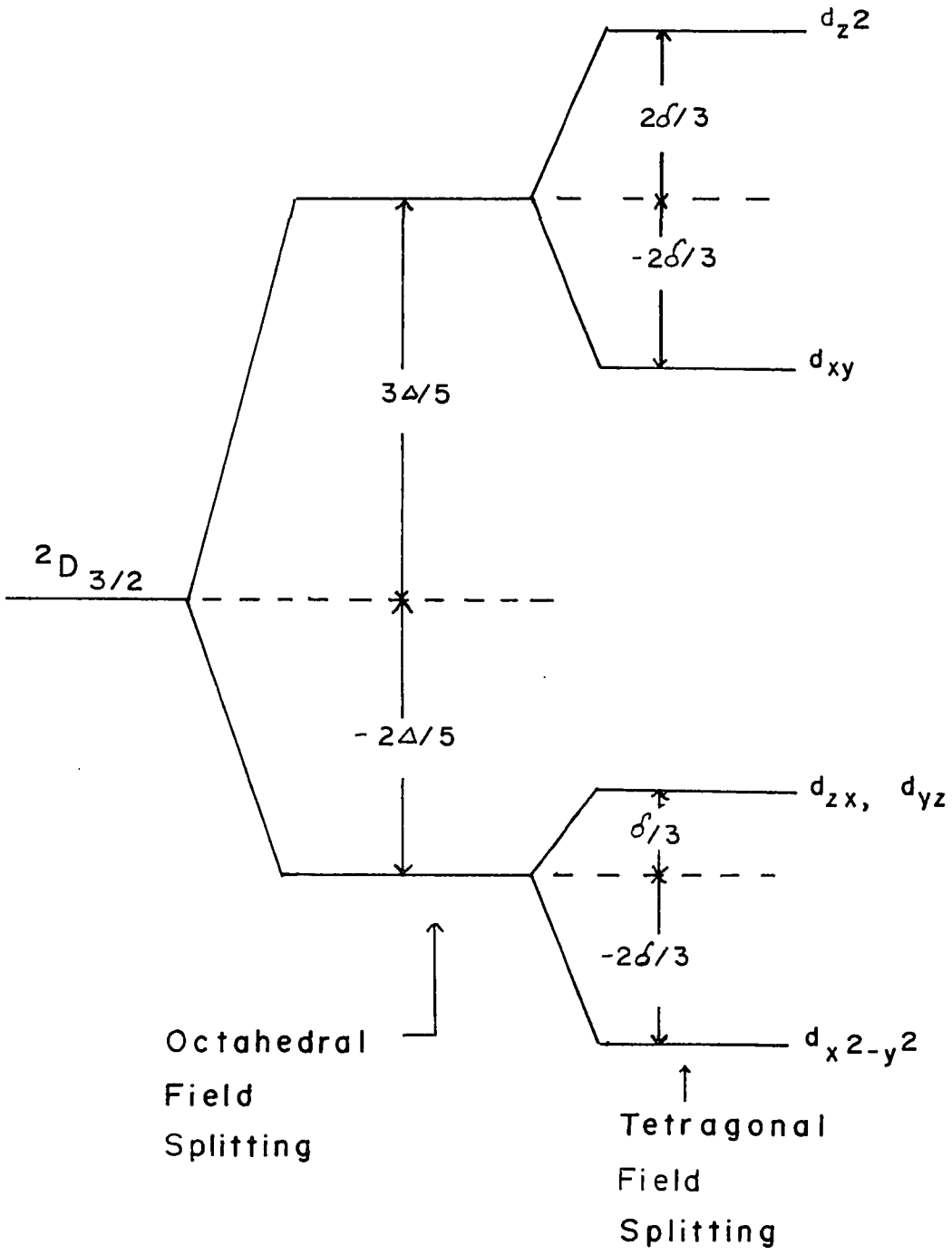
d_{z^2}
$2\delta/3$
$-2\delta/3$
d_{xy}
$3\Delta/5$
$^2D_{3/2}$
$-2\Delta/5$
d_{zx}, d_{yz}
$\delta/3$
$-2\delta/3$
$d_{x^2-y^2}$
Octahedral
Field
Splitting
Tetragonal
Field
Splitting

quantum number is J = 3/2. When a $^4F_{3/2}$ state ion is in an octahedral crystal field the orbital wave functions are split into a triplet of states as shown in Figure 3-3.

The ground state in the octahedral field is an orbital singlet with a 4-fold spin degeneracy. When the octahedral field is trigonally distorted the first excited state splits into a singlet and a doublet. Spin-orbit coupling mixes this effect into the ground state, causing a splitting of the ground state into two doubly degenerate spin states. The spin Hamiltonian parameter D is a measure of this splitting. Figure 3-4 shows the two possible ways in which the ground state can be split. The remaining spin degeneracy is removed when a magnetic field is applied.

There are theoretical expressions for the spin Hamiltonian parameters, D, A, and B of Cr^{3+} in an axially symmetric crystal field. O'Reilly and Tsang expressed the fine structure zero field splitting parameter D in the following form[20]

$$D = (3/7)\ (\lambda/\Delta E)\ \langle r^2 \rangle\ V_{zz} \qquad 3\text{-}17$$

where ΔE is the energy difference between the ground state and the first excited state $\langle r^2 \rangle$ is the average of r^2 for the Cr^{3+} 3d wave function.

McGarvey found the following expressions for the hyperfine constants A and B'[21].

$$A = P(4/21(1 - 2a^2 + b^2) - K) \qquad 3\text{-}18$$

$$B = P(-2/21(1 - 2a^2 + b^2) - K) \qquad 3\text{-}19$$

Figure 3-3: Splitting of the $^4F_{3/2}$ state of Cr^{3+} by cubic and trigonal components of the crystal field.

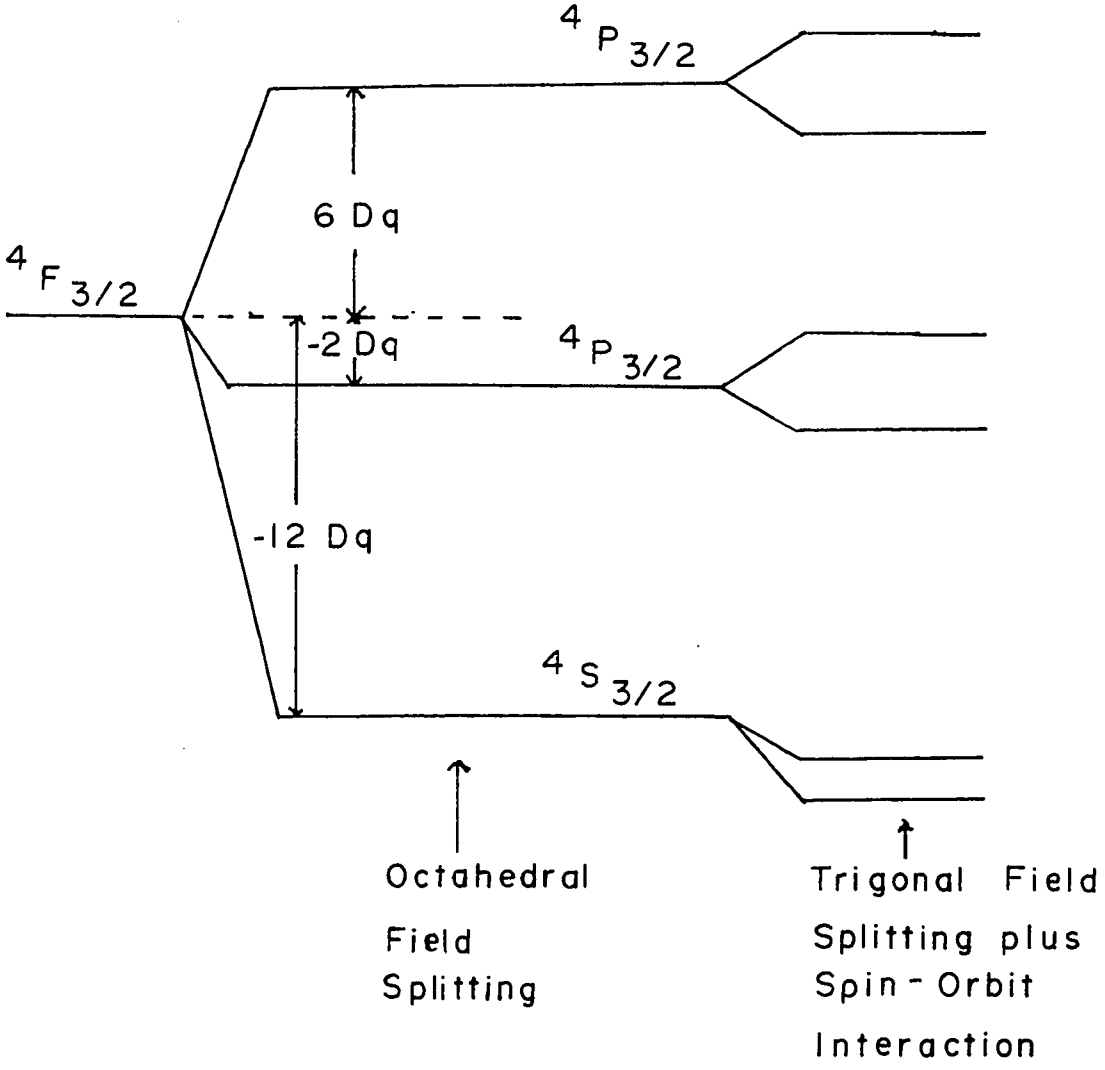
$^4P_{3/2}$
6 Dq
$^4F_{3/2}$
-2 Dq
$^4P_{3/2}$
-12 Dq
$^4S_{3/2}$
Octahedral
Field
Splitting
Trigonal Field
Splitting plus
Spin - Orbit
Interaction

Figure 3-4: Energy level diagram showing the two possible ways the $^4S'_{3/2}$ state can split due to the trigonal component of the crystal field.

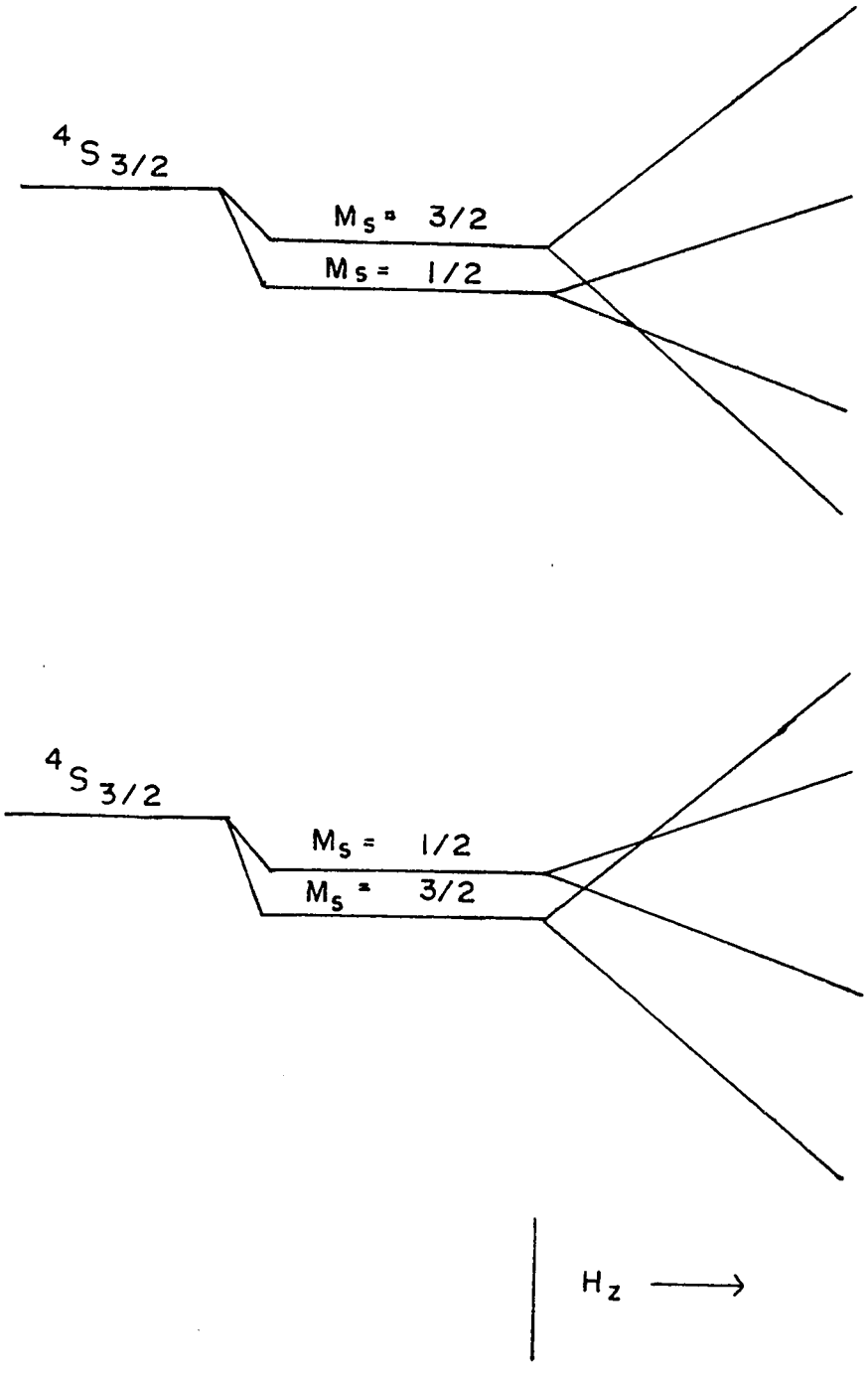
$^4S_{3/2}$
$M_S = 3/2$
$M_S = 1/2$
$^4S_{3/2}$
$M_S = 1/2$
$M_S = 3/2$
$H_z \longrightarrow$

where a and b are coefficients of the d wave functions used in the construction of the electronic wave functions. For Cr^{3+}, P is approximately $-40 \times 10^{-4} cm^{-1}$. In the case of octahedral symmetry for the six waters surrounding the Cr^{3+} ion, $a^2 = 2/3$ and $b^2 = 1/3$. When $a^2 < 2/3$ and $b^2 > 1/3$ there is a trigonal compression of the octahedron and A-B is negative. When $a^2 > 2/3$ and $b^2 < 1/3$ there is an extension of the octahedron and A-B is positive.

(7) Application of the Spin Hamiltonian

The allowed spectral lines observed in ESR occur when the selection rules $\Delta M_S = 1$ and $\Delta M_I = 0$ are satisfied. For the ESR work covered in this thesis the spin Hamiltonian of an axial symmetric system, the z axis of which makes an angle Θ with an external magnetic field, is described by the expression

$$\mathcal{H} = g\beta H S_z + D/2\,(3(g_{\parallel}/g_{\perp})^2 \cos^2\Theta - 1)(S_z - 1/3\,S(S+1))$$

$$- Dg_{\parallel} g_{\perp}/g^2 \sin\Theta\cos\Theta\,(S_x S_z + S_z S_x)$$

$$+ (D/2)(g_{\perp}/g)^2 \sin\Theta\,(S_x^2 - S_y^2) + KS_z I_z + BS_y I_y + \frac{AB}{K} S_x I_x$$

$$+ \frac{B^2 - A^2}{2K} g_{\parallel} g_{\perp}/g^2 \sin 2\Theta\, S_x I_z \qquad 3\text{-}20$$

The parameters g and K are defined by the following two expressions:

$$g = g_{\perp} \sin\Theta \sin\alpha + g_{//} \cos\Theta \cos\alpha$$

$$gK = A\, g_{//} \cos\Theta \cos\gamma + B g_{\perp} \sin\Theta \sin\gamma$$

where α and γ are the angles which the electron spin $\vec{S}$ and nuclear spin $\vec{I}$ make with the z axis of symmetry, respectively.

(7a) Application of the Spin Hamiltonian to the VO^{2+} System

For an electron spin 1/2 system, such as VO^{2+}, the fine structure term drops out. Applying second order perturbation theory to equation 3-20 the two electronic spin energy levels of VO^{2+} are given by

$$E(M_S = \pm 1/2) = \pm 1/2\, g\beta H \pm 1/2 K M_I - \frac{AB^2 M_I}{4g\beta HK}$$

$$\pm \frac{B^2(A^2 + K^2)}{8g\beta HK^2} (I(I+1) - M_I^2)$$

$$\pm \frac{(A^2 - B^2)^2}{4g\beta H} \left(\frac{g_{//}\, g_{\perp}}{2g^2 K} \sin 2\Theta\right)^2 M_I^2 \qquad 3\text{-}21$$

where the plus sign applies for $M_S = 1/2$, and the minus sign applies for $M_S = -1/2$

When $\Theta = 0$ then $g = g_{//}$ and $K = A$, and the transition energy

obtained when the applied magnetic field is parallel to the axis of symmetry is

$$E(M_S = 1/2) - E(M_S = -1/2) = h\nu = g_{//}\beta H + AM_I + \frac{B^2(I(I+1) - M_I^2)}{2g_{//}\beta H} \qquad 3\text{-}22$$

when $\theta = \pi/2$ then $g = g_\perp$ and $K = B$, and the transition energy obtained when the applied magnetic field is perpendicular to the axis of symmetry is

$$E(M_S = 1/2) - E(M_S = -1/2) = h\nu = g_\perp \beta H + BM_I + \frac{A^2 + B^2}{4g_\perp \beta H}(I(I+1) - M_I^2) \qquad 3\text{-}23$$

(7b) Application of the spin Hamiltonian to the Cr^{3+} System

For $^{52}Cr^{3+}$ the nuclear spin is $I = 0$ and so the hyperfine terms do not exist. Thus when the magnetic field is in the z direction the energy levels are described by

$$\mathcal{H} = g_{//}\, 3HS_z + D(S_z^2 - 5/4) \qquad 3\text{-}24$$

The ESR transitions are described by

$M_s \rightarrow M_S + 1$

$-3/2 \rightarrow -1/2$	$H_1 = H_o + 2D$	3-25a
$-1/2 \rightarrow 1/2$	$H_2 = H_o$	3-25b
$1/2 \rightarrow 3/2$	$H_3 = H_o - 2D$	3-25c

where H_1, and H_2 and H_3 are the magnetic field positions of the resonance lines. H_o is defined by

$$H_o = h\nu/g_{//}\beta \qquad 3\text{-}25d$$

where ν is the microwave frequency.

When the magnetic field is perpendicular to the axis of symmetry the energy levels are described by

$$\mathcal{H} = g_\perp \beta H_\perp S_z + D/2(2S_x^2 - 5/2) \qquad 3\text{-}26$$

The diagonalized matrix of the above Hamiltonian has the following four eigenvalues

$$E(3/2) = 1/2g_\perp \beta H_\perp + \sqrt{(g_\perp \beta H_\perp - D/2)^2 + 3D^2/4}$$

$$E(1/2) = -1/2g_\perp \beta H_\perp + \sqrt{(g_\perp \beta H_\perp + D/2)^2 + 3D^2/4}$$

$$E(-1/2) = 1/2\, g_\perp \beta H_\perp - \sqrt{(g_\perp \beta H_\perp - D/2)^2 + 3D^2/4}$$

$$E(-3/2) = -1/2g_{\perp}\beta H_{\perp} - \sqrt{(g_{\perp}\beta H_{\perp} + D/2)^2 + 3D^2/4}$$

where the bracked quantities (3/2), etc., refer to the M_S values. The ESR transitions are described by

$$M_S \rightarrow M_S + 1$$

$$-3/2 \rightarrow -1/2 \qquad h\nu' = g_{\perp}\beta H_{\perp} - \sqrt{(g_{\perp}\beta H_{\perp} - D/2)^2 + 3D^2/4} + \sqrt{(g_{\perp}\beta H_{\perp} + D/2)^2 + 3D^2/4} \qquad 3\text{-}27a$$

$$-1/2 \rightarrow 1/2 \qquad h\nu' = -g_{\perp}\beta H_{\perp} + \sqrt{(g_{\perp}\beta H_{\perp} + D/2)^2 + 3D^2/4} + \sqrt{(g_{\perp}\beta H_{\perp} - D/2)^2 + 3D^2/4} \qquad 3\text{-}27b$$

$$1/2 \rightarrow 3/2 \qquad h\nu' = g_{\perp}\beta H_{\perp} + \sqrt{(g_{\perp}\beta H_{\perp} - D/2)^2 + 3D^2/4} - \sqrt{(g_{\perp}\beta H_{\perp} + D/2)^2 + 3D^2/4} \qquad 3\text{-}27c$$

At thermal equilibrium the ratio of populations between a lower energy state and an upper state is

$\frac{N_L}{N_u} = \exp(\Delta E/kT)$ where ΔE is the energy between the two states

For $M_S = \pm 1$ transitions we have $\frac{N_L}{N_u} = \exp(g\beta H/kT)$. Using $g \simeq 2$, $H \simeq 3 \times 10^3$ gauss one obtains for $T \simeq 300^{\circ}K$

$$N_L/N_u \simeq 1.0013; \text{ for } T \simeq 4\ ^{\circ}K \quad N_L/N_u \simeq 1.11$$

(8) ESR Transitions

ESR absorption between two energy levels depends on the existence of a difference in population between the levels. In order for the absorbed energy to be dissipated so that the electrons can return to the ground state, there must be a relaxation process. In this case the most important relaxation process is the spin-lattice interaction. Thermal vibrations in the lattice cause the crystalline electric field to oscillate, resulting in an interaction with the ion's spin via L-S coupling. The three principal spin-lattice interaction processes, direct emission of a phonon, phonon scattering, and a two stage phonon process, are temperature dependent[22]. The spin-lattice relaxation time is also dependent on the energy separation between the ground and first excited state[23]; and for a large separation the spin-lattice relaxation time is long.

If only spin-lattice interactions were present the spectral lines would be Lorentzian[24]; however, there are spin-spin interactions between different paramagnetic ions which broaden the line. The magnetic field experienced by a particular ion is the sum of the fields due to the

applied field and those of neighbouring magnetic ions. Thus an ESR transition covers a band of frequencies. A spectral line broadened due to pure spin-spin interaction is Gaussian[25].

(9) ENDOR Transitions

The hyperfine interaction is the interaction between the electrons and nucleus. Figure 3-5 shows how the electronic energy levels of $^{53}Cr^{3+}$ are split due to hyperfine interaction. The ENDOR technique involves measuring the spacings between the hyperfine energy levels directly, and the effect of such a resonance absorption is observed via a change in the intensity of the ESR transition. In this procedure one first sets the magnetic field at an ESR transition such as shown in Figure 3-5. The microwave power is then increased so as to partially saturate the transition, hence causing the ESR line to decrease in size. An oscillator, which is coupled to the sample by a few turns of wire, is then swept in frequency through the range corresponding to the spacings between the hyperfine lines at the given field position. When a nuclear resonance is achieved this causes an unbalance in the spin populations of the ESR transition with a consequent increase in the magnitude of the ESR line. The frequencies of the nuclear resonance transitions can then be read from the oscillator.

The ENDOR frequencies are used to measure the hyperfine parameters of $^{53}Cr^{3+}$. To first order in perturbation theory the spin-nuclear

Figure 3-5: Hyperfine splitting of $^{53}Cr^{3+}$.
The broken lines refer to the relative energy levels of ^{52}Cr.

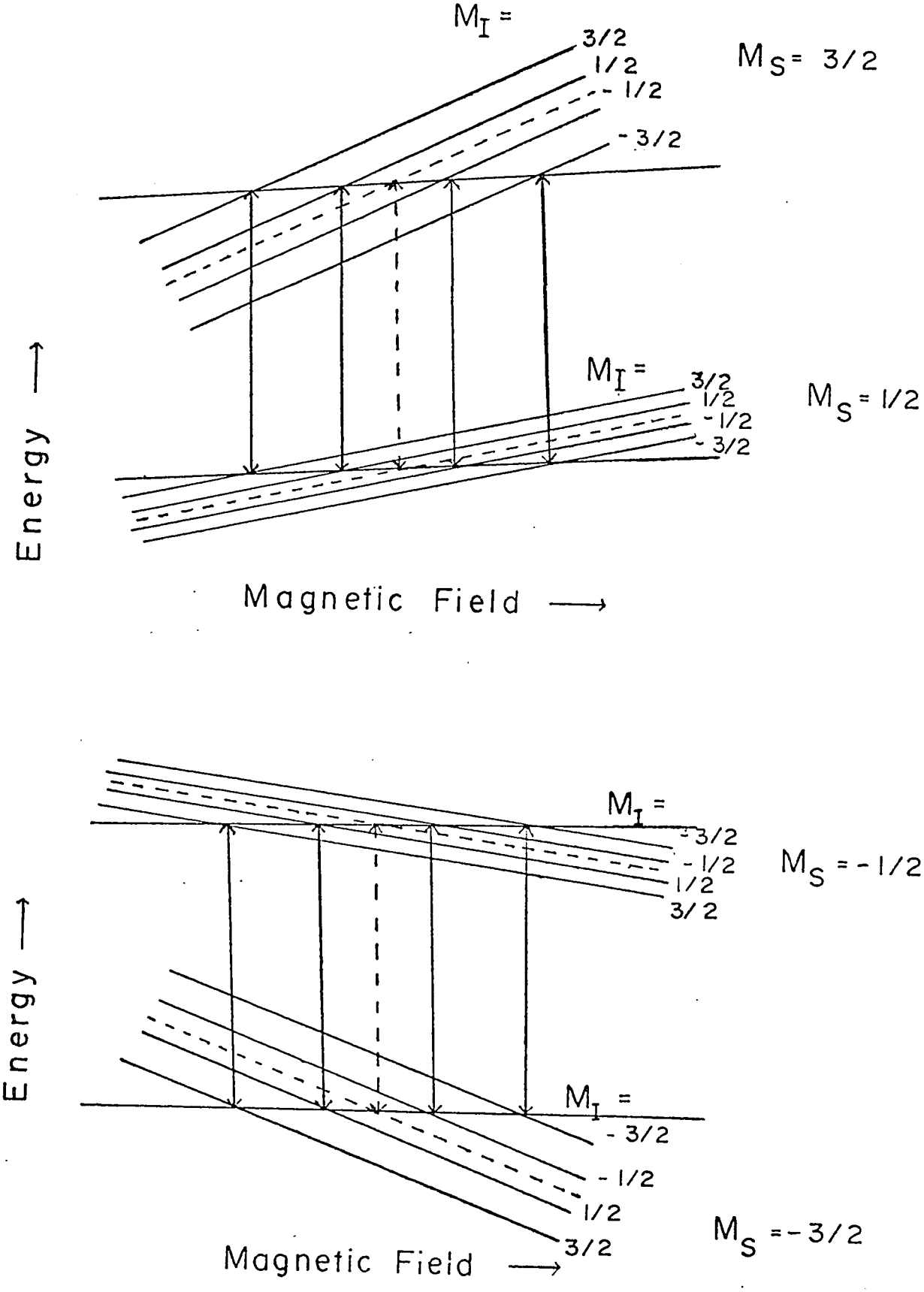
M_I =
3/2
1/2
-1/2
-3/2
M_S = 3/2
M_I =
3/2
1/2
-1/2
-3/2
M_S = 1/2
Energy
Magnetic Field
M_I =
-3/2
-1/2
1/2
3/2
M_S = -1/2
M_I =
-3/2
-1/2
1/2
3/2
M_S = -3/2
Energy
Magnetic Field

interaction can be written as $E = AM_S M_I$. Using second order perturbation theory the energy levels of the ground manifold of $^{53}Cr^{3+}$ in an applied magnetic field along the z direction are described by[26]

$$E(M_S, M_I) = g_{//}\beta H_z M_S + D(M_S^2 - 1/3\ S(S+1)) + AM_S M_I$$

$$- g_n\beta_n H_z M_I + Q'(M_I^2 - 1/3\ I(I+1))$$

$$+ 1/4\ B^2 \frac{(S(S+1) - M_S(M_S+1))(I(I+1) - M_I(M_I-1))}{-g_{//}\beta H_z - D(2M_S+1) + A(M_S - M_I + 1)}$$

$$+ 1/4\ B^2 \frac{(S(S+1) - M_S(M_S-1))(I(I+1) - M_I(M_I-1))}{g_{//}\beta H_z + D(2M_S-1) + A(M_I - M_S + 1)}$$

3-28.

From the above equation the six theoretical ENDOR transitions listed in Table 3-1 can be derived.

The most important factor in ENDOR linewidths is the spin-spin relaxation time[27]. This effect has been maximized in this work because the paramagnetic ions are widely separated in the dilutely doped crystals, hence the ENDOR lines are narrow. The effect of inhomogeneous fields within the crystal is small because the stray fields are perturbing a half a million gauss field set up by the ion's electrons instead of a three kilogauss externally applied field. The spin-lattice interactions do not significantly effect the ENDOR linewidths.

Table 3-1: Theoretical ENDOR Transition Frequencies

For $M_S = 3/2$

$$M_I(1/2 \rightarrow 3/2)h\nu_a = 3/2\ A + 2Q' - g_n\beta_n H_z - \frac{9B^2}{4(2D + g_{//}\beta H_z)}$$

$$M_I(-1/2 \rightarrow 1/2)h\nu_b = 3/2\ A - g_n\beta_n H_z - \frac{3B^2}{4(2D + g_{//}\beta H_z)}$$

$$M_I(-3/2 \rightarrow -1/2)h\nu_c = 3/2\ A - 2Q' - g_n\beta_n H_z + \frac{3B^2}{4(2D + g_{//}\beta H_z)}$$

For $M_S = -3/2$

$$M_I(-1/2 \rightarrow -3/2)h\nu_c = 3/2\ A + 2Q' + g_n\beta_n H_z - \frac{9B^2}{4(2D - g_{//}\beta H_z)}$$

$$M_I(1/2 \rightarrow -1/2)h\nu_b = 3/2\ A + g_n\beta_n H_z - \frac{3B^2}{4(2D - g_{//}\beta H_z)}$$

$$M_I(3/2 \rightarrow 1/2)h\nu_a = 3/2\ A - 2Q' + g_n\beta_n H_z + \frac{3B^2}{4(2D - g_{//}\beta H_z)}$$

CHAPTER IV EQUIPMENT

(1) Introduction

All ESR measurements were done at X-band microwave frequencies ($\sim$ 9.4 GHz). The measurements were made at room temperature (297^{o}K), carbon dioxide sublimation temperature (195^{o}K), liquid nitrogen temperature (77^{o}K), and liquid helium temperature (4.2^{o}K). The first three were done using a commercial spectrometer manufactured by Hilger and Watts Ltd. of England. The ESR and ENDOR measurements made at liquid helium temperature were done using a second X-band spectrometer operating on the superheterodyne principle which was constructed by Danilov and Manoogian[28a, 28b]. All measurements were made in a magnetic field produced by an eight inch Newport magnet.

(2) Commercial Spectrometer

The microwave source used in the commercial spectrometer is a reflex klystron capable of supplying about 35 mW of power[29]. The automatic frequency control (A.F.C.) circuit (see Figure 4-1) stabilizes the frequency output of the klystron. Part of the klystron's output enters arm #1 of magic tee #1, the rest enters the ESR waveguide bridge circuit. Crystal #3 is used to determine the resonance frequency of the ESR bridge circuit and its amplified signal is monitored on the oscilloscope. The reference cavity resonator is then tuned to the resonance frequency of

the ESR bridge circuit.

The magic tee, or hybrid tee, has two properties which are useful in the AFC circuit. One property is that power from the E arm of the magic tee does not directly enter the H arm of the tee, and vice versa. The second property is that microwaves entering via the H arm excite waves of equal amplitude and the same phase in arms #1 and #2 whereas waves entering via the E arm excite waves of equal amplitude but opposite phase in arms #1 and #2. Thus when the klystron frequency drifts from the resonance frequency of the reference cavity the phase relationship between the H arm and arm #2 of magic tee #1 change, causing the resultant waves detected by crystals #1 and #2 to be different. The outputs of crystals #1 and #2 are fed into a differential amplifier which then sends a correction signal to the klystron's reflector.

A sawtooth wavegenerator, which is not shown in Figure 4-1, provides the time base for the cathode ray tube and varies the reflector voltage of the klystron. The latter function is convenient for tuning the klystron, however, when ESR measurements are being made it is disconnected from the klystron's reflector.

In the ESR bridge circuit, the microwave signal enters the E arm of magic tee #3. When electron spin resonance occurs the amount of energy returning from the sample cavity changes, thus unbalancing the magic tee. In order to detect and amplify the signal the external magnetic field is modulated by a 100 kHz signal. After amplification the out-of-balance signal is mixed against the 100 kHZ reference signal

Figure 4-1: A Schematic diagram of the commercial spectrometer.

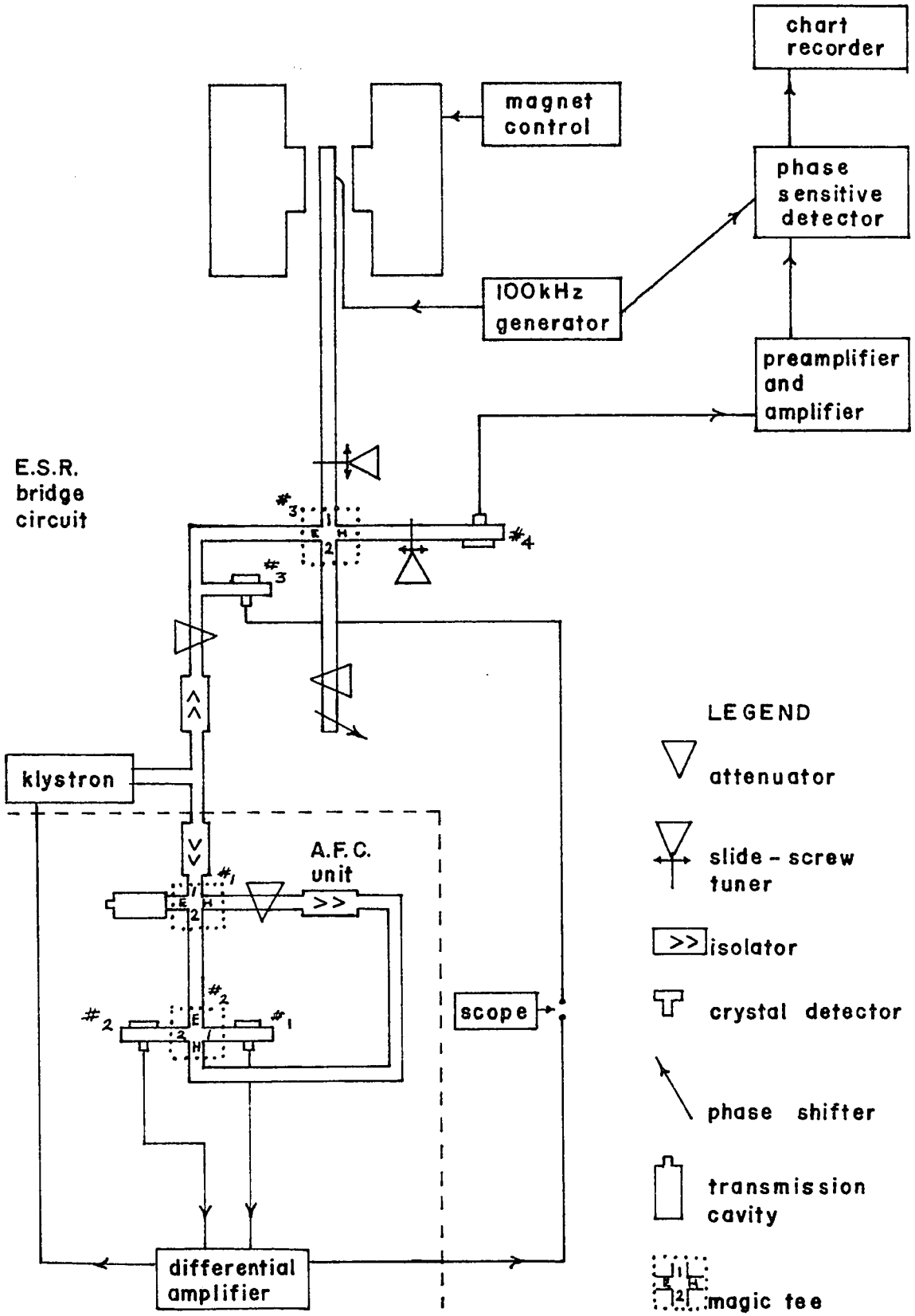
chart recorder
magnet control
phase sensitive detector
100kHz generator
preamplifier and amplifier
E.S.R. bridge circuit
klystron
A.F.C. unit
scope
differential amplifier
LEGEND
attenuator
slide - screw tuner
isolator
crystal detector
phase shifter
transmission cavity
magic tee

resulting in an output proportional to the first derivative of either the absorption or dispersion signal.

(In a high frequency field the magnetization of the sample lags behind the magnetizing field, thus the magnetic susceptibility is in fact $X = X' - iX''$ where the real part of the magnetic susceptibility represents the magnetization in phase with the field, and the imaginary part is the magnetization out of phase with the field. It can be shown that a change in the imaginary part of the magnetic susceptibility results from a change in the amount of energy absorbed by the crystal[30], and a change in the real part results from a frequency change of the resonance cavity[31]. Depending on the balancing of the bridge either change can be detected).

(3) Superheterodyne Spectrometer

In this spectrometer the klystron frequency is automatically stabilized by mixing some of the microwave power with a high harmonic of a crystal oscillator. Comparison of the resulting beat signal with an intermediate reference frequency produces the correction voltage for the klystron. The schematic diagram for this spectrometer is shown in Figure 4-2.

A portion of the klystron's output is used to monitor the klystron's power level (a). After the signal has passed through an isolator and attenuator the circulator sends the signal to the sample

Figure 4-2: A schematic diagram of the superheterodyne spectrometer

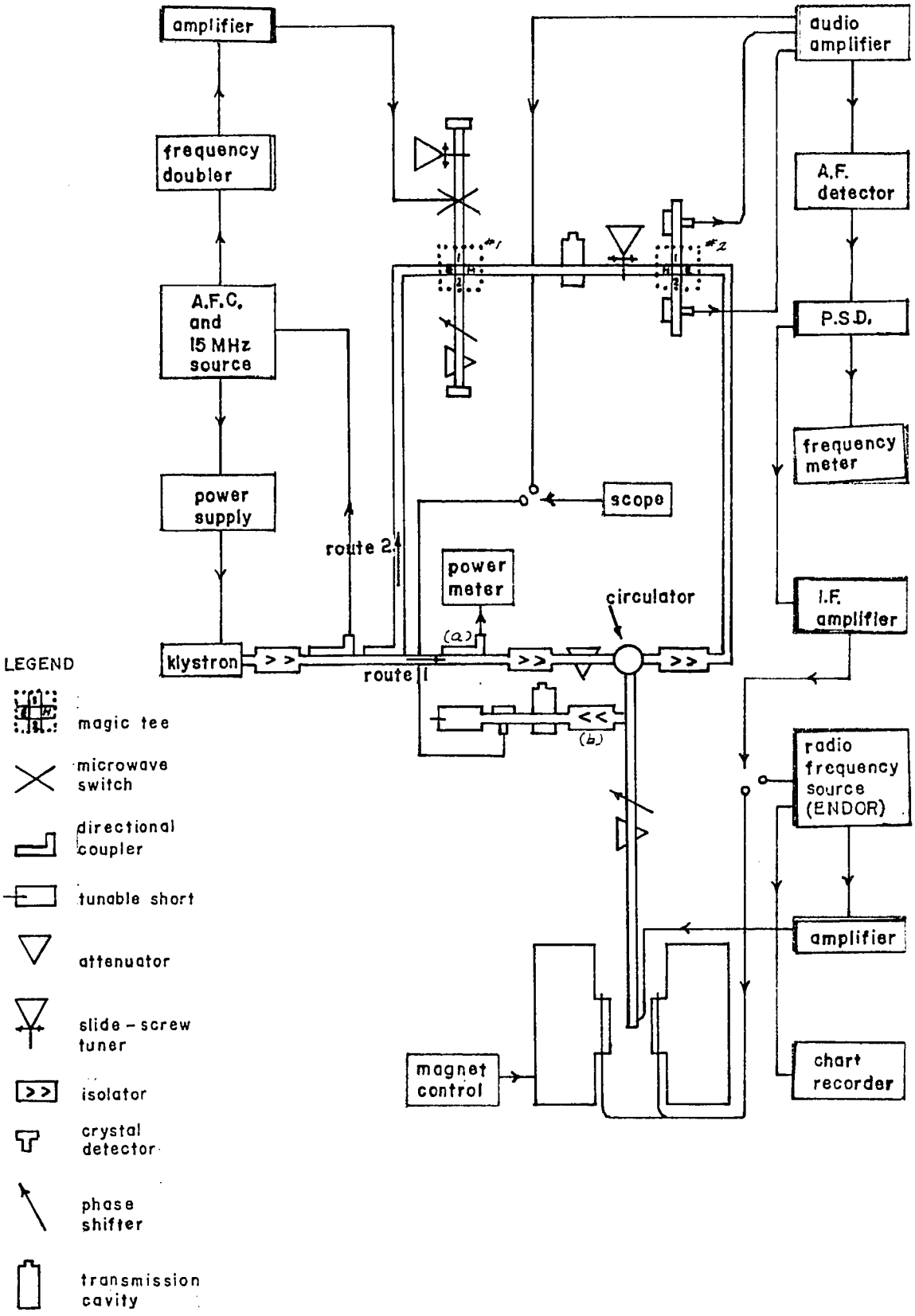
amplifier
frequency doubler
A.F.C. and 15 MHz source
power supply
klystron
route 2
route 1
power meter
scope
circulator
audio amplifier
A.F. detector
P.S.D.
frequency meter
I.F. amplifier
radio frequency source (ENDOR)
amplifier
chart recorder
magnet control
LEGEND
magic tee
microwave switch
directional coupler
tunable short
attenuator
slide - screw tuner
isolator
crystal detector
phase shifter
transmission cavity

cavity. A portion of the microwave signal enters side arm (b) via a directional coupler. Here a resonance cavity acts as a frequency meter and there is a crystal detector for measuring the power output of the sample cavity. Most of the power, however, returns to the circulator which directs the signal to the E arm of magic tee #2.

The portion of the microwave signal which did not travel via route 1 enters magic tee #1 via its E arm. In one arm of the magic tee there is a microwave switch which amplitude modulates the microwave signal. The Fourier spectrum of the resultant signal contains side bands 30 MHz above and below the klystron's frequency.

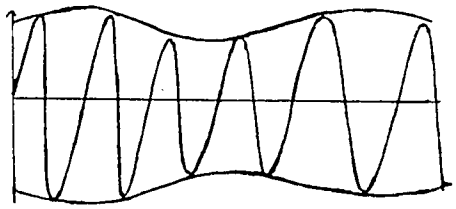

Amplitude Modulated Signal

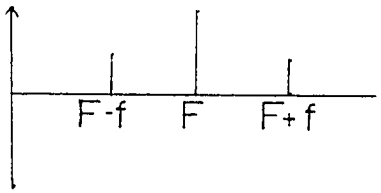

Frequency Representation of a single tone amplitude modulated signal

The slide screw tuner, phase shifter and attenuator control the amount of power which leaves the magic tee via its H arm. One of the side bands, selected by the transmission cavity, acts as a reference signal in magic tee #2. When there is a change in the microwave signal

from the sample cavity the two crystals in magic tee #2 detect different signals. The two signals are mixed and the intermediate frequency is then detected.

When the superheterodyne spectrometer is used the magnetic field is modulated at 200 hz with an amplitude of 5 gauss via Helmholtz coils on the magnet pole faces. Thus the IF signal is amplitude modulated at 200 hz. After amplification, the 200 hz component is detected by a crystal detector, amplified by an audio amplifier, and fed to a phase sensitive detector. A phase sensitive detector, or as it is sometimes called, a lock-in detector, only passes signals which have the proper frequency and arrive in phase with a reference signal. The output of the P.S.D. is the derivative of the absorption or dispersion signal depending on how the bridge has been balanced.

In order to make ENDOR measurements the power to the Helmholtz coils is turned off and the magnetic field position is set on an ESR absorption line, which is then partially saturated by increasing the amount of microwave power into the cavity. The ENDOR signal generator is swept through the frequency range of interest. In order to detect nuclear transitions the RF signal is frequency modulated by the 200 hz signal of the P.S.D. When nuclear transitions occur the bridge is again unbalanced and a 200 hz modulated IF signal is again detected.

Figure 4-3: The effect of modulation. The diagram is drawn for ESR; for ENDOR the horizontal axis becomes frequency.

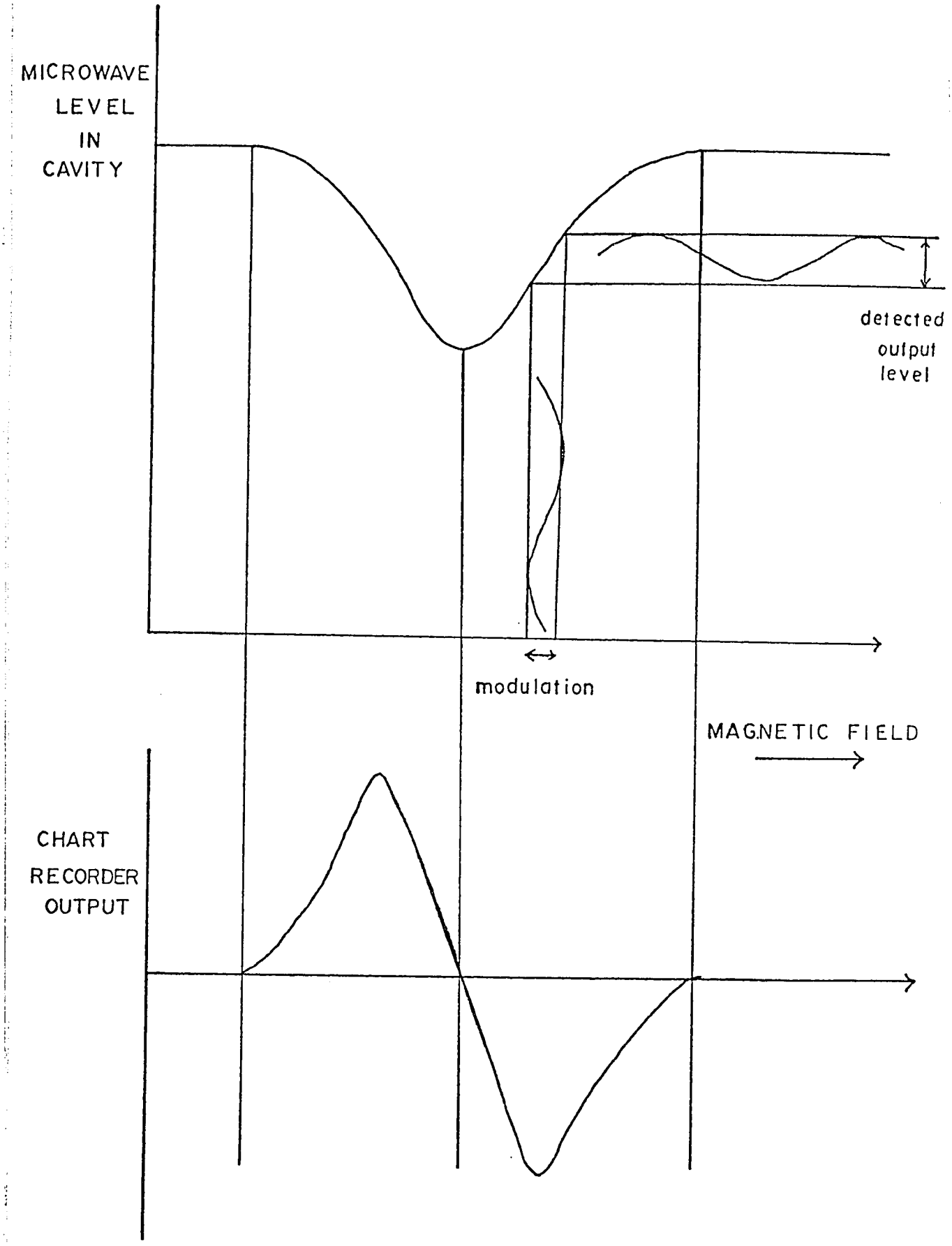
MICROWAVE
LEVEL
IN
CAVITY
detected
output
level
modulation
MAGNETIC FIELD
CHART
RECORDER
OUTPUT

(4) Microwave Cavities

All room temperature measurements were done with a cylindrical cavity operating in the TE_{011} mode. The crystal was placed at the centre of the cavity where the microwave magnetic field is vertical and rotationally invariant. Measurements on the VO^{2+} doped sample were done with a special goniometer type sample holder which allowed the sample to be rotated in the vertical and horizontal planes. The TE_{011} cavity and the special goniometer type sample holder are shown in Figure 4-4.

Low temperature ESR measurements were made with a rectangular cavity operating in the TE_{014} mode, which is shown in Figure 4-5. The magnetic field modulation was provided by a single turn of copper wire, which was parallel to the cavity's wide wall, and hence normal to the microwave magnetic field.

ENDOR measurements were made with a different rectangular cavity which also operated in the TE_{014} mode. The ENDOR cavity is shown in Figure 4-6. All of these cavities were previously used by Danilov[32].

(5) Resonance Frequency Measurements

The microwave frequency was determined by use of calibrated transmission cavities built into the microwave circuits. These cavities could be read to an accuracy of ±2kHz.

The magnetic field was determined by NMR measurements. The NMR sample used was water doped with a paramagnetic salt, the salt

providing a relaxation mechanism to prevent saturation of the NMR signal. The strength of the field was determined from the fact that in a 1 kgauss field the NMR frequency of water protons is 4.25759 MHz. Field measurements were accurate to ±1 gauss.

ENDOR frequency measurements were made with a Hewlett Packard model 5253B frequency converter. The uncertainty of the frequency of an ENDOR line was estimated to be ±5 kHz.

Figure 4-4: Diagram of TE_{011} cavity (for ESR) and special goniometer. H represents the external magnetic field. The r-f field is represented by h. c is the sample. The 100-kHz field modulation inputs are marked M. The calibrated crystal-rotation dials are marked D.

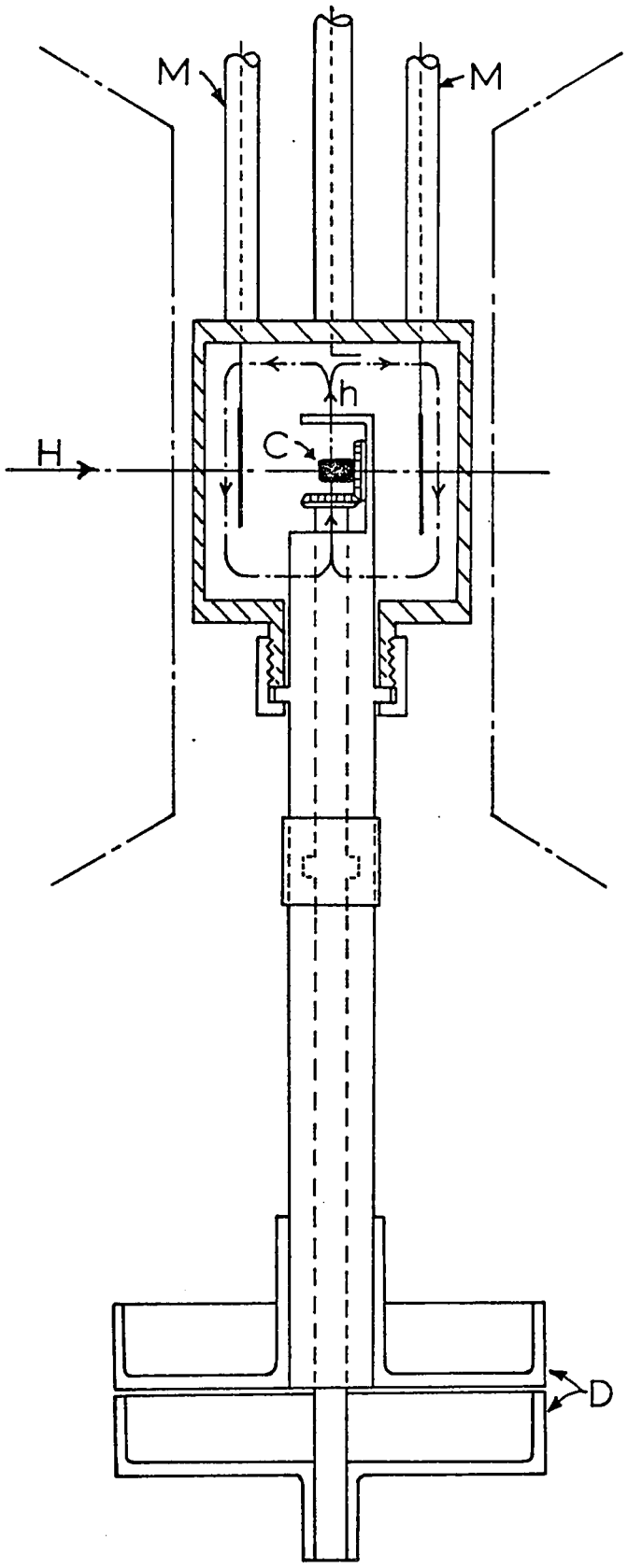
M
M
h
C
H
D

Figure 4-5: Diagram of TE_{014} cavity (for ESR)

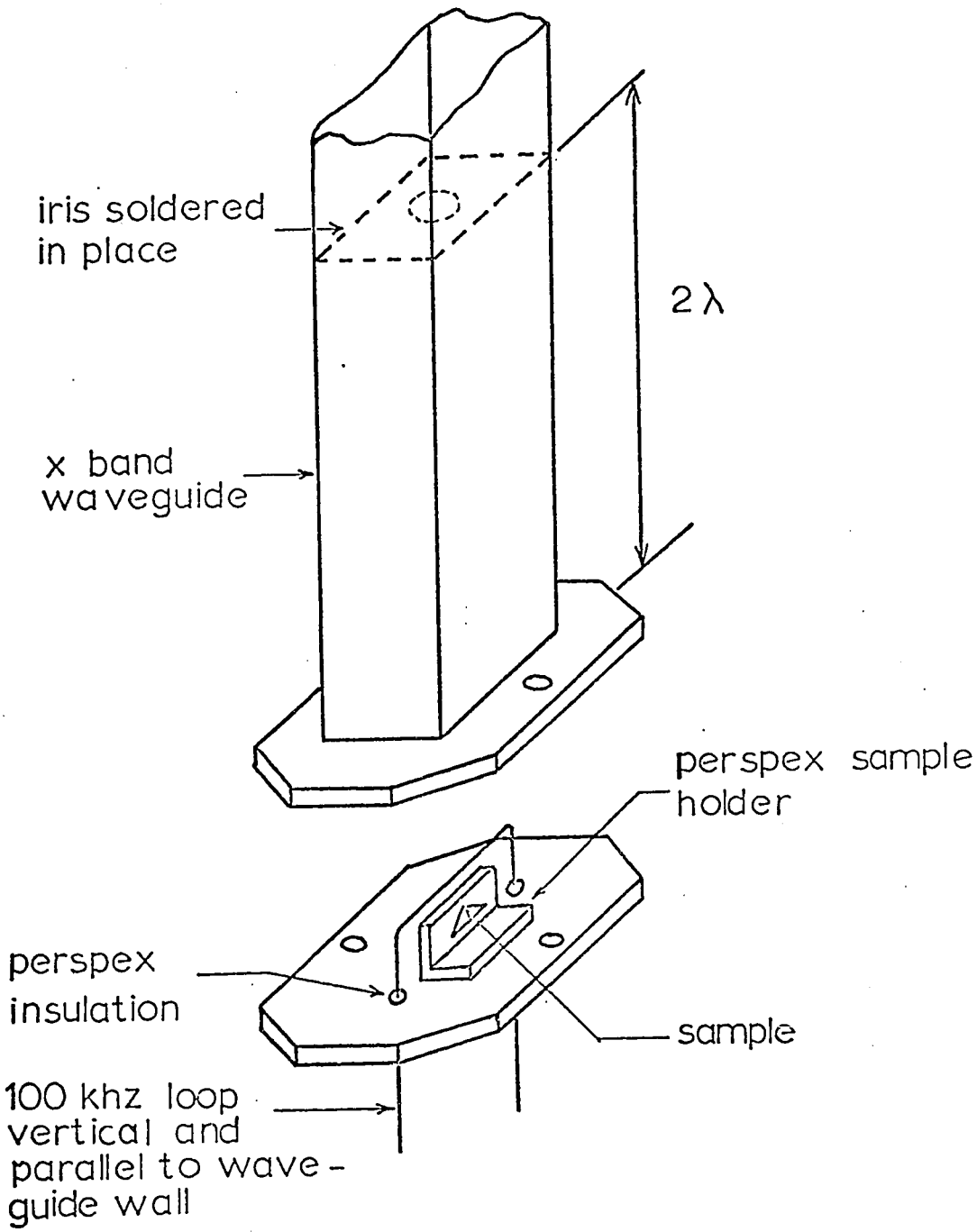
iris soldered
in place
2λ
x band
waveguide
perspex sample
holder
perspex
insulation
sample
100 khz loop
vertical and
parallel to wave-
guide wall

Figure 4-6: Diagram of TE_{014} cavity (ENDOR).
The ENDOR cavity is shown in (a).
The sample holder is shown in (b).
The directions of the external,
microwave, and ENDOR magnetic fields
are shown in (c).

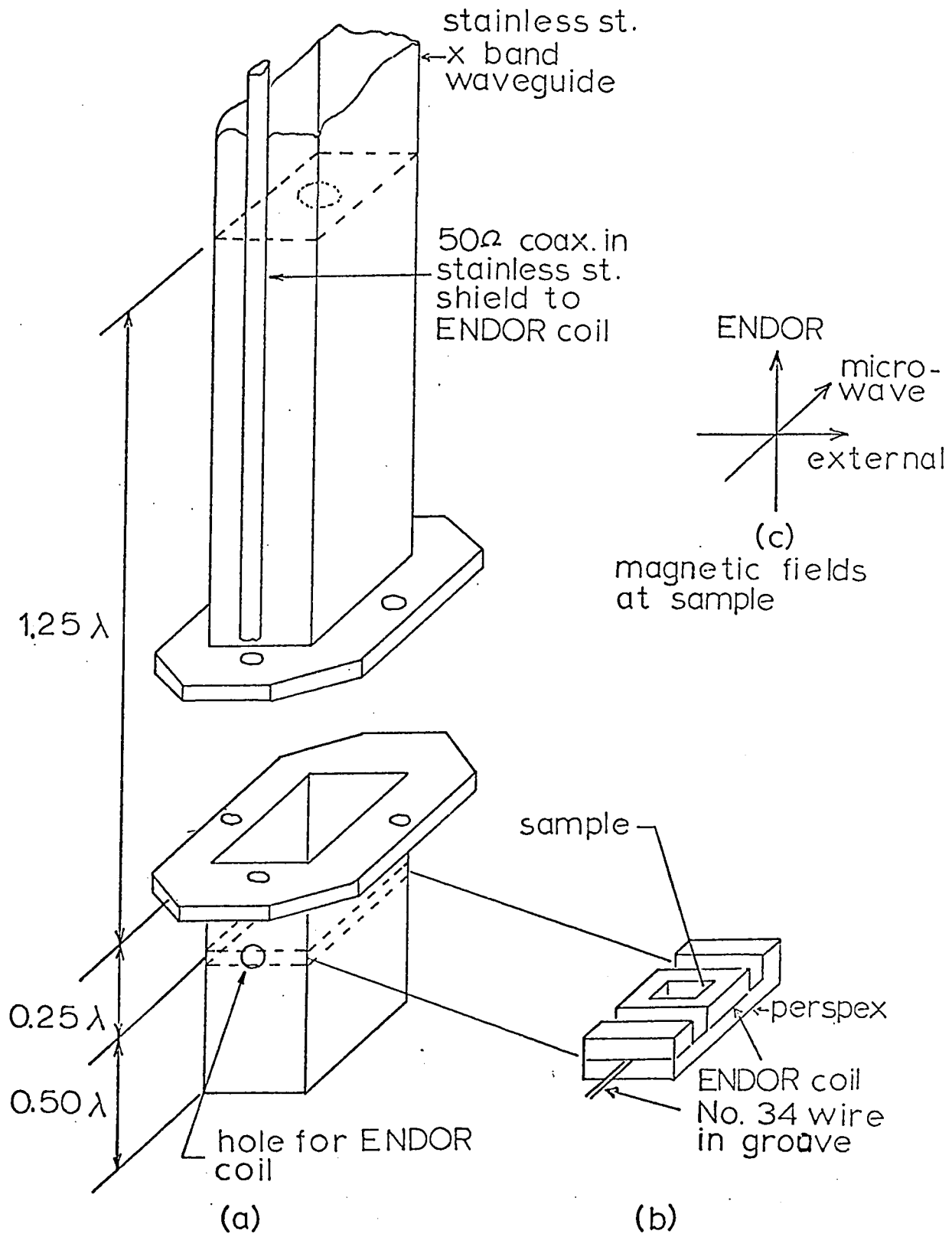
stainless st.
x band
waveguide
50Ω coax. in
stainless st.
shield to
ENDOR coil
1.25 λ
0.25 λ
0.50 λ
hole for ENDOR
coil
(a)
sample
perspex
ENDOR coil
No. 34 wire
in groove
(b)
ENDOR
micro-
wave
external
(c)
magnetic fields
at sample

CHAPTER V EXPERIMENTAL RESULTS AND CALCULATIONS

(1) ESR Results for VO^{2+}

The ESR spectrum of VO^{2+} in $AlCl_3.6H_2O$ consists of 48 identifiable ESR lines. When the magnetic field is parallel to the crystal c axis these 48 lines collapse into eight lines (see Figure 5-1). As the crystal is rotated in the direction of a tetragonal axis for one of the two types of octahedron of waters each of the eight lines will split into six resonance lines. This effect is due to the presence of six magnetic complexes in the crystal. Comparison of the ESR spectra along the z axis of each magnetic complex indicates the six complexes are identical. The stereographic projection graph, Figure 5-2, illustrates that the magnetic complexes can be grouped into two groups. The two groups correspond to the two inequivalent but otherwise similar $Al^{3+}.6H_2O$ magnetic complexes per unit cell. Within the limits of experimental accuracy, the three magnetic complexes per group have z axes which are mutually perpendicular. On the stereographic projection graph the angle between any z_1 axis with its nearest z_2 neighbour is $27^{\circ} \pm 3^{\circ}$. The projection of the tetragonal axes of the water octahedron onto the plane perpendicular to the crystal c axis shows that the two types of octahedron are rotated to each other by an angle $33^{\circ} \pm 3^{\circ}$ about the c axis. Each z axis makes an angle of $55^{\circ} \pm 2^{\circ}$ with the crystal c axis.

A graph of the angular variation of the ESR lines of VO^{2+} in $AlCl_3.6H_2O$ from the z axis of a magnetic complex to the z axis of a

Figure 5-1: VO^{2+} spectrum when the magnetic field is along the crystal c direction.

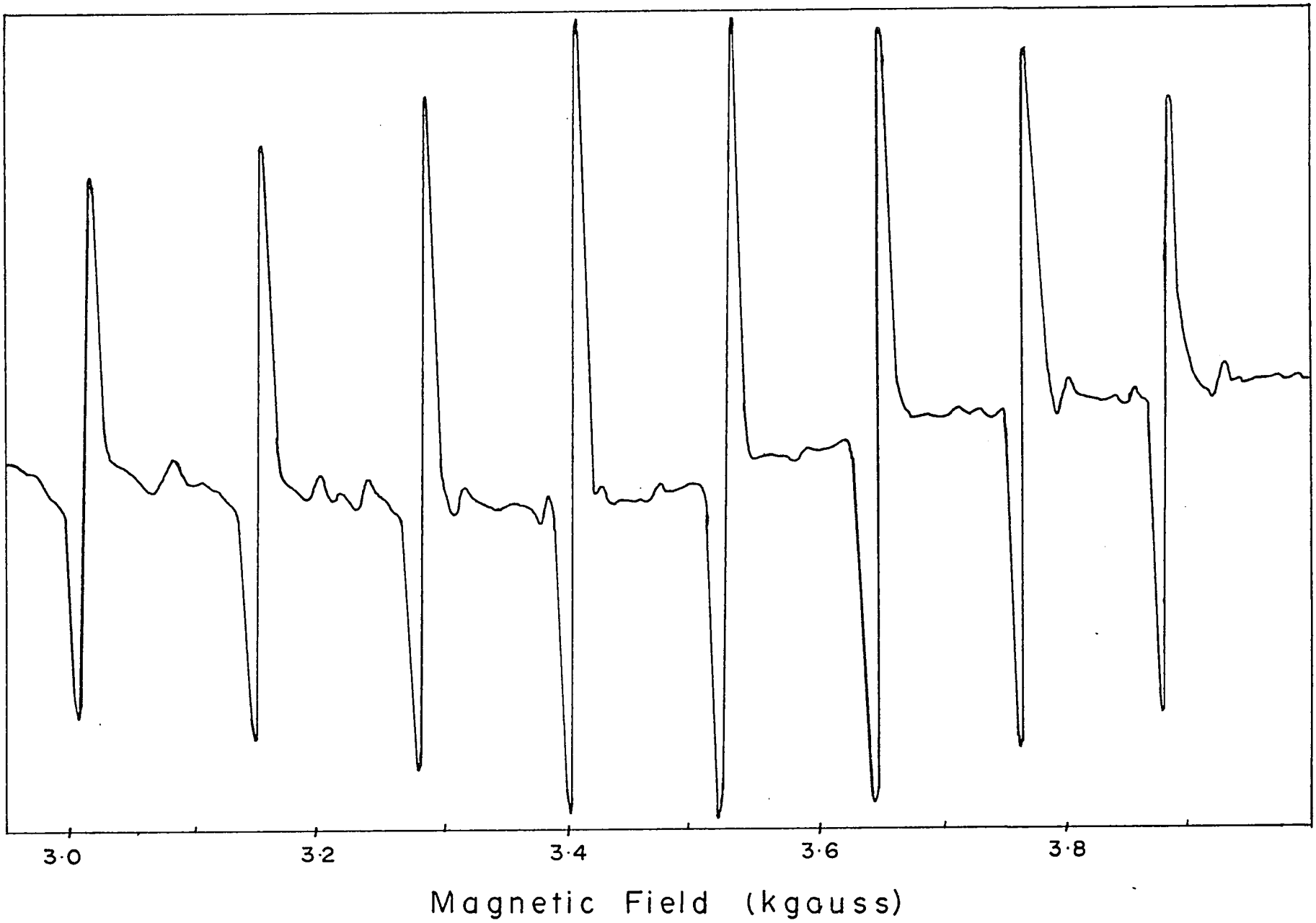
3·0
3·2
3·4
3·6
3·8
Magnetic Field (kgauss)

Figure 5-2: Stereographic projection graph showing the z directions and perpendicular planes of the $VO^{2+}.5H_2O$ magnetic complexes in $AlCl_3.6H_2O$. The subscripts 1 and 2 refer to the distinguishable types of octahedra of waters in the unit cell.

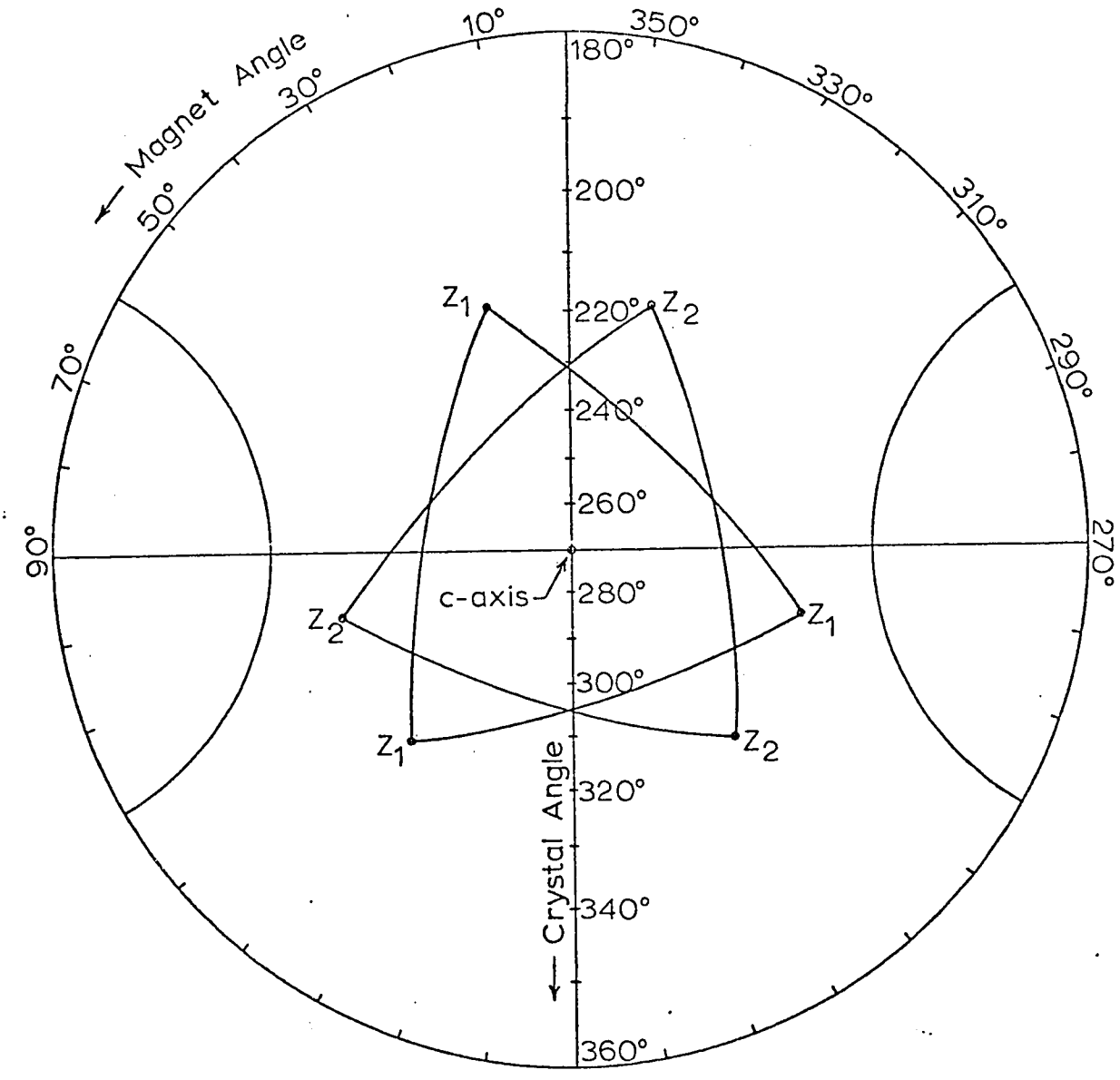
Magnet Angle
10°
350°
30°
330°
50°
310°
70°
290°
90°
270°
180°
200°
220°
240°
260°
280°
300°
320°
340°
360°
Crystal Angle
c-axis
Z_1
Z_2
Z_2
Z_1
Z_1
Z_2

second magnetic complex in the same group is shown in Figure 5-3. It can be seen from Figure 5-3 that the accuracy in finding the positions of the z axes is not great because the angular variation of the spectral lines is not sharp. In Figure 5-3 the positions of the ESR lines were obtained on chart recordings in 5^{o} intervals for the direction of the external magnetic field. The results were plotted as a function of magnetic field strength. The unbroken lines in Figure 5-3 correspond to the type 1 complexes identified in Figure 5-2, while the broken lines correspond to the type 2 complexes. The difference between the positions of one set of spectral lines, identified as belonging to one of the type 2 complexes, and a second set of spectral lines, identified as belonging to the type 1 complex which had its z axis perpendicular to the plane of rotation, is so small that the two positions cannot be resolved in Figure 5-3. These lines are the eight lines which do not show any variation in Figure 5-3. It is noted that when one group of lines shows a maximum separation, two groups of lines collapse into a single group to give a minimum separation of lines. Furthermore, in Figure 5-3 there is an angle of about 27^{o} between the maximum separation of one of the group of brokens lines and one of the group of unbroken lines.

Figure 5-4 is a typical ESR spectrum obtained along the z axis of one of the magnetic complexes. Table 5-1 lists the magnetic field positions of resonance lines along the z and perpendicular directions of a magnetic complex.

Figure 5-3: Angular variation of the ESR lines of VO^{2+} in $AlCl_3.6H_2O$ when the angle of the external magnetic field is varied in a plane perpendicular to one of the magnetic z axes. The unbroken and broken lines refer to type 1 and type 2 octahedra identified in Figure 5-2. To aid in following the pattern made by the spectrum the type 1 lines are broken into three sets; one marked with triangles, one with rectangles, and one with ellipses.

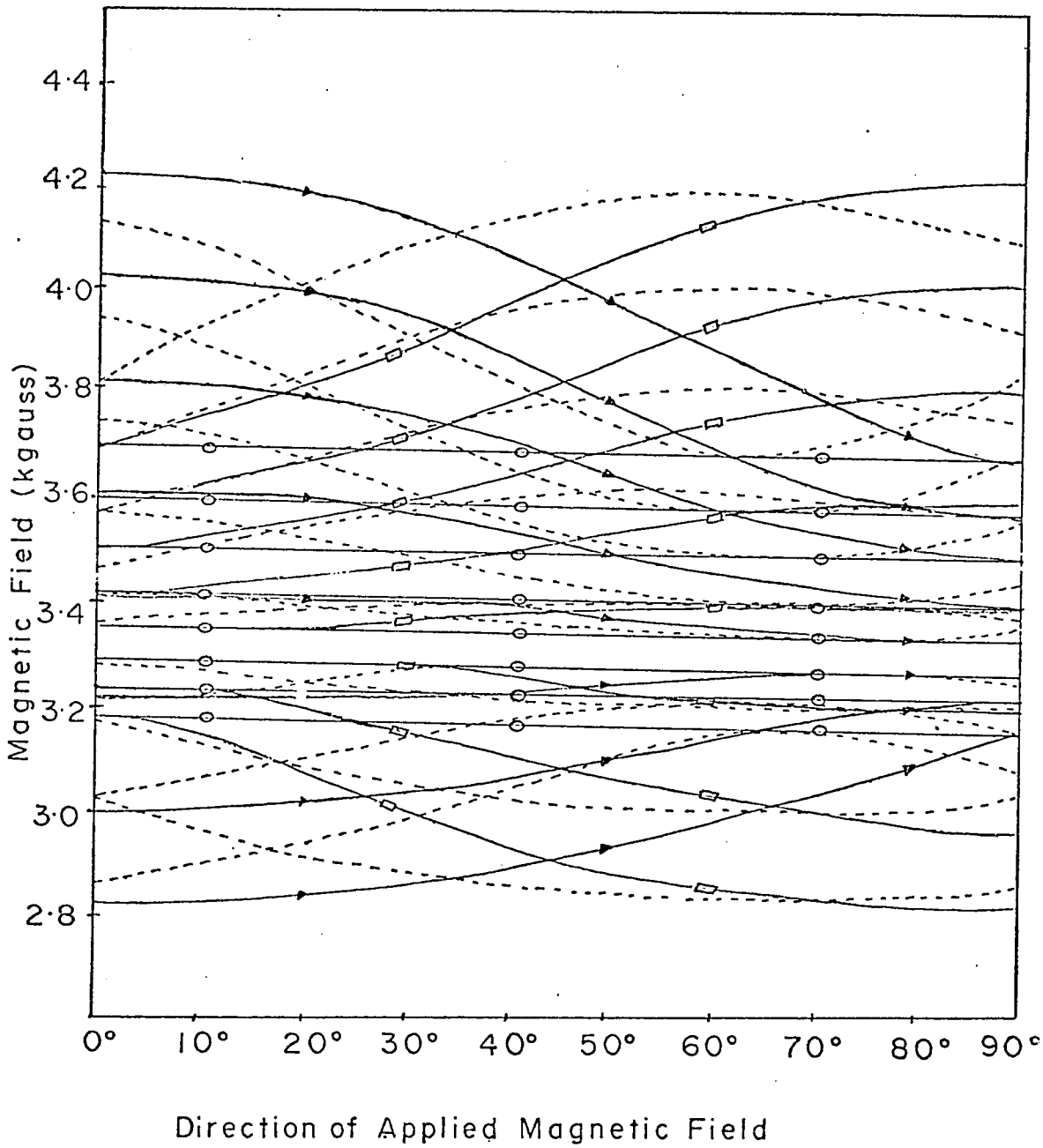
4·4
4·2
4·0
3·8
3·6
3·4
3·2
3·0
2·8
Magnetic Field (kgauss)
0°
10°
20°
30°
40°
50°
60°
70°
80°
90°
Direction of Applied Magnetic Field

Figure 5-4: ESR spectrum of VO^{2+} in $AlCl_3.6H_2O$. When the magnetic field is along the z axis of a $VO^{2+}.5H_2O$ magnetic complex.

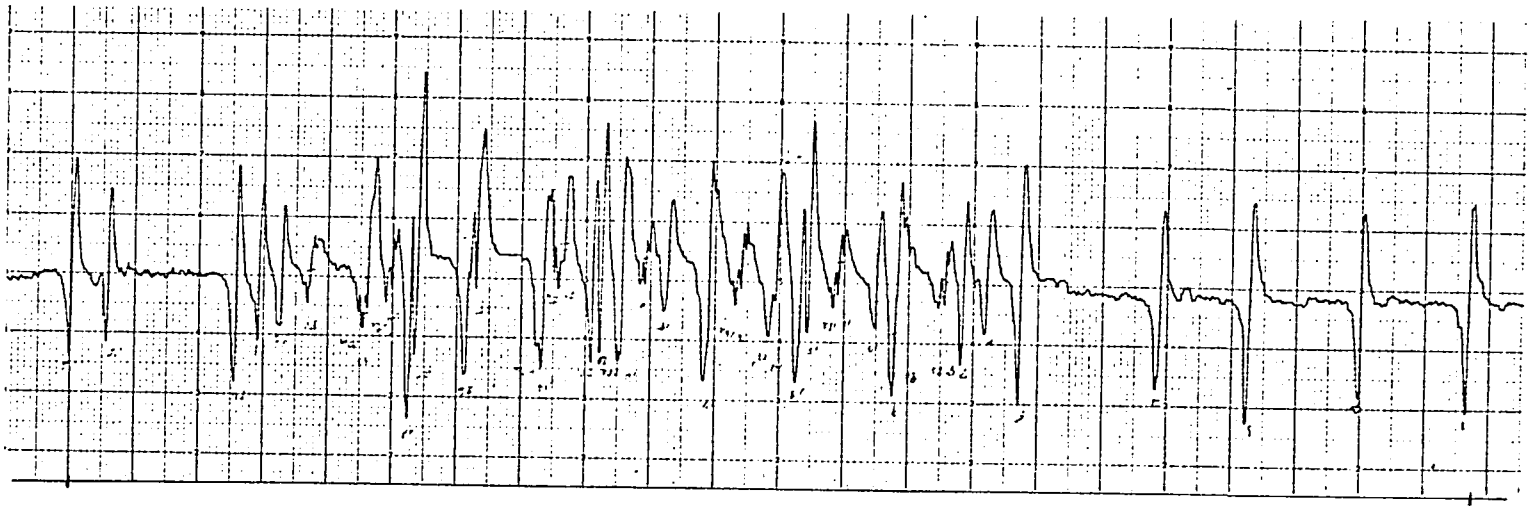
2·83
4·24
Magnetic Field (kgauss) ⟶

Table 5-1: Magnetic field positions of the VO^{2+} resonance

M_I	Magnetic Field values for z axis (kgauss)	Magnetic Field values for the perpendicular Direction (kgauss)
±7/2	4.2376	3.7113
±5/2	4.0321	3.6171
±3/2	3.8280	3.5281
±1/2	3.6260	3.4456
∓1/2	3.4266	3.3690
∓3/2	3.2272	3.2986
∓5/2	3.0289	3.2356
∓7/2	2.8342	3.1830

Microwave frequency = 9.533 GHz

In Table 5-1 the M_I values are listed as being plus or minus because the sign of M_I could not be determined from the experimental data.

The VO^{2+} spin Hamiltonian parameters are listed in Table 5-2. They were calculated using equations 3.22 and 3.23. There were five contributing factors to the uncertainty of the values of the parameters.

The microwave frequency could be determined to an accuracy of ±2kHZ. The measurement of the magnetic field at the site of the NMR probe had an uncertainty of ±1 gauss. The difference in the magnetic field strength at the site of the NMR probe and the magnetic field strength at the sample's location contributed to the total error. There was also error due to the misalignment of the magnetic field with the crystal magnetic axes, and in finding the centre of each spectral line.

Table 5-2: Spin Hamiltonian parameters of VO^{2+} doped in $AlCl_3.6H_2O$

Spin Parameters	Value
$g_{//}$	1.929 ± 0.002
$g_{\perp}$	1.974 ± 0.002
$\|A\|$	$187 \times 10^{-4} cm^{-1} \pm 1 \times 10^{-4} cm^{-1}$
$\|B\|$	$72 \times 10^{-4} cm^{-1} \pm 1 \times 10^{-4} cm^{-1}$

(2) ESR Results for Cr^{3+}

ESR measurements were made on $AlCl_3.6H_2O$ doped with chromium in its natural abundance at room temperature ($297^{o}K$), the sublimation temperature of dry ice ($195^{o}K$), liquid nitrogen temperature ($77^{o}K$), and liquid helium temperature ($4.2^{o}K$). From Table 5-3, which lists the g and D values found at the various temperatures where measurements were made. It can be seen that the magnitude of D increases slightly as the temperature decreases. ESR measurements of samples doped with $^{53}Cr^{2+}$ enriched to 96% at $297^{o}K$ and $4.2^{o}K$ showed the g and D values to be the same as in samples which were doped with chromium in its natural isotopic abundance. In the $^{53}Cr^{3+}$ enriched sample each spectral line splits into four lines (see Figure 5-5) due to hyperfine interactions. The sign of D was determined from the comparative magnitudes of the first and last resonance lines at room and liquid helium temperature. Figure 5-6 shows the three different ways the ground state of Cr^{3+} can split, depending on whether D is positive, negative, or zero. Since the intensity of the low field ESR lines was found to be greater than the high field ESR lines at both room and liquid helium temperature, D is negative.

Figure 5-7 shows a graph of the angular variation of the ESR lines of Cr^{3+} in $AlCl_3.6H_2O$ from the crystal c axis to a plane perpendicular to the crystal c axis. In Figure 5-7 the magnetic field strength of each ESR line was measured in 5^{o} intervals for the direction of the external magnetic field. The maximum separation of the ESR lines

Figure 5-5: ESR spectrum of $^{53}Cr^{3+}$ in $AlCl_3.6H_2O$ at room temperature when the magnetic field is (a) along the z axis and (b) along a perpendicular direction.

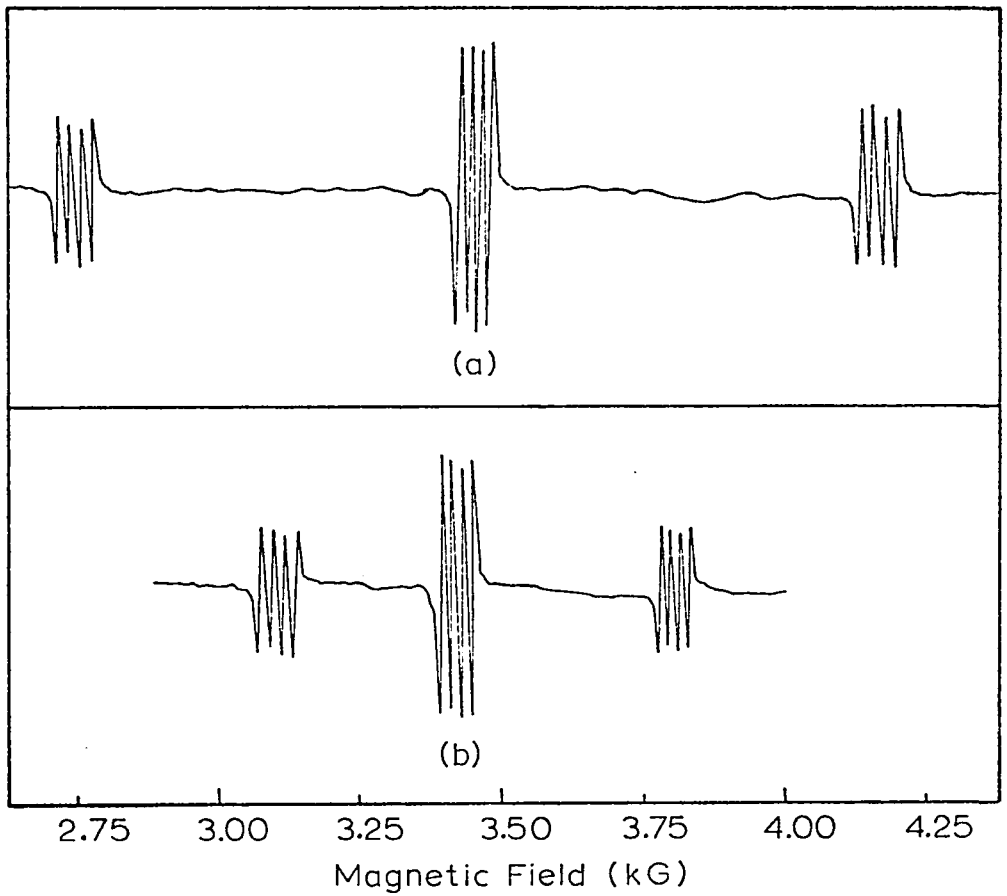
(a)
(b)
2.75
3.00
3.25
3.50
3.75
4.00
4.25
Magnetic Field (kG)

Figure 5-6: Energy versus magnetic field plots showing the fine structure splitting of Cr^{3+} for D positive, negative and zero.

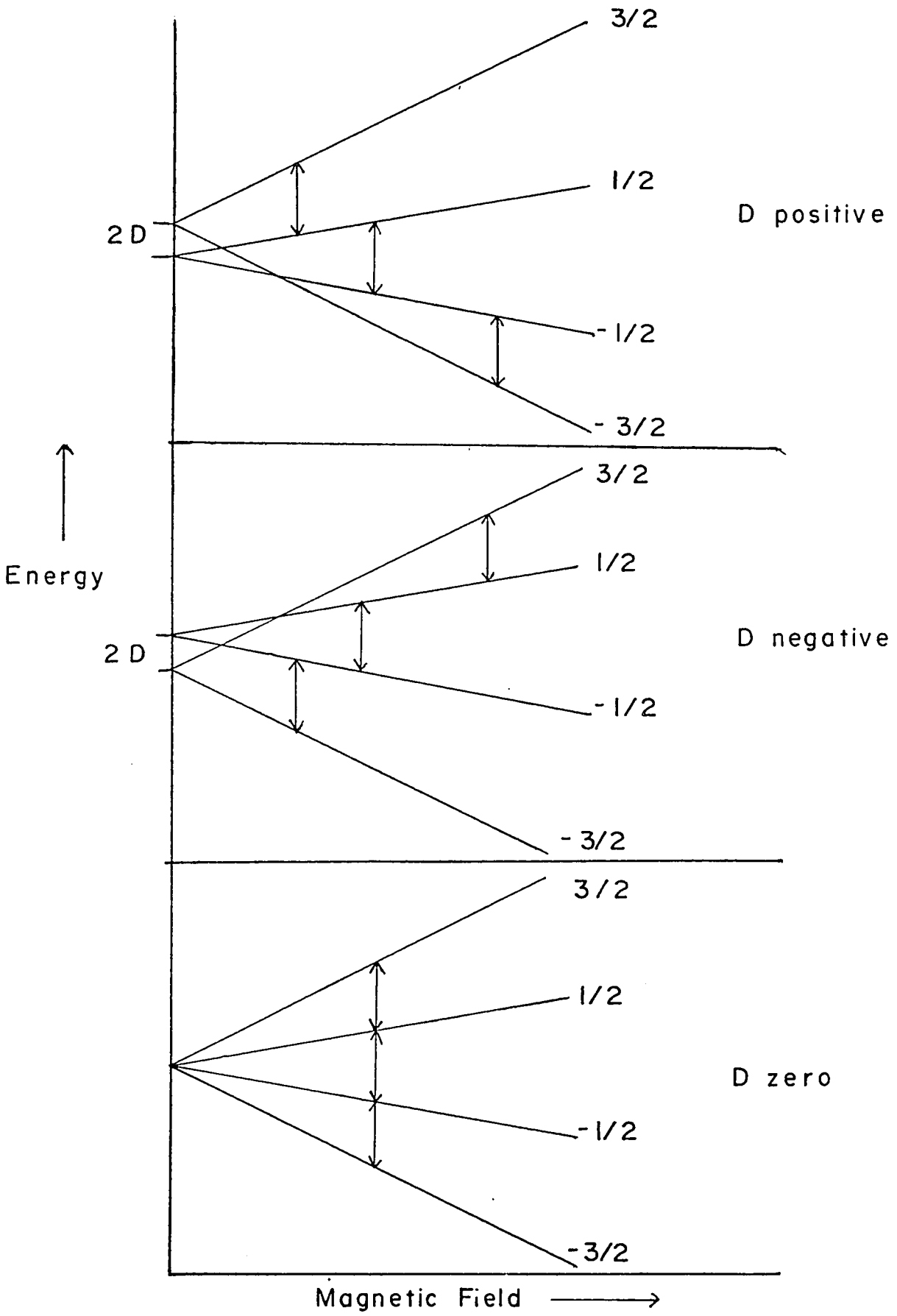
3/2
1/2
2D
D positive
-1/2
-3/2
Energy
3/2
1/2
2D
D negative
-1/2
-3/2
3/2
1/2
D zero
-1/2
-3/2
Magnetic Field

occurs when the external magnetic field is along the crystal c axis. This result means the $Cr^{3+}.6H_2O$ magnetic complexes are trigonally distorted along the crystal c axis. When the magnetic field is rotated in the plane perpendicular to the crystal c axis the ESR lines do not show any variation in their position. Hence the magnetic complexes possess axial symmetry. Figure 5-7 agrees with the plot previously obtained by Emch and Lacroix[42] showing the angular variation of the ESR lines of Cr^{3+} in $AlCl_3.6H_2O$.

(3) ENDOR Results for $^{53}Cr^{3+}$

ENDOR measurements were made in 70-80 MHz range at several positions on the low and high field ESR lines in the z and perpendicular directions. Chart recordings of the ENDOR spectra obtained at the various positions are shown in Figures 5-8a, 5-8b, 5-9a and 5-9b.

The procedure for calculating the spin Hamiltonian parameters is as follows. The $g_{//}$, $g_{\perp}$, and D values are first calculated from the ESR measurements using equations 3-25a thru 3-25d, and 3-27(a-c). Approximate values for the hyperfine parameters are derived with the aid of four of the equations tabulated in Table 3-1, which are pertinent to the ENDOR transitions measured. These values are used as the starting parameters in a computer program which diagonalizes the spin Hamiltonian and then calculates the ENDOR transition frequencies

Figure 5-7: Angular variation of the ESR lines of Cr^{3+} in $AlCl_3.6H_2O$ at room temperature.

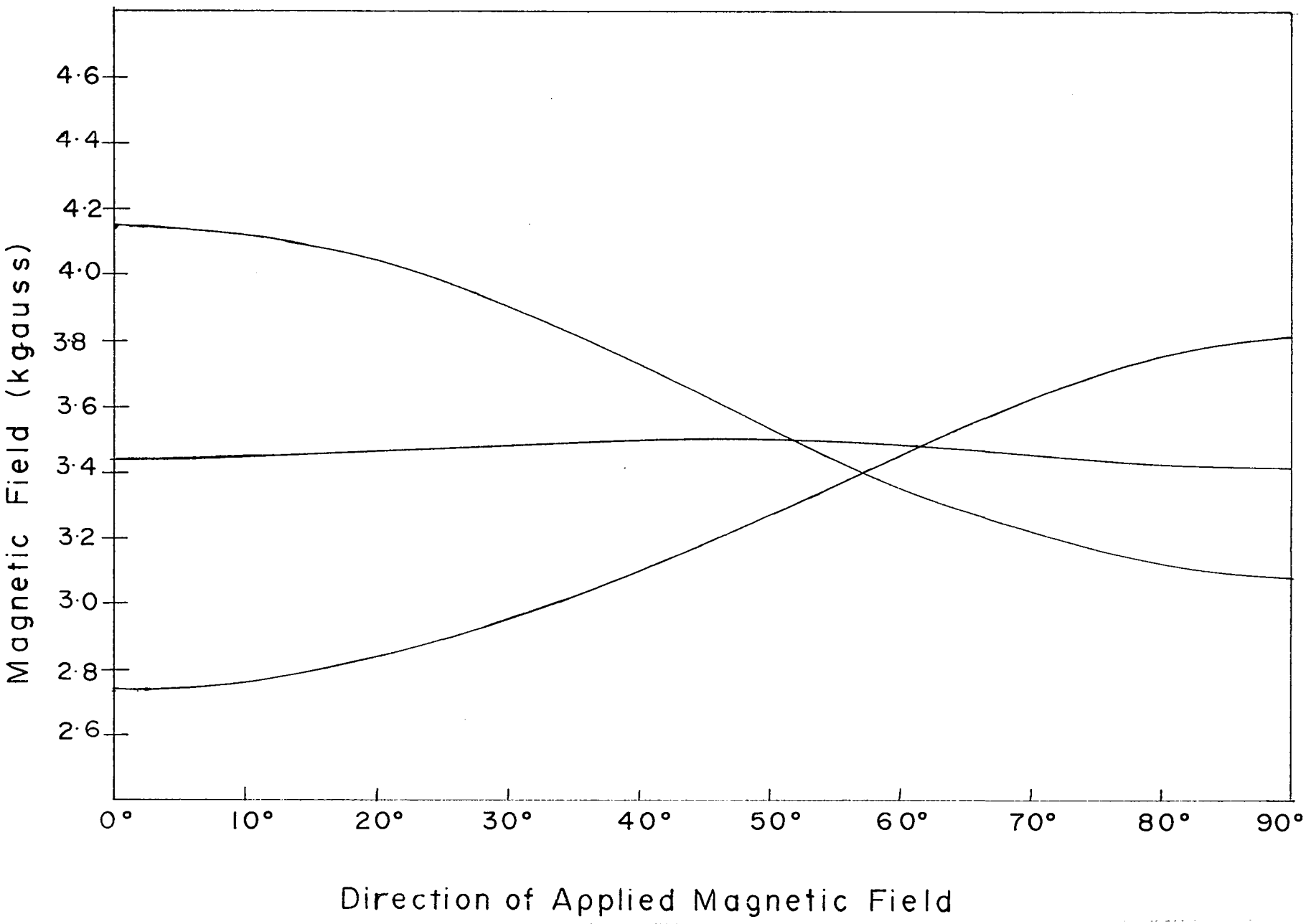
4·6
4·4
4·2
4·0
3·8
3·6
3·4
3·2
3·0
2·8
2·6
Magnetic Field (kgauss)
0°
10°
20°
30°
40°
50°
60°
70°
80°
90°
Direction of Applied Magnetic Field

Table 5-3: Spin parameters g and D for Cr^{3+} in $AlCl_3.6H_2O$ at room temperature, dry ice temperature, liquid nitrogen temperature and liquid helium temperature.

Temperature	D $(10^{-4}cm^{-1})$	g
298^oK	-326 ± 2	1.975 ± 0.002
195^oK	-337 ± 2	1.975 ± 0.002
77^oK	-338 ± 2	1.975 ± 0.002
4.2^oK	-341 ± 2	1.975 ± 0.002

Table 5-4: ESR transition field values for Cr^{3+} in $AlCl_3.6H_2O$ at room temperature, dry ice temperature, liquid nitrogen temperature, and liquid helium temperature.

Temperature	Transition $M_S \rightarrow M_S+1$	Magnetic Field Value for H // z (kgauss)	Magnetic Field Value for H ⊥ z (kgauss)	Microwave Frequency H // z (kMhz)	Microwave Frequency H ⊥ z
298^oK	-3/2 → -1/2	2.7450	3.7972	9.533	9.531
	-1/2 → 1/2	3.4523	3.4195		
	1/2 → 3/2	4.1592	3.0962		
195^oK	-3/2 → -1/2	2.7131		9.521	
	-1/1 → 1/2	3.4471			
	1/2 → 3/2	4.1758			
77^oK	-3/2 → -1/2	2.5537		9.075	
	-1/2 → 1/2	3.2914			
	1/2 → 3/2	4.0221			
4.2^oK	-3/2 → -1/2	2.6347	3.7494	9.315	9.308
	-1/2 → 1/2	3.3733			
	1/2 → 3/2	4.1023	3.0134		

Figure 5-8: ENDOR chart recordings of

(a) the low field group $M_S(-3/2 \rightarrow -1/2)$ and

(b) the high field group $M_S(1/2 \rightarrow 3/2)$

of $^{53}Cr^{3+}$ in $AlCl_3.6H_2O$ when the external magnetic field is along the crystal c axis.

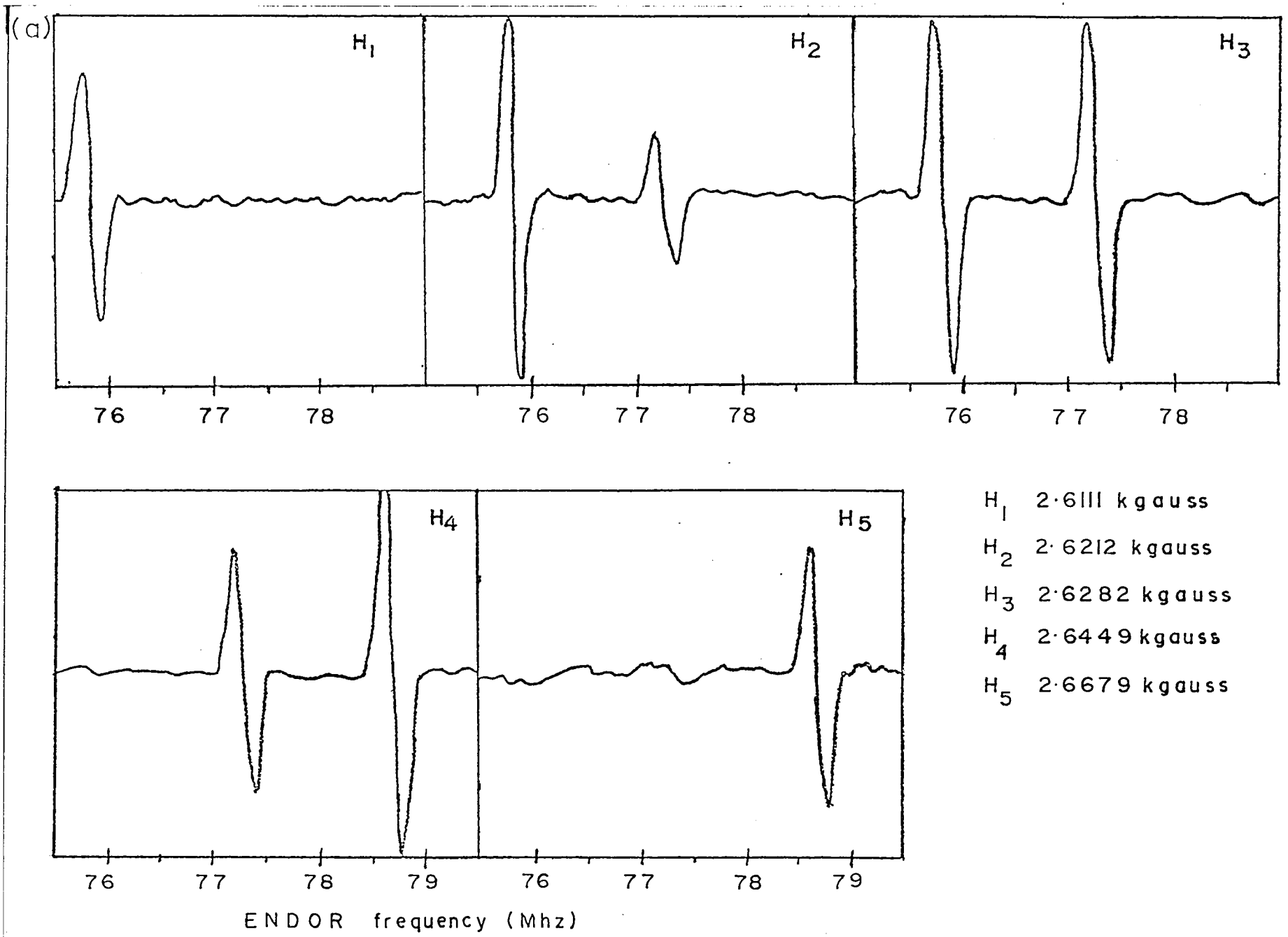

H_1 2·6111 kgauss

H_2 2·6212 kgauss

H_3 2·6282 kgauss

H_4 2·6449 kgauss

H_5 2·6679 kgauss

(b)

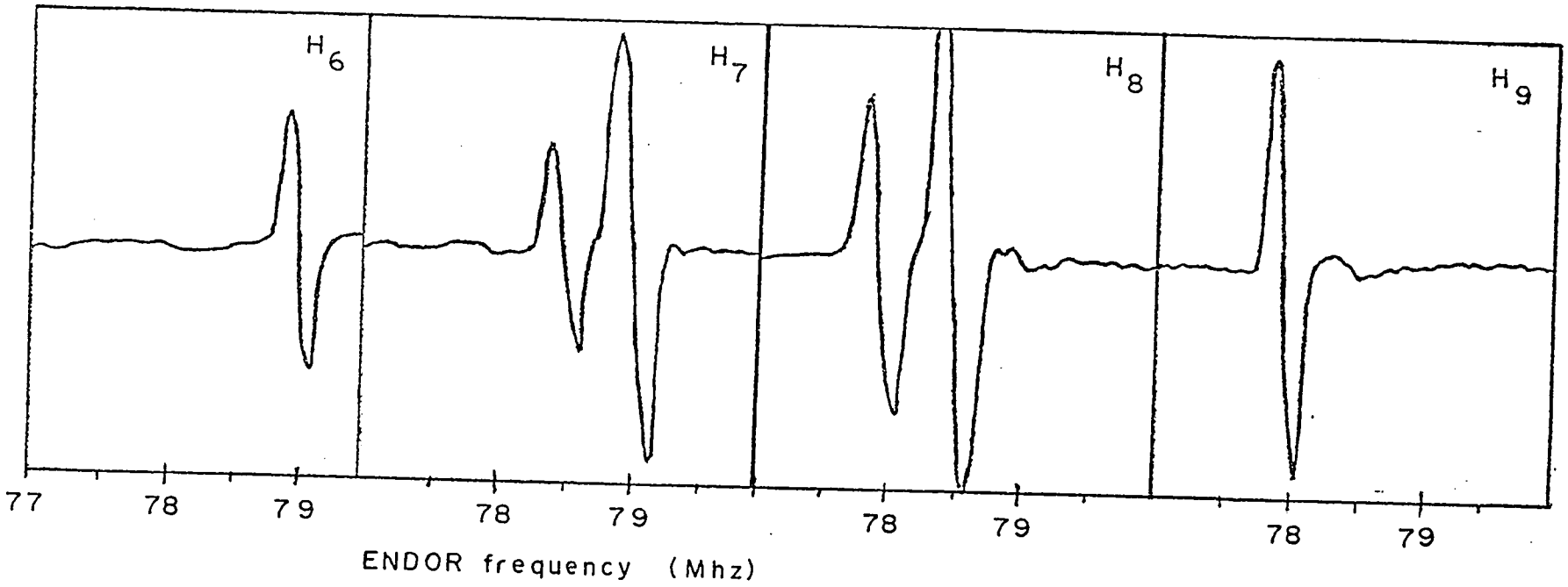

H_6 4·0719 kgauss

H_7 4·0918 kgauss

H_8 4·1150 kgauss

H_9 4·1307 kgauss

Figure 5-9: ENDOR chart recordings of

(a) the low field group $M_S(1/2 \rightarrow 3/2)$ and

(b) the high field group $M_S(-3/2 \rightarrow -1/2)$

of $^{53}Cr^{3+}$ in $AlCl_3.6H_2O$ when the external magnetic field is perpendicular to the crystal c axis.

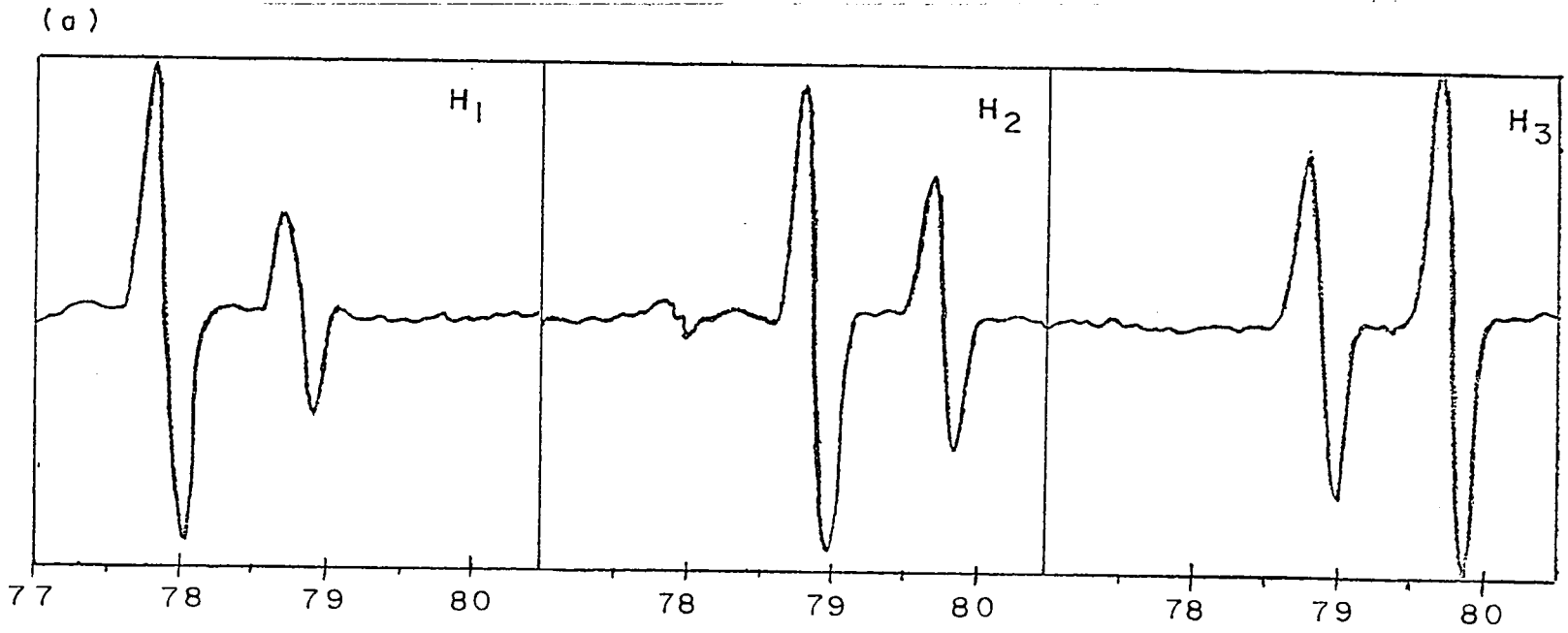

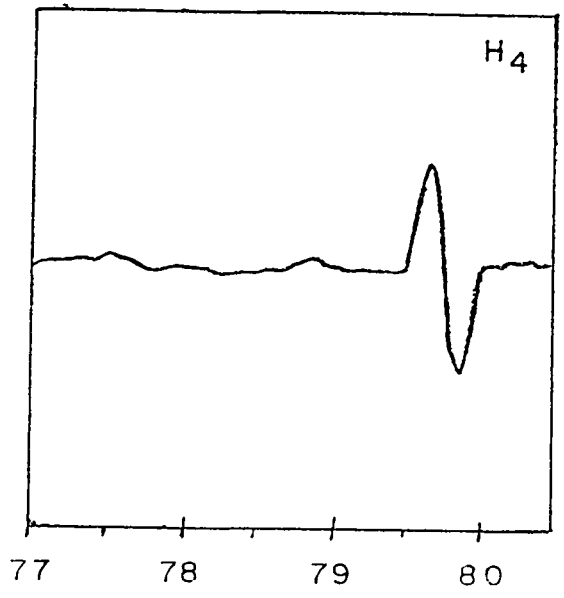

H_1 2·9789 kgauss

H_2 3·0033 kgauss

H_3 3·0282 kgauss

H_4 3·0433 kgauss

between the adjacent energy levels. The computer program is given in Appendix A. The parameters are varied one at a time and the measured ENDOR transition frequencies are compared with the calculated transition frequencies. The spin parameters which result in the smallest difference between the measured and calculated transition frequencies are called the best fit values. For $^{53}Cr^{3+}$ doped in $AlCl_3.6H_2O$ the best fit values obtained give an average difference of 7.4 kHz between the calculated and measured transition frequencies. This difference corresponds to A, B, and Q' having uncertainties less than $\pm$ 0.001 x $10^{-4}cm^{-1}$ and g_n having an uncertainty less than $\pm$ 0.001. Table 5-5 lists the calculated spin Hamiltonian parameters. Tables 5-6 and 5-7 show how the measured and calculated ENDOR transition frequencies compare.

Table 5-5: Spin Hamiltonian parameters for $^{53}Cr^{3+}$ in $AlCl_3.6H_2O$ at 4.2°K

D	-341 x $10^{-4}cm^{-1}$
g	1.975
g_n	-0.320
A	17.277 x $10^{-4}cm^{-1}$
B	17.474 x $10^{-4}cm^{-1}$
Q'	0.159 x $10^{-4}cm^{-1}$

Table 5-6: ENDOR frequencies (MHz) when the external magnetic field is along the z direction.

FIELD (kG)	Calculated	Measured	Difference
(low group)			
2.6111	75.853	75.832	0.021
2.6212	75.850	75.850	0.000
	77.277	77.277	0.000
2.6282	75.853	75.834	0.019
	77.271	77.275	0.004
2.6449	77.266	77.276	0.010
	78.690	78.691	0.001
2.6679	78.679	78.705	0.026
(high group)			
4.0719	78.995	78.987	0.008
4.0918	78.463	78.466	0.003
	79.001	79.000	0.001
4.1150	77.933	77.937	0.004
	78.474	78.468	0.006
4.1307	77.939	77.939	0.000
		average difference	7.4 khz

Table 5-7: ENDOR frequencies (MHz) when the external magnetic field is along a perpendicular direction

FIELD (kG)	Calculated	Measured	Difference
(low group)			
2.9789	77.896	77.913	0.017
	78.819	78.825	0.006
3.0033	78.838	78.845	0.007
	79.747	79.749	0.002
3.0282	78.840	78.842	0.002
	79.758	79.752	0.006
3.0433	79.764	79.750	0.014
(high group)			
3.7131	xxx	77.730	
3.7420	77.668	77.663	0.005
3.7620	xxx	77.656	
		average difference	7.4 khz

xxx Not possible to reliably determine which transition or how much of which combination of transitions is being measured due to the overlap of the spectral lines.

CHAPTER VI DISCUSSION AND CONCLUSIONS

(1a) VO^{2+}: Summary of the Spectrum

Aluminum chloride hexahydrate is composed of parallel chains of the type $-Al(H_2O)_6^{3+}- 3Cl^- -Al(H_2O)_6^{3+} - 3Cl^-$ - running parallel to the crystal c axis. From X-ray measurements, alternate water octahedra are rotated with respect to each other about their [111] axes. The angle which the octahedra make with respect to each other has been quoted by Andress and Carpenter to be about 24^{o} [6], and by Buchanan and Harris to be about 28^{o} [4]. Neither Andress and Carpenter, nor Buchanan and Harris give an estimate of the uncertainty of their values. When the VO^{2+} ion substitutes for the Al^{3+} ion in the crystal the distorted octahedral complex $VO^{2+}.5H_2O$ is formed. In this complex, the V-O bond direction is along the direction of the missing water.

The ESR results show that the two different types of octahedra are rotated $33^{o} \pm 3^{o}$ about their [111] direction with respect to each other. This measurement can be interpreted in two different ways. Since neither Andress and Carpenter, nor Buchanan and Harris quote an error, then the angle found from the ESR work might be in agreement with the angle found from the X-ray work. The second possibility is that when the VO^{2+} ion replaces Al^{3+} the hydrated complex is rotated about the [111] axis. The change in the relative orientations of the different sets of octahedra is due to the two different sets of octahedra being rotated differently when the VO^{2+} ion replaces the Al^{3+} ion. It has

been found that when VO^{2+} is doped in RbAl alum[33], CsAl alum[33], KAl alum[34], and NH_4Al alum[34] the VO^{2+} ion rotates the water ocahedron 8^{o} - 9^{o} from its original position about the [111] axis.

In the orientated octahedron the tetragonal distortion is along one of the three axes. Since the octahedra have two distinct orientations, there are up to six distinct possible angles between the V-O bonds and the direction of an applied magnetic field. The ground state of VO^{2+} has a spin of ½. The single spin transition appears as eight lines because of hyperfine interactions with the vanadium nucleus (^{51}V I = 7/2, 99.75%). The six possible orientations of the tetragonal distortion multiplies the eight lines to give 48 observable lines.

(1b) VO^{2+}: Spin Parameters A and B

Table 6-1 lists the spin parameters of VO^{2+} doped in several crystals. Except for GeO_2, germanium dioxide, the VO^{2+} ion enters the host crystal replacing a metal (+++) ion centered in an octahedron of waters. In GeO_2, unlike the alums, there is no charge compensation necessary when the VO^{2+} ion enters the lattice. A comparison of the spin Hamiltonian parameters for GeO_2 with those of the other crystals shows that the parameters are insensitive to the effects of charge compensation.

Table 6-1: Spin Hamiltonian parameters for VO^{2+} doped in different crystals

Host	$g_{//}$	$g_{\perp}$	$\|A\|$ ($\times 10^{-4} cm^{-1}$)	$\|B\|$ ($\times 10^{-4} cm^{-1}$)
$AlCl_3.6H_2O$	1.929	1.974	187	72
$RbAl(SO_4)_2.12H_2O$ [33]	1.932	1.977	182	67
$CsAl(SO_4)_2.12H_2O$ [33]	1.932	1.977	183	66
$KAl(SO_4)_2.12H_2O$ [34]	1.940	1.978	177	68
$NH_4Al(SO_4)_2.12H_2O$ [34]	1.939	1.976	176	66
GeO_2 [35]	1.929	1.976	176	68

(1c) VO^{2+} Comparison of the Crystal Field Description with the Molecular Orbital Description of $VO^{2+}.5H_2O$

In the crystal field approach the V^{4+} ion is in an octahedral crystal field with an additional small tetragonal distortion. The diagonalized Hamiltonian which describes the system is

	d_{xy}	d_{yz}	d_{zx}	$d_{x^2-y^2}$	d_{z^2}
d_{xy}	$-2\Delta/5 - 2\delta/3$	0	0	0	0
d_{yz}	0	$-2\Delta/5 + \delta/3$	0	0	0
d_{zx}	0	0	$-2\Delta/5 + \delta/3$	0	0
$d_{x^2-y^2}$	0	0	0	$3\Delta/5 - 2\delta/3$	0
d_{z^2}	0	0	0	0	$3\Delta/5 + 2\delta/3$

where Δ is the separation energy between the triplet and doublet states in the pure octahedral crystal field (see Figure 3-2). δ is the separation energy between the ground singlet state and first excited state in the tetragonally distorted crystal field (see Figure 3-2).

Using equation 3-9 the following expressions for $g_{\perp}$ and $g_{//}$ are obtained

$$g_{\perp} = 2.0023\ (1 - \lambda/\delta) \qquad 6\text{-}1$$

$$g_{//} = 2.0023\ (1 - 4\lambda/\Delta) \qquad 6\text{-}2$$

It is interesting that if $\delta = \Delta/4$ the g value will be isotropic even though the ion is not in a cubic environment. For $\delta > \Delta/4$ it follows that $g_{\perp} > g_{//}$, which is consistent with the experimental results for $VO^{2+}.5H_2O$ (see Table 6-1). This means the $VO^{2+}.5H_2O$ complex has a large tetragonal distortion. According to the analysis of Ballhausen and Gray[19] a pure crystal field model of the

$VO^{2+}.5H_2O$ complex does not explain why such a large tetragonal distortion exists. To accurately describe the $VO^{2+}.5H_2O$ complex the covalent nature of the V-O bond must be considered. Ballhausen and Gray used a semiempirical linear combination of atomic orbitals - molecular orbital (LCAO-MO) model. The molecular orbitals of the $VO^{2+}.5H_2O$ complex were constructed by adding wave functions of the neighbouring ligands to the 3d, 4s, and 4p wave functions of the V^{4+} ion. The resultant stable molecular orbitals obtained reflect the lower energy of the molecular orbitals as compared to the atomic orbitals, and the tetragonal symmetry of the $VO^{2+}.5H_2O$ complex. In the Ballhausen and Gray picture the electronic ground state for the $VO^{2+}.5H_2O$ complex is the $3d_{xy}$ orbital of the V^{4+} ion, which is not bound to any of the ligand orbitals.

The theoretical expressions obtained by Ballhausen and Gray for the g values are[19]

$$g_{\perp} = 2.0023 \quad (1 - \gamma^2\lambda/\Delta_1) \qquad 6\text{-}3$$

$$g_{//} = 2.0023 \quad (1 - 4\beta^2\lambda/\Delta_2) \qquad 6\text{-}4$$

where Δ_1 is the energy difference between the ground state and first excited state; Δ_2 is the energy difference between the ground state and second excited state; γ is a measure of how much of the first excited molecular orbital is due to the $3d_{xz}$ and $3d_{yz}$ atomic orbitals of V^{4+}; β is a measure of how much of the second excited molecular orbital is due to the $3d_{x^2-y^2}$ atomic orbital of V^{4+}.

The values for γ, β, Δ_1, and Δ_2 are[19]

$\gamma = 0.907$

$\beta = 0.946$

$\Delta_1 = 13{,}000\ cm^{-1}$

$\Delta_2 = 16{,}000\ cm^{-1}$

Ballhausen and Gray estimated λ, the spin-orbit coupling parameter for V^{4+}, to be 135 cm^{-1} or 54% of its free ion value 248 cm^{-1}. The values of $g_\perp$ and $g_{//}$ calculated from equations 6-3 and 6-4 are

$g_\perp = 1.983$

$g_{//} = 1.940$

If the pure crystal field model is used to calculate $g_\perp$ and $g_{//}$ then for $\lambda = 146\ cm^{-1}$

$g_\perp = 1.980$

$g_{//} = 1.929$

The experimentally measured g values for VO^{2+} doped in $AlCl_3.6H_2O$ are

$g_\perp = 1.974 \pm 0.002$

$g_{//} = 1.929 \pm 0.002$

In conclusion, the Ballhausen and Gray model takes into account the covalent nature of the V-O bond. However, the pure crystal field model does not assume as large a reduction in the spin-orbit coupling parameter of the V^{4+} ion. Both models predict that for the $VO^{2+}.5H_2O$ complex $g_\perp$ is greater than $g_{//}$. The pure crystal field

values for $g_{\perp}$ and $g_{//}$ are in better agreement with the experimental values found for VO^{2+} doped in $AlCl_3.6H_2O$ than the Ballhausen and Gray values for $g_{\perp}$ and $g_{//}$.

(2a) Cr^{3+}: Summary of ESR Spectrum

The ESR spectrum of $AlCl_3.6H_2O$ doped with Cr^{3+} consists of three spectral lines. The z axis of the magnetic complex is along the crystal c axis. Comparison of the Al-H_2O bond length (1.87Å) with the Cr-H_2O bond length (1.90Å) suggests that when Cr^{3+} substitutes for Al^{3+} the octahedron of waters will expand. McGarvey[21] has shown that for A < B, which is true for Cr^{3+} doped in $AlCl_3.6H_2O$, the octahedron is trigonally compressed. A possible explanation for the observed trigonal compression along the crystal c axis is that the octahedron does expand when Cr^{3+} replaces Al^{3+}. However, the forces bonding the atoms in the $-Al^{3+}.6H_2O - 3Cl^- - Al^{3+}.6H_2O - 3Cl^-$ - chains, which run parallel to the crystal c axis, are stronger than the forces binding the parallel chains together. Hence, when the octahedron expands the observed effect is a trigonal compression along the crystal c direction.

(2b) Cr^{3+}: Comparison of $g_{//}$, $g_{\perp}$ and D values for $AlCl_3.6H_2O$ found by Different Authors

The spin Hamiltonian parameters $g_{//}$, $g_{\perp}$, and D of Cr^{3+} doped in $AlCl_3.6H_2O$ have been previously measured by several authors. Table 6-2 lists the results of measurements made on $AlCl_3.6H_2O$ and $AlCl_3.6D_2O$. With the exception of the D value reported by Wong at $77^{o}K$, the values of g and D obtained in the present study agree with those of previous authors. It is noted that the D values for $AlCl_3.6D_2O$ at $297^{o}K$ and $77^{o}K$ are shifted by a constant amount from the values obtained in the present study. This shifting of the D value by a constant amount is consistent with the work done by Danilov and Manoogian on nondeuterated and and deuterated crystals of RbGa alum and CsGa alum doped with trivalent chromium[28a].

(2c) Cr^{3+}: Analysis of Electronic g-value

The g value for Cr^{3+} doped in $AlCl_3.6H_2O$ is, within experimental error, isotropic. In an octahedral field

$$g = 2.0023\ (1 - \lambda\Omega_{zz}) \qquad 3\text{-}9$$

Ω_{zz} is given by

$$\Omega_{zz} = \sum_{n\neq 0} \frac{\langle 0|L_z|n\rangle\langle n|L_z|0\rangle}{E_n - E_o} = 4/\Delta$$

where Δ is the energy difference between the ground state and first excited state.

From optical measurements on $Cr^{3+}.6H_2O$ it has been found that[36]

$$\Delta = 17.500 \times 10^3 cm^{-1}.$$

Using equation 3-9, the spin-orbit coupling parameter λ is $60 \pm 5\ cm^{-1}$. This value for the spin-orbit coupling parameter is 66% of the free ion value found for Cr^{3+}. The value of the spin-orbit coupling parameter for Cr^{3+} in chromium alum is $57\ cm^{-1}$. [37]

In a survey of experimental results from paramagnetic resonance and optical spectra Owen[38] found the spin-orbit coupling parameter of a paramagnetic ion in a crystal to be reduced 20% to 30% of its free ion value. His interpretation of these results was that the paramagnetic ion's electrons are spending 20% to 30% of their time in the orbits of the surrounding ligands. This implies that there is very strong covalent bonding between the paramagnetic ion and its surrounding ligands. Marshall and Stuart[39] have objected to Owen's interpretation. They have proposed that the reduction in the spin-orbit parameter in transition ion complexes is due to the screening effect of the ligands' electrons. When the ligands' electrons screen the paramagnetic ion's 3d electrons from the paramagnetic ion's nucleus the electron cloud expands. The reduction in the spin-orbit parameter follows from λ being proportional to the average value of $1/r^3$ for the 3d wave function. Abragam and Bleaney have suggested that some of the reduction of the spin-orbit parameter may be due to vibrations in the crystal field[40].

Table 6-2: Values of $g_{//}$, $g_{\perp}$, and D of Cr^{3+} doped in $AlCl_3.6H_2O$ and $AlCl_3.6D_2O$ found by different authors at different temperatures.

Author (Crystal)	Parameter	Temperature	Value*
Emch and Lacroix [1] ($AlCl_3.6H_2O$)	$g_{//}$	297°K	1.9769 ± 0.0004
	$g_{\perp}$	297°K	1.9764 ± 0.0004
	|D|	297°K	327 ± 1
Wong [2] ($AlCl_3.6H_2O$)	g	297°K	1.977 ± 0.001
	g	77°K	1.977 ± 0.001
	|D|	297°K	327 ± 1
	|D|	77°K	430 ± 1
Wong [2] ($AlCl_3.6D_2O$)	g	297°K	1.977 ± 0.001
	g	77°K	1.977 ± 0.001
	|D|	297°K	315 ± 1
	|D|	77°K	327 ± 1
Burns [3] ($AlCl_3.6H_2O$)	|D|	297°K	328
	|D|	195°K	342
	|D|	77°K	343
Present Study ($AlCl_3.6H_2O$)	g	297°K	1.975 ± 0.002
	g	195°K	1.975 ± 0.002
	g	77°K	1.975 ± 0.002
	g	4.2°K	1.975 ± 0.002
	D	297°K	-326 ± 2
	D	195°K	-337 ± 2
	D	77°K	-338 ± 2
	D	4.2°K	-341 ± 2

*D is given in units of $10^{-4}cm^{-1}$

(3a) $^{53}Cr^{3+}$: Nuclear Zeeman Interaction

Within experimental error, g_n', the effective nuclear g value, is isotropic for $^{53}Cr^{3+}$ doped in $AlCl_3.6H_2O$. The nuclear Zeeman interaction induces a splitting of about 0.6 MHz ($0.2 \times 10^{-4} cm^{-1}$) and 0.9 MHz ($0.3 \times 10^{-4} cm^{-1}$) in the low and high field ESR lines, respectively. This effect is readily measured by ENDOR.

Table 6-3 lists the effective nuclear g value for $^{53}Cr^{3+}$ doped in several different samples. Column 3 is the calculated effective nuclear magnetic moment $\mu_n' = g_n' I$, in nuclear magnetons, calculated from the effective nuclear g value. Column 4 lists the magnitude of the difference between the calculated effective nuclear magnetic moment and the Handbook value for the nuclear magnetic moment, -0.4735 nuclear magnetons[41].

Table 6-3: Effective nuclear g value g_n for $^{53}Cr^{3+}$ in some trigonally distorted $Cr^{3+}.6H_2O$ complexes at $4.2^{\circ}K$

Crystal	g_n' (± 0.001)	μ_n' (± 0.002)	Difference from Handbook value
RbGa alum[28b]	-0.311	-0.466	-0.0075
CsGa alum[28b]	-0.311	-0.466	-0.0075
$AlCl_3.6H_2O$	-0.320	-0.480	+0.0065
CsAl alum[42]	-0.314	-0.471	-0.0025
RbAl alum[42]	-0.317	-0.475	+0.0015
GAlSH (1)[43]	-0.317	-0.475	+0.0015
GAlSH (2)[43]	-0.317	-0.475	+0.0015
CsIn alum[44]	-0.315	-0.472	-0.0015
		average	0.0034

The real nuclear g_n value is related to g_n', the effective nuclear g value, by

$$g_n' = g_n(1 + \sigma) \qquad 3\text{-}15$$

The shielding factor σ has been expressed by Gerschwind in the form[18]

$$\sigma = -5.84 \langle 1/r^3 \rangle_{a.u.} \Delta g/\lambda \qquad 3\text{-}16$$

Tables 6-4a and 6-4b compare the calculated nuclear magnetic moment of $^{53}Cr^{3+}$ in different crystals with the Handbook value. Table 6-4a assumes the value of the spin-orbit coupling parameter to be 91 cm^{-1}. Table 6-4b assumes the correct value of λ to be the reduced value 60 cm^{-1}.

Table 6-4a: Comparison of nuclear magnetic moment of ^{53}Cr in some trigonally distorted $Cr^{3+}.6H_2O$ complexes with the Handbook value for μ_n (assuming λ = 91 cm^{-1})

Crystal	σ	μ_n	Difference from Handbook value
RbGa alum[28b]	0.007165	-0.463	-0.0105
CsGa alum[28b]	0.007698	-0.463	-0.0105
$AlCl_3.6H_2O$	0.007545	-0.476	+0.0025
CsAl alum[42]	0.005971	-0.468	-0.0055
RbAl alum[42]	0.006707	-0.472	-0.0015
GAlSH (1)[43]	0.006047	-0.472	-0.0015
GAlSH (2)[43]	0.006453	-0.472	-0.0015
CsIn alum[44]	0.006936	-0.469	-0.0045
		average	0.0047

Table 6-4b Comparison of nuclear magnetic moment of ^{53}Cr in some trigonally distorted $Cr^{3+}.6H_2O$ complexes with the Handbook value for μ_n (assuming λ = 60 cm^{-1})

Crystal	σ	μ_n	Difference from Handbook value
RbGa alum[28b]	0.010860	-0.462	-0.0115
CsGa alum[28b]	0.011675	-0.461	-0.0125
$AlCl_3.6H_2O$	0.011440	-0.474	+0.0005
CsAl alum[42]	0.009055	-0.467	-0.0065
RbAl alum[42]	0.010173	-0.471	-0.0025
GAlSH (1)[43]	0.009171	-0.470	-0.0035
GAlSH (2)[43]	0.009787	-0.470	-0.0035
CsIn alum[44]	0.010519	-0.467	-0.0065
		average	0.0059

The nuclear magnetic moment of ^{53}Cr is independent of the crystal field. Since $\sigma > 0$ for $^{53}Cr^{3+}$ the magnitude of g_n' is greater than the magnitude of g_n. Hence the effective nuclear magnetic moment is greater than the nuclear magnetic moment.

A comparison of Table 6-3 with Table 6-4a and Table 6-4b shows that, on the average, the effective nuclear magnetic moment is closer to the Handbook value than the nuclear magnetic moments found from equations

3-15 and 3-16. The difference between the Handbook value and the calculated values for the nuclear magnetic moment of ^{53}Cr possibly originates in the calculation of σ, the shielding parameter. Geschwind's expression for σ assumes a static crystal field. It will be shown in sections 3c and 3d that a static crystal field alone does not satisfactorily describe the spin Hamiltonian parameters of $^{53}Cr^{3+}$ in a trigonally distorted octahedron of waters.

(3b) $^{53}Cr^{3+}$: Fermi Contact Term

Table 6-5 lists the values of A, B, A + 2B, A-B, and D of $^{53}Cr^{3+}$ in some trigonally distorted $Cr^{3+}.6H_2O$ magnetic complexes at 4.2°K. All of the crystals have a value of 52.1 ± 0.2 ($10^{-4}cm^{-1}$) for A + 2B. Using either McGarvey's expressions for the hyperfine constants A and B,

$$A = P(4/21\ (1 - 2a^2 + b^2) - K) \qquad 3\text{-}18$$

$$B = P(-2/21\ (1 - 2a^2 + b^2) - K) \qquad 3\text{-}19$$

or Abragam and Pryce's expression for A_{ij},

$$A_{ij} = -P(K\delta_{ij} + 3\zeta\ell_{ij} + 2\lambda\Omega_{ij} - 3\zeta\lambda U_{ij}) \qquad 3\text{-}11,$$

where $A_{zz} \equiv A$ and $A_{xx} = A_{yy} \equiv B$, it can be shown that

$$A + 2B = -3PK$$

P is given by

$$P = \frac{g_e g_n \beta\beta_n}{\langle r^3 \rangle}$$

Table 6-5: Spin Hamiltonian parameters A, B, and D, and some related parameters of $^{53}Cr^{3+}$ in some trigonally distorted $Cr^{3+}.6H_2O$ magnetic complexes at $4.2^{o}K$.

Crystal	A ($10^{-4}cm^{-1}$)	B ($10^{-4}cm^{-1}$)	A + 2B ($10^{-4}cm^{-1}$)	A - B ($10^{-4}cm^{-1}$)	D ($10^{-4}cm^{-1}$)
RbGa alum[28b]	17.372	17.291	51.954	0.081	518
RbAl alum[42]	17.357	17.274	51.905	0.083	349
$AlCl_3.6H_2O$	17.277	17.474	52.225	-0.197	-341
CsIn alum[44]	17.228	17.517	52.262	-0.289	-528
CsGa alum[28b]	17.212	17.475	52.162	-0.263	-660
CsAl alum[42]	17.204	17.459	52.122	-0.255	-715
GAlSeH (2)[44]	17.088	17.500	52.088	-0.412	-1.327
GAlSeH (1)[44]	17.026	17.472	51.970	-0.446	-1.880

where g_e is the electronic g value

g_n is the nuclear g value

β is the Bohr magneton

β_n is the nuclear magneton

$\langle r^3 \rangle$ is the average of r^3 for the 3d wave function of Cr^{3+}

K is the Fermi contact term. Both P and K are properties of the paramagnetic ion which are not very sensitive to variations in the surrounding crystal field. The value of the product of PK is

$$PK = -16.7 \times 10^{-4} cm^{-1}.$$

This is in agreement with the value of PK for $^{53}Cr^{3+}$ found by McGarvey[21]. Using $P = -40 \times 10^{-4} cm^{-1}$ the value of the Fermi contact term for $^{53}Cr^{3+}$ centered in an octahedron of waters is 0.433.

It should be noted that though the value of A + 2B falls within the range 52.1 ± 0.2 ($10^{-4} cm^{-1}$) for all of the crystals, it is not a constant within the accuracy of the ENDOR measurements (± 0.003 x $10^{-4} cm^{-1}$).

(3c) $^{53}Cr^{3+}$: The Relation between A-B and D

From the equations 3-10 and 3-11 it can be shown that

$$D = -3/2\lambda^2\Omega_{zz} \qquad 6\text{-}5$$

$$A = -P(K + 2\lambda\Omega_{zz}) \qquad 6\text{-}6$$

$$B = -P(K - \lambda\Omega_{zz}) \qquad 6\text{-}7$$

Therefore the following theoretical expression for the difference between

A and B can be obtained

$$A - B = \frac{2P}{\lambda} D$$

Using the values $P = -40 \times 10^{-4} cm^{-1}$

$$\lambda = 60\ cm^{-1}$$

the following expression is found:

$$A - B = -1.33 \times 10^{-4} D \qquad 6\text{-}8$$

Figure 6-1 is a graph of A-B versus D. The slope of the least square line through all the data points for which D is negative is 2.3×10^{-4}. Though the order of magnitude of the theoretical slope value is in agreement with the experimental value, the sign is wrong.

McGarvey found that for A > B the ligand octahedron surrounding $^{53}Cr^{3+}$ is trigonally extended, and for A < B the octahedron is trigonally compressed[21]. From the experimental data A is greater than B when D is positive, and A is less than B when D is negative. Stress measurements have shown that $^{53}Cr^{3+}$ centered in a compressed octahedron has a negative D, and a $^{53}Cr^{3+}$ in a trigonally extended octahedron has a positive D.[45] According to equation 6-8 when A - B < 0, then D > 0. Thus when the left hand side of equation 6-8 states that the octahedron of waters is compressed the right hand side states the octahedron is extended.

The nature of the discrepancy between equation 6-8 and the experimental results is believed to be due to the neglect of crystal vibrations. If equation 6-8 is correct for a static crystal field then

Figure 6-1: Plot of A - B versus D for $^{53}Cr^{3+}$ in some trigonally distorted $Cr^{3+}.6H_2O$ magnetic complexes at $4.2^{o}K$.

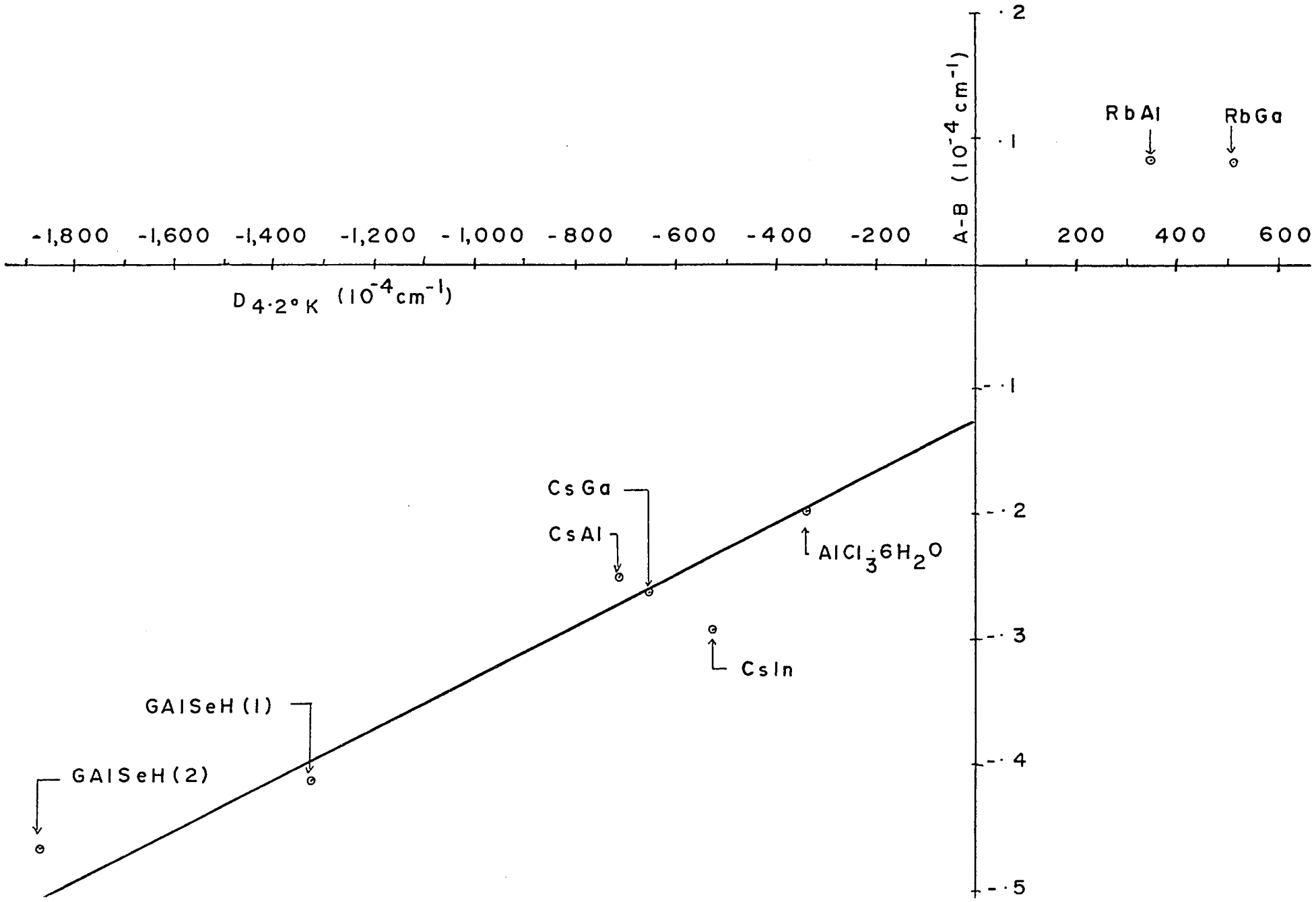
·2
·1
A-B (10^{-4} cm^{-1})
RbAl
RbGa
-1,800
-1,600
-1,400
-1,200
-1,000
-800
-600
-400
-200
200
400
600
$D_{4.2°K}$ (10^{-4}cm^{-1})
-·1
-·2
-·3
-·4
-·5
CsGa
CsAl
$AlCl_3 6H_2O$
CsIn
GAlSeH (1)
GAlSeH (2)

it can be rewritten as

$$(A - B)_s = c_s D_s$$

where the subscript s means static, and

$$c_s = 2P/\lambda$$

If A - B and D are the sum of static and vibration parts then

$$A - B = (A - B)_s + (A - B)_v$$

and

$$D = D_s + D_v$$

where the subscript v refers to vibration. In order to have a straight line graph of the form $A - B = cD + \alpha$ where c and α are the slope and intercept, the vibration part of A - B and D must be related by the expression

$$(A - B)_v = c_v D_v + \alpha$$

From plane geometry $c = c_s + c_v$.

As there are only three independent equations relating D_s, D_v, c c_s, and c_v to the data it is not possible to empirically determine the values of D_s, D_v, c_s, and c_v. However, by splitting the spin Hamiltonian parameters into static and vibration parts the plot of A - B versus D can be explained.

(3d) $^{53}Cr^{3+}$: The Relation between Q' and D

From equation 3-6 and 3-17

$$Q' = 3V_{zz}eQ \qquad 3\text{-}6$$

$$D = 3/7\ (\lambda/\Delta E)^2 \langle r^2 \rangle V_{zz} \qquad 3\text{-}17$$

the following expression can be obtained

$$Q' = kD \qquad 6\text{-}9$$

where

$$k = 7\ (\frac{\Delta E}{\lambda})^2\ \frac{1}{\langle r^2 \rangle}\ eQ$$

A plot of Q' versus D (see figure 6-2) for CsAl alum, CsGa alum, CsIn alum, and $AlCl_3.6H_2O$ shows that Q' is independent of D. If the static contribution is described by equation 6-9 then it can be rewritten as $Q' = k_s D_s$. In order to have a constant Q' value the vibration part of Q' and D must be related by the expression

$$Q'_v = k_v D_v + \beta$$

with $k_v = -k_s$. If $D_s = D_v$ then $\beta = 0$. However, as in the analysis of A - B versus D, there is not enough information to empirically determine the values of k_s, k_v, D_s, and D_v.

Figure 6-2: Plot of Q' versus D for $^{53}Cr^{3+}$ in $AlCl_3.6H_2O$ and cesium alums at 4.2°K. The dotted line indicates the behaviour expected when the trigonal distortion is due to a purely static effect.

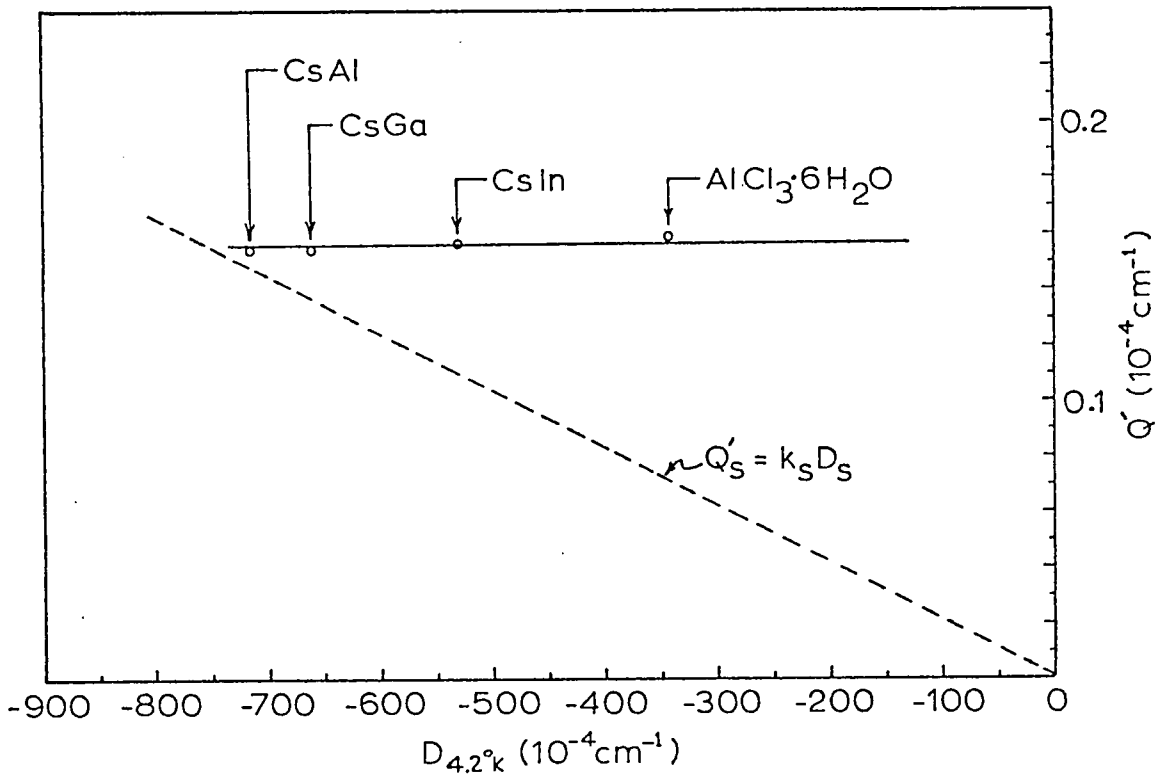
CsAl
CsGa
CsIn
AlCl3·6H2O
0.2
0.1
Q′ (10-4cm-1)
Q′s = ksDs
-900 -800 -700 -600 -500 -400 -300 -200 -100 0
D4.2°k (10-4cm-1)

Table 6-6: Comparison of the $^{53}Cr^{3+}$ spin Hamiltonian zero field splitting parameter D and the quadrupole interaction parameter Q' at 4.2°K for $AlCl_3.6H_2O$ and cesium alums.

Crystal	D $(10^{-4}cm^{-1})$	Q' $(10^{-4}cm^{-1})$
$AlCl_3.6H_2O$	-341	0.159
CsIn alum[44]	-528	0.156
CsGa alum[28b]	-670	0.155
CsAl alum[42]	-715	0.155

(4) Comparison of Relevant Spin Hamiltonian Parameter of Cr^{3+} and VO^{2+} in $AlCl_3.6H_2O$ and CsAl alum

X-ray measurements show that in $AlCl_3.6H_2O$ and CsAl alum the Al^{3+} ion is centered in a nearly regular octahedron. In $AlCl_3.6H_2O$ the Al-O distance is 1.88 ± 0.02 Å [4]. In CsAl alum the Al-O distance is 1.882 ± 0.005 Å [5]. Since the $Al^{3+}.6H_2O$ complexes in these two crystals are identical it is interesting to compare pertinent spin Hamiltonian parameters of $^{53}Cr^{3+}$ and VO^{2+} doped in $AlCl_3.6H_2O$ and CsAl alum. It is seen from Table 6-7 that the chromium D value is larger in CsAl alum than in $AlCl_3.6H_2O$. It is believed that the more negative D is, the greater is the compression of the $Cr^{3+}.6H_2O$ magnetic complex.

The hyperfine parameters A and B for VO^{2+} and $^{53}Cr^{3+}$ are larger in $AlCl_3.6H_2O$ than in CsAl alum. These results indicate that the trigonal distortion of the $Cr^{3+}.6H_2O$ complex and the tetragonal distortion of the $VO^{2+}.5H_2O$ complex are both greater in CsAl alum than in $AlCl_3.6H_2O$. This conclusion follows from the argument that since both types of complexes are under compressional distortion the system with the greater compression will have more of the chromium or vanadium charge transferred to the oxygen ligands. The effect of the charge being transferred is that the hyperfine parameters A and B, which are a measure of the interaction between the paramagnetic's nucleus and electrons, will be smaller. Though the measured A, B, and D parameters include a contribution due to crystal vibrations, this effect is not expected to change the above argument. It appears likely that the larger distortion found in CsAl alum is due to it being more susceptible to distortion upon impurity doping than is $AlCl_3.6H_2O$. In particular, the VO^{2+} results reinforce this view. When VO^{2+} substitues for Al^{3+} the neighbouring oxygen ligands are so radically affected that any small distortion from octahedral symmetry which exists in the $Al^{3+}.6H_2O$ complex does not contribute to the VO^{2+} results.

Table 6-7: Comparison of pertinent spin Hamiltonian parameters for VO^{2+} and $^{53}Cr^{3+}$ in $AlCl_3.6H_2O$ and CsAl alum (unit of parameters is $10^{-4}cm^{-1}$)

Crystal	VO^{2+} (297^oK)		$^{53}Cr^{3+}$		
	$\|A\|$	$\|B\|$	A	B	D
$AlCl_3.6H_2O$	187	72	17.277	17.474	-341
CsAl alum[42]	183	66	17.204	17.459	-715

(5) Suggestions for Future Work

VO^{2+}: Further measurements of VO^{2+} doped in hydrated crystals to form $VO^{2+}.5H_2O$ magnetic complexes should be undertaken in order to determine whether or not there is a relation between the spin Hamiltonian parameters of VO^{2+} and the spin Hamiltonian parameters of $^{53}Cr^{3+}$ doped in the same crystal.

$^{53}Cr^{3+}$: The development of a theory which satisfactorily explains the static and vibrational contributions to the spin Hamiltonian parameters is needed. At the present time an empirical approach to the separation of the zero field splitting parameter D into its static and vibrational components is being developed by Dr. Manoogian and A. Leclerc. In order to test the consistency of any theory more crystals will have to be studied. The alums comprise an extensive group of salts. The general formula is $M^{+}M^{3+}(M^{6+}O^{4})$ where M^{+} is a monocovalent metal ion, M^{3+} is a trivalent metal ion, and M^{6+} is a sulphur, selenium, or tellurium ion. The alums mentioned in this thesis contain sulphur. It would be interesting to compare the results of the sulphur containing alums with results for selenium or tellurium containing alums.

Appendix A: The Computer Program

```
C
C
C
0001            DIMENSION A(136),S(16),HA(10) ,R(256),DEL(15),TEXT(18)
0002            DIMENSION FREQ(27), FF(27)
0003            STEP=0.00001
0004            MO=2
0005            REAL  MEMORY
0006            STORE=1000.0
C
C   THE EXPLANATION OF A'S DIMENSION IS GIVEN IN BRIAN'S NOTES
C
0007              MV=1
C
C       MV IS A CODE FOR OUTPUT
C       0 SIGNIFIES FINDING BOTH EIGENVECTORS AND EIGENVALUES
C       1 SIGNIFIES FINDING ONLY THE EIGENVALUES
C
0008              N=16
C
C       N IS THE ORDER OF THE A AND R MATRICIES
C
0009              READ (1,101) (TEXT(J),J=1,18)
C
C       TEXT IS THE TITLE OF THE OUTPUT
C
0010              READ (1,2) (D,G,GNPRIM ,AHYP,QPRIME,BHYP)
C
C       THESE ARE THE APPROXIMATE HAMILTONIAN PARAMETERS
C       NOW THE SPECIFIC FIELD VALUES FOR WHICH
C       MEASUREMENTS WERE TAKEN ARE READ IN
C
0011              READ (1,33) (HA(M), M=1,9)
C
C       NOW READ IN THE MEASURED FREQUENCIES
C
0012              READ (1,5) (FREQ(I),I=1,27)
C
0013          101 FORMAT (18A4)
0014            2 FORMAT (3(F12.6),3(F12.8))
0015           33 FORMAT (9F8.5)
0016            5 FORMAT (11F7.4/11F7.4/11F7.4)
C
0017              WRITE (3,102)(TEXT(J),J=1,18)
0018              WRITE (3,100)
0019          102 FORMAT ('1',10X,18A4,//)
0020          100 FORMAT(     10X,'EIGEN VALUES',///,5X,'ENERGY VALUES FOR H ALONG
                 1Z',//)
C
C
C
C
C       M DETERMINES HOW MANY TIMES THE ITERATION IS DONE
C
0021              DO 24 M=1,10
C
0022          103 FORMAT (10X,'D = ',F12.6,'  KILOGAUSS',/,10X,'G = ',F12.6,' ELECTRONIC
```

```
     2LOGAUSS',/,10X,'Q = ',F12.8,'  KILOGAUSS',/,10X,'B = ',F12.8,
     3'  KILOGAUSS',////)
C
C     USED TO STEP TO + OR - 1/2 STEP TO EITHER SIDE OF VARIED PARAMETER
C
0023       DO 300 IC=1,3
0024       WRITE (3,103)(D,G,GNPRIM,AHYP,QPRIME,BHYP)
0025       IF (M.NE.1.AND.IC.EQ.1) WRITE (3,203) STORE
0026       IF(M.NE.1.AND.IC.EQ.1) GO TO 300
C
C     SELECTION OF NUMBER OF DIFFERENT MAGNETIC FIELDS MEASURED
C
0027       IF (MO.EQ.1) IDI=9
0028       IF (MO.EQ.2) IDI=7
0029       DO 20 K=1,IDI
0030       BNBG=(0.544633E-3)/G
0031       GBH=(1.399611E+3)*G
C
C     BNBG IS A CONSTANT KEEPING UNITS IN KILOGAUSS
C     GBH IS A CONSTANT CONVERTING KILOGAUSS TO MEGACYCLES
C
C
C
C     IDENTIFING Z AXIS MATRIX
C
0032       IF(MO.EQ.1) CALL LABEL1(A,HA,D,G,GNPRIM,AHYP,QPRIME,BHYP,BNBG,K)
C
C     IDENTIFING PERPENDICULAR AXIS MATRIX
C
0033       IF(MO.EQ.2) CALL LABEL2(A,HA,D,G,GNPRIM,AHYP,QPRIME,BHYP,BNBG,K)
0034       CALL EIGEN (A,R,N,MV)
0035       DO 270 I=1,16
0036       L=I+(I*I-I)/2
0037   270 S(I)=A(L)
C
C     EVALUATION OF TRANSITION FREQUENCIES
C
0038       DO 1 I=1,15
0039     1  DEL(I)=(S(I)-S(I+1))*GBH
C
C      WRITING OUTPUT
C
0040       WRITE (3,8) HA(K)
0041     8 FORMAT ('0',25X,F8.5,' KILOGAUSS ',6X,' CALCULATED ',5X,'  ACTUAL'
          1)
0042       DO 9 J=1,15
0043       JJ=J-3
0044       L=K+K+JJ
0045       IF (JJ) 15,15,16
0046    15 FF(J)=FREQ(L)
0047       GO TO 17
0048    16 FF(J)=0.0
0049    17 WRITE (3,10) DEL(J),FF(J)
0050     9  CONTINUE
0051    10 FORMAT (' ', 49X,F10.6,' MC ',5X,F10.6,' MC')
C
C     THIS IS TO AID IN FINDING THE CORRECT VALUE OF THE VARIED PARAMETER
C
```

```
                C       FIRST WE COMPARE ACTUAL AND CALCULATED FREQUENCIES
0052                    DIFF=0
0053                    IF (MO.EQ.2) GO TO 50
                C
                C       Z DIRECTION CALCULATION OF DIFFERENCE
                C
                C
                C       SELECTION OF LOW OR HIGH GROUP
                C
0054                    IF (K.GE.6) GO TO 31
0055                    DO 30 J=1,3
0056                 30 IF (FF(J).NE.0) DIFF=DIFF+ABS(DEL(16-J)-FF(J))
0057                    WRITE (3,202) DIFF
0058                    GO TO 60
0059                 31 DO 32 J=1,3
0060                 32 IF (FF(J).NE.0.AND.J.LE.3) DIFF=DIFF+ABS(DEL(4-J)-FF(J))
0061                    WRITE(3,202) DIFF
0062                    GO TO 60
                C
                C       PERPENDICULAR DIRECTION CALCULATION OF DIFFERENCE
                C
0063                 50 IF (K.GE.5) GO TO 43
0064                    DO 40 J=1,3
0065                 40 IF (FF(J).NE.0) DIFF=DIFF+ABS(DEL(J)-FF(J))
0066                 43 WRITE (3,202) DIFF
0067                500 FORMAT('THIS VALUE OF THE PARAMETER MAKES THE VALUES OF THE HIGH
                   1GROUP UNACCEPTABLE')
0068                    IF (K.EQ.6.AND.(FF(2).GE.DEL(15).OR.FF(2).LE.DEL(13))) WRITE (3,50
                   10)
0069                    IF (K.EQ.6.AND.(FF(2).GE.DEL(15).OR.FF(2).LE.DEL(13))) GO TO 300
0070                    IF (K.EQ.6) DIFF=ABS(DEL(14)-FF(2))
0071                    IF (K.EQ.6) WRITE (3,202) DIFF
                C
                C       IN THIS PART WE SUM UP THE DIFFERENCES WITHIN THE GROUP
                C
0072                 60 IF (K.EQ.1) TDIF=0
0073                    TDIF=TDIF+DIFF
0074                    IF (K.EQ.IDI) WRITE(3,203) TDIF
0075                 20 CONTINUE
0076                    IF (TDIF.LE.STORE) MEMORY=BHYP
0077                    IF(TDIF.LE.STORE) STORE=TDIF
0078           202   FORMAT(/' ',15X,'THE DIFFERENCE BETWEEN CALCULATED AND ACTUAL
                   1IS  ',F10.6,' MC')
0079           203   FORMAT(/' ',20X,'THE TOTAL DEVIATION IS  ',F10.6,' MC',//)
                C
                C       VARIED PARAMETER
0080                300 BHYP=BHYP+(-1)**IC*STEP*IC
0081                    BHYP=MEMORY
0082                 24  STEP=STEP/2.0
0083                    RETURN
0084                    END
```

```
      C
0001        SUBROUTINE LABEL1(A,HA,D,G,GNPRIM,AHYP,QPRIME,BHYP,BNBG,K)
0002        DIMENSION A(136), HA(10)
      C       ZEROING OUT MATRIX
      C
0003        DO 14 I=1,136
0004     14 A(I)=0.0
      C
      C       IDENTIFING NONZERO ELEMENTS
      C
0005        A(12)=1.5*BHYP
0006        A(18)=SQRT(3.)*BHYP
0007        A(25)=1.5*BHYP
0008        A(42)=SQRT(3.)*BHYP
0009        A(52)=2.0*BHYP
0010        A(63)=SQRT(3.)*BHYP
0011        A(88)=1.5*BHYP
0012        A(102)=SQRT(3.)*BHYP
0013        A(117)=1.5*BHYP
0014        A(1)=1.5*HA(K)-(1.5*GNPRIM *BNBG          *HA(K))+D+2.25*AHYP+QPRIME
0015        A(3)=1.5*HA(K)-(.5*GNPRIM *BNBG         *HA(K))+D+.75*AHYP-QPRIME
0016        A(6)=1.5*HA(K)+(.5*GNPRIM *BNBG         *HA(K))+D-.75*AHYP-QPRIME
0017        A(10)=1.5*HA(K)+(1.5*GNPRIM *BNBG          *HA(K))+D-2.25*AHYP+QPRIME
0018        A(15)=.5*HA(K)-(1.5*GNPRIM *BNBG         *HA(K))-D+.75*AHYP+QPRIME
0019        A(21)=.5*HA(K)-.5*GNPRIM*BNBG          *HA(K)-D+.25*AHYP-QPRIME
0020        A(28)=.5*HA(K)+.5*GNPRIM *BNBG          *HA(K)-D-.25*AHYP-QPRIME
0021        A(36)=.5*HA(K)+1.5*GNPRIM *BNBG          *HA(K)-D-.75*AHYP+QPRIME
0022        A(45)=-.5*HA(K)-1.5*GNPRIM *BNBG          *HA(K)-D-.75*AHYP+QPRIME
0023        A(55)=-.5*HA(K)-.5*GNPRIM *BNBG          *HA(K)-D-.25*AHYP-QPRIME
0024        A(66)=-.5*HA(K)+.5*GNPRIM *BNBG          *HA(K)-D+.25*AHYP-QPRIME
0025        A(78)=-.5*HA(K)+1.5*GNPRIM *BNBG          *HA(K)-D+.75*AHYP+QPRIME
0026        A(91)= -1.5*HA(K)-1.5*GNPRIM *BNBG          *HA(K)+D-2.25*AHYP+QPRIME
0027        A(105)=-1.5*HA(K)-.5*GNPRIM *BNBG          *HA(K)+D-.75*AHYP-QPRIME
0028        A(120)=-1.5*HA(K)+.5*GNPRIM *BNBG          *HA(K)+D+.75*AHYP-QPRIME
0029        A(136)=-1.5*HA(K)+1.5*GNPRIM *BNBG          *HA(K)+D+2.25*AHYP+QPRIME
0030        RETURN
0031        END
```

```
0001                  SUBROUTINE LABEL2(A,HA,D,G,GNPRIM,AHYP,QPRIME,BHYP,BNBG,K)
0002                  DIMENSION A(136), HA(10)
                C       ZEROING OUT MATRIX
                C
0003                  DO 14 I=1,136
0004               14 A(I)=0.0
                C
                C       IDENTIFING NONZERO ELEMENTS
                C
0005                  A1=0.5*HA(K)
0006                  A2=0.5*GNPRIM*BNBG*HA(K)
0007                  A3=0.5*D
0008                  A4=0.25*BHYP
0009                  A5=0.5*QPRIME
0010                  A (1)  =  3.*A1-3.*A2-A3+9.*A4-A5
0011                  A (3)  =  3.*A1-    A2-A3+3.*A4+A5
0012                  A (6)  =  3.*A1+    A2-A3-3.*A4+A5
0013                  A (10) =  3.*A1+3.*A2-A3-9.*A4-A5
0014                  A (15) =     A1-3.*A2+A3+3.*A4-A5
0015                  A (21) =     A1-    A2+A3+    A4+A5
0016                  A (28) =     A1+    A2+A3-    A4+A5
0017                  A(36)= A1+3.*A2+A3-3.*A4-A5
0018                  A(45)=-A1-3.*A2+A3-3.*A4-A5
0019                  A(55)=-A1-A2+A3-A4+A5
0020                  A(66)=-A1+A2+A3+A4+A5
0021                  A(78)=-A1+3.*A2+A3+3.*A4-A5
0022                  A(91)=-3.*A1-3.*A2-A3-3.*A4-A5
0023                  A(105)=-3.*A1-A2-A3-3.*A4+A5
0024                  A(120)=-3.*A1+A2-A3+3.*A4+A5
0025                  A(136)=-3.*A1+3.*A2-A3+9.*A4-A5
0026                  A( 4)=                SQRT(3.)*A5
0027                  A( 8)=                SQRT(3.)*A5
0028                  A(26)=                SQRT(3.)*A5
0029                  A(34)=                SQRT(3.)*A5
0030                  A(64)=                SQRT(3.)*A5
0031                  A(76)=                SQRT(3.)*A5
0032                  A(118)=               SQRT(3.)*A5
0033                  A(134)=               SQRT(3.)*A5
0034                  A(12)=3.*(0.25*AHYP+A4)
0035                  A(18)= SQRT(3.)*(0.5*AHYP+2.*A4)
0036                  A(25)=3.*(0.25*AHYP+A4)
0037                  A(42)= SQRT(3.)*(0.5*AHYP+2.*A4)
0038                  A(52)=AHYP+BHYP
0039                  A(63)= SQRT(3.)*(0.5*AHYP+2.*A4)
0040                  A(88)= 3.*(0.25*AHYP+A4)
0041                  A(102)= SQRT(3.)*(0.5*AHYP+2.*A4)
0042                  A(117) = 3.*(0.25*AHYP+A4)
0043                  A(16)= 3.*(0.25*AHYP-A4)
0044                  A(23)= SQRT(3.)*(0.5*AHYP-2.*A4)
0045                  A(31)= 3.*(0.25*AHYP-A4)
0046                  A(50)= SQRT(3.)*(0.5*AHYP-2.*A4)
0047                  A(61)= AHYP-BHYP
0048                  A(73)= SQRT(3.)*(0.5*AHYP-2.*A4)
0049                  A(100)=3.*(0.25*AHYP-A4)
0050                  A(115)= SQRT(3.)*(0.5*AHYP-2.*A4)
0051                  A(131)= 3.*(0.25*AHYP-A4)
0052                  A(37)=                      SQRT(3.)*A3
0053                  A(47)=                      SQRT(3.)*A3
```

```
0054          A(56)=      SQRT(3.)*A3
0055          A(70)=      SQRT(3.)*A3
0056          A(83)=      SQRT(3.)*A3
0057          A(97)=      SQRT(3.)*A3
0058          A(112)=     SQRT(3.)*A3
0059          A(128)=     SQRT(3.)*A3
0060          RETURN
0061          END
```

Appendix B: The Matrix Elements of the Spin Hamiltonian

SPIN HAMILTONIAN MATRIX ELEMENTS INCLUDING THE HYPERFINE STRUCTURE FOR THE ORIENTATION $H = H_z$.

Diagonal elements

$\langle M_I \; M_S \; |H| \; M_S \; M_I \rangle$

$\langle 3/2 \; 3/2 \; |H| 3/2 \; 3/2 \rangle = (3/2 g_{II} \beta H_z) - 3/2(g'_{nII} \beta_n H_z) + 9/4A+D+Q'$

$\langle 1/2 \; 3/2 \; |H| 3/2 \; 1/2 \rangle = (\quad " \quad) - 1/2(\quad " \quad) + 3/4A+D-Q'$

$\langle -1/2 \; 3/2 \; |H| 3/2 \; -1/2 \rangle = (\quad " \quad) + 1/2(\quad " \quad) - 3/4A+D-Q'$

$\langle -3/2 \; 3/2 \; |H| 3/2 \; -3/2 \rangle = (\quad " \quad) + 3/2(\quad " \quad) - 9/4A+D+Q'$

$\langle 3/2 \; 1/2 \; |H| 1/2 \; 3/2 \rangle = (1/2 g_{II} \beta H_z) - 3/2(g'_{nII} \beta_n H_z) + 3/4A-D+Q'$

$\langle 1/2 \; 1/2 \; |H| 1/2 \; 1/2 \rangle = (\quad " \quad) - 1/2(\quad " \quad) + 1/4A-D-Q'$

$\langle -1/2 \; 1/2 \; |H| 1/2 \; -1/2 \rangle = (\quad " \quad) + 1/2(\quad " \quad) - 1/4A-D-Q'$

$\langle -3/2 \; 1/2 \; |H| 1/2 \; -3/2 \rangle = (\quad " \quad) + 3/2(\quad " \quad) - 3/4A-D+Q'$

$$\langle 3/2\text{-}1/2|H|\text{-}1/2\ 3/2\rangle = (-1/2 g_{II}\beta H_z) - 3/2(g'_{nII}\beta_n H_z) - 3/4A\text{-}D\text{+}Q'$$

$$\langle 1/2\text{-}1/2|H|\text{-}1/2\ 1/2\rangle = (\quad " \quad) - 1/2(\quad " \quad) - 1/4A\text{-}D\text{-}Q'$$

$$\langle -1/2\text{-}1/2|H|\text{-}1/2\text{-}1/2\rangle = (\quad " \quad) + 1/2(\quad " \quad) + 1/4A\text{-}D\text{-}Q'$$

$$\langle -3/2\text{-}1/2|H|\text{-}1/2\text{-}3/2\rangle = (\quad " \quad) + 3/2(\quad " \quad) + 3/4A\text{-}D\text{+}Q'$$

$$\langle 3/2\text{-}3/2|H|\text{-}3/2\ 3/2\rangle = (-3/2 g_{II}\beta H_z) - 3/2(g'_{nII}\beta_n H_z) - 9/4A\text{+}D\text{+}Q'$$

$$\langle 1/2\text{-}3/2|H|\text{-}3/2\ 1/2\rangle = (\quad " \quad) - 1/2(\quad " \quad) - 3/4A\text{+}D\text{-}Q'$$

$$\langle -1/2\text{-}3/2|H|\text{-}3/2\text{-}1/2\rangle = (\quad " \quad) + 1/2(\quad " \quad) + 3/4A\text{+}D\text{-}Q'$$

$$\langle -3/2\text{-}3/2|H|\text{-}3/2\text{-}3/2\rangle = (\quad " \quad) + 3/2(\quad " \quad) + 9/4A\text{+}D\text{+}Q'$$

Off diagonal elements

$$\langle \pm 3/2 \pm 1/2| \ |\pm 1/2 \pm 1/3\rangle = (3/2\ B)$$

$$\langle \mp 1/2 \pm 1/2| \ |\mp 3/2 \pm 3/2\rangle = "$$

$$\langle \pm 3/2 + 1/2|H|+1/2 \pm 1/2\rangle = "$$

$$\langle \mp 1/2 \mp 3/2|H|+1/2 \mp 3/2\rangle = "$$

$< M_I\ M_S\ |H|\ M_S\ M_I >$

$\langle \pm 1/2 \pm 1/2 |H| \pm 3/2 \mp 1/2 \rangle = (\sqrt{3}\ B)$

$\langle \pm 3/2 \mp 1/2 |H| \pm 1/2 \pm 1/2 \rangle = \quad "$

$\langle \mp 1/2 \mp 1/2 |H| \pm 1/2 \mp 3/2 \rangle = \quad "$

$\langle \pm 1/2 \mp 3/2 |H| \mp 1/2 \mp 1/2 \rangle = \quad "$

$\langle \pm 1/2 \mp 1/2 |H| \pm 1/2 \mp 1/2 \rangle = 2\ B$

All other elements in this manifold are zero.

SPIN HAMILTONIAN MATRIX ELEMENTS INCLUDING THE HYPERFINE STRUCTURE WHEN THE MAGNETIC FIELD IS PERPENDICULAR TO THE Z AXIS.

Diagonal elements.

$< M_I \; M_S \; |H| \; M_S \; M_I >$

$< 3/2 \; 3/2 \; |H| 3/2 \; 3/2> = (3/2 g_\perp \beta H_\perp) - 3/2 (g'_{n\perp} \beta_n H_\perp) + 9/4 \; B - 1/2D - 1/2Q'$

$< 1/2 \; 3/2 \; |H| 3/2 \; 1/2> = (\quad " \quad) - 1/2 (\quad " \quad) + 3/4 \; B - 1/2D + 1/2Q'$

$<-1/2 \; 3/2 \; |H| 3/2 -1/2> = (\quad " \quad) + 1/2 (\quad " \quad) - 3/4 \; B - 1/2D + 1/2Q'$

$<-3/2 \; 3/2 \; |H| 3/2 -3/2> = (\quad " \quad) + 3/2 (\quad " \quad) - 9/4 \; B - 1/2D - 1/2Q'$

$< 3/2 \; 1/2 \; |H| 1/2 \; 3/2> = (1/2 g_\perp \beta H_\perp) - 3/2 (g'_{n\perp} \beta_n H_\perp) + 3/4 \; B + 1/2D - 1/2Q'$

$< 1/2 \; 1/2 \; |H| 1/2 \; 1/2> = (\quad " \quad) - 1/2 (\quad " \quad) + 1/4 \; B + 1/2D + 1/2Q'$

$<-1/2 \; 1/2 \; |H| 1/2 -1/2> = (\quad " \quad) + 1/2 (\quad " \quad) - 1/4 \; B + 1/2D + 1/2Q'$

$<-3/2 \; 1/2 \; |H| 1/2 -3/2> = (\quad " \quad) + 3/2 (\quad " \quad) - 3/4 \; B + 1/2D - 1/2Q'$

$$\langle 3/2\text{-}1/2 \,|H|\, -1/2\ 3/2\rangle = (-1/2 g_{\perp}\beta H_{\perp}) - 3/2(g'_{n\perp}\beta_n H_{\perp}) - 3/4\ B + 1/2D - 1/2Q'$$

$$\langle 1/2\text{-}1/2 \,|H|\, -1/2\ 1/2\rangle = (\quad " \quad) - 1/2(\quad " \quad) - 1/4\ B + 1/2D + 1/2Q'$$

$$\langle -1/2\text{-}1/2 \,|H|\, -1/2\text{-}1/2\rangle = (\quad " \quad) + 1/2(\quad " \quad) + 1/4\ B + 1/2D + 1/2Q'$$

$$\langle -3/2\text{-}1/2 \,|H|\, -1/2\text{-}3/2\rangle = (\quad " \quad) + 3/2(\quad " \quad) + 3/4\ B + 1/2D - 1/2Q'$$

$$\langle 3/2\text{-}3/2 \,|H|\, -3/2\ 3/2\rangle = (-3/2 g_{\perp}\beta H_{\perp}) - 3/2(g'_{n\perp}\beta_n H_{\perp}) - 9/4\ B - 1/2D - 1/2Q'$$

$$\langle 1/2\text{-}3/2 \,|H|\, -3/2\ 1/2\rangle = (\quad " \quad) - 1/2(\quad " \quad) - 3/4\ B - 1/2D + 1/2Q'$$

$$\langle -1/2\text{-}3/2 \,|H|\, -3/2\text{-}1/2\rangle = (\quad " \quad) + 1/2(\quad " \quad) + 3/4\ B - 1/2\ D + 1/2Q'$$

$$\langle -3/2\text{-}3/2 \,|H|\, -3/2\text{-}3/2\rangle = (\quad " \quad) + 3/2(\quad " \quad) + 9/4\ B - 1/2\ D - 1/2Q'$$

Off-diagonal elements

$< M_I \quad M_S | H | \quad M_S \quad M_I >$

$<\mp 1/2 \quad 3/2 | H | \quad 3/2 \pm 3/2 > \quad = \quad (\sqrt{3}/2)\, Q'$

$<\mp 3/2 \quad 3/2 | H | \quad 3/2 \pm 1/2 > \quad = \quad "$

$<\mp 1/2 \quad 1/2 | H | \quad 1/2 \pm 3/2 > \quad = \quad "$

$<\mp 3/2 \quad 1/2 | H | \quad 1/2 \pm 1/2 > \quad = \quad "$

$<\mp 1/2 \; -1/2 | H | -1/2 \pm 3/2 > \quad = \quad "$

$<\mp 3/2 \; -1/2 | H | -1/2 \pm 1/2 > \quad = \quad "$

$<\mp 1/2 \; -3/2 | H | -3/2 \pm 3/2 > \quad = \quad "$

$<\mp 3/2 \; -3/2 | H | -3/2 \pm 1/2 > \quad = \quad "$

$<\pm 3/2 \pm 1/2 | H | \pm 3/2 \pm 1/2 > \quad = \quad (3/2)A$

$<\mp 1/2 \pm 1/2 | H | \pm 3/2 \mp 3/2 > \quad = \quad "$

$<\pm 3/2 \mp 3/2 | H | \mp 1/2 \pm 1/2 > \quad = \quad "$

$<\mp 1/2 \mp 3/2 | H | \mp 1/2 \mp 3/2 > \quad = \quad "$

$$\langle \pm 1/2 \pm 1/2 | H | \pm 3/2 \mp 1/2 \rangle = \sqrt{3}\, A$$

$$\langle \pm 3/2 \mp 1/2 | H | \pm 1/2 \pm 1/2 \rangle = \text{"}$$

$$\langle \mp 1/2 \mp 1/2 | H | \pm 1/2 \mp 3/2 \rangle = \text{"}$$

$$\langle \pm 1/2 \mp 3/2 | H | \mp 1/2 \mp 1/2 \rangle = \text{"}$$

$$\langle \pm 1/2 \mp 1/2 | H | \pm 1/2 \mp 1/2 \rangle = 2\, A$$

$$\langle \pm 3/2 \mp 1/2 | H | \pm 3/2 \pm 3/2 \rangle = (\sqrt{3}/2)\, D$$

$$\langle \pm 1/2 \mp 1/2 | H | \pm 3/2 \mp 1/2 \rangle = \text{"}$$

$$\langle \mp 1/2 \mp 1/2 | H | \pm 3/2 \mp 1/2 \rangle = \text{"}$$

$$\langle \mp 3/2 \mp 1/2 | H | \pm 3/2 \mp 3/2 \rangle = \text{"}$$

$$\langle \pm 3/2 \mp 3/2 | H | \pm 1/2 \pm 3/2 \rangle = \text{"}$$

$$\langle \pm 1/2 \mp 3/2 | H | \pm 1/2 \pm 1/2 \rangle = \text{"}$$

$$\langle \mp 1/2 \mp 3/2 | H | \pm 1/2 \mp 1/2 \rangle = \text{"}$$

$$\langle \mp 3/2 \mp 3/2 | H | \pm 1/2 \mp 3/2 \rangle = \text{"}$$

All other matrix elements in this manifold are zero.

LIST OF REFERENCES

1. Emch, G., and Lacroix, R., Helv. Phys. Acta., 33, 1021, (1960).

2. Wong, E. Y., J. Chem. Phys., 32, 598, (1960).

3. Burns, G., J. Chem. Phys., 37, 1165, (1962).

4. Buchanan, D. R., and Harris, P. M., Acta. Cryst., B24, 954, (1968).

5. Cromer, D. T., Kay, M. I., and Larson, A. C., Acta. Cryst., 21, 383, (1966).

6. Andress, K. R., and Carpenter, C., Z. Kristallogr., 87, 446, (1934).

7. Jackson, J. D., Classical Electrodynamics, p. 134, (John Wiley & Sons, Inc., N.Y., 1965).

8. Reference 7, pp. 364-268.

9. Abragam, A., and Bleaney, B., Electron Paramagnetic Resonance of Transition Metal Ions, p. 678, (Clarendon Press, Oxford, 1970).

10. Reference 9, p. 692

11. Reference 7, p. 157.

12. Wood, J. H., and Pratt, G., Phys. Rev., 107, 995, (1957).

13. Slichter, C., Principles of Magnetic Resonance, p. 84, (Harper and Row, N.Y., 1963).

14. Reference 13, p. 171.

15. Bleaney, B., Hyperfine Interactions, edited by A. S. Freeman and R. B. Frankel, p. 27, (Academic Press, N.Y., 1967).

16. Reference 9, p. 167

17a. Pryce, M. H. L., Proc. Phys. Soc., A63, 25, (1950).

17b. Abragam, A., and Pryce, M. H. L., Proc. Roy. Soc. (London), A205, 135, (1951).

17c. Reference 9, section 19.2

18 Geschwind, S., Hyperfine Interactions, edited by A. J. Feeman and R. B. Frankel, p. 243, (Academic Press, N.Y., 1967).

19. Ballhausen, C. J. and Gray, H. B., Inorg. Chem., 1, 111, (1962).

20. O'Reilly, D. E. and Tsang, T., Phys. Rev., 157, 417, (1967).

21. McGarvey, B. R., J. Chem. Phys., 40, 809, (1964).

22. Kittel, C., Introduction to Solid State Physics, 4th ed. p. 580-582, (John Wiley & Sons, Inc., N.Y., 1972).

23. Van Vleck, J. H., Phys. Rev., 57, 426, (1940).

24 Ayscough, P. B., Electron Spin Resonance in Chemistry, p. 21, (Methusen & Co., Ltd., London, 1967).

25. Reference 24, p. 20

26. Terhune, R. W., Lambe, J., Kikuchi, C., and Baker, J., Phys. Rev., 123, 1265, (1961).

27. Reference 9, section 4.10

28a. Danilov, A., and Manoogian, A., Phys. Rev., B6, 4097, (1972).

28b. Danilov, A., and Manoogian, A., Phys. Rev., B6, 4103, (1972).

29. Danilov, A. G., Ph.D. Thesis, University of Ottawa, (1971), p. 58.

30. Reference 24, p. 16

31. Poole, C. P., Electron Spin Resonance, p. 529, (Interscience Publishers, N.Y., 1967).

32. Reference 29, pp. 65-69.

33. Manoogian, A., and MacKinnon, J. A., Can. J. Phys., 45, 2769, (1967).

34. Rao, K. V. S., Sastry, M. D., and Venkateswarlu, P., J. Chem. Phys., 49, 4984, (1968).

35. Seigel, I., Phys. Rev., 134, A193, (1964).

36 Reference 9, p. 431.

37. Reference 9, p. 400.

38 Owen, J., Proc. Roy. Soc. (London), A227, 183, (1954).

39. Marshall, W., and Stuart, R., Phys. Rev., 123, 2048, (1961).

40. Reference 9, p. 401

41. Handbook of Chemistry and Physics, 1968, (The Chemical Rubber Company, Cleveland, Ohio).

42. Manoogian, A., and Auger, B., Can. J. Phys., 52, 1731, (1974).

43. Manoogian, A., and Leclerc, A., Phys. Rev. B10, 1052, (1974).

44. Leclerc, A., and Manoogian, A., to be published.

45. Danilov, A. G., Vial, J. C., and Manoogian, A., Phys. Rev. B8, 3124, (1973).